

Ground-based Observations  
of  
Exoplanet Atmospheres



# Ground-based Observations of Exoplanet Atmospheres

Proefschrift

ter verkrijging van  
de graad van Doctor aan de Universiteit Leiden,  
op gezag van de Rector Magnificus prof. mr. P.F. van der Heijden,  
volgens besluit van het College voor Promoties  
te verdedigen op woensdag 28 september 2011  
klokke 11.15 uur

door

Ernst Johan Walter de Mooij

geboren te 's-Gravenhage  
in 1983

Promotiecommissie

Promotor: Prof. dr. K. H. Kuijken

Co-promotor: Dr. I. A. G. Snellen

Overige leden: Dr. M. Lopez-Morales (Institute for Space Science, Spain)  
Dr. R. J. de Kok (Netherlands Institute for Space Research, Utrecht)  
Prof. dr. M. Fridlund  
Dr. M. A. Kenworthy  
Prof. dr. H. V. J. Linnartz  
Prof. dr. E. F. van Dishoeck

Voor mijn ouders

**Cover image: Night-time on La Palma. This photo was taken during a night with full moon from the south balcony of the Isaac Newton Telescope. The telescope domes seen in this image are the William Herschel Telescope (back cover), The Liverpool Telescope (left on front cover) and the Mercator Telescope (right on front cover). On the front cover, both Mars and part of the constellation Leo are visible, including  $\gamma^1$  Leonis (Algieba), which hosts a planet.**

# Contents

	Page
<b>Chapter 1. Introduction</b>	<b>1</b>
1.1 Discovering exoplanets . . . . .	1
1.2 Studying atmospheres of transiting exoplanets . . . . .	3
1.3 Hot Jupiter atmospheres . . . . .	6
1.3.1 The atmospheric temperature structure . . . . .	6
1.3.2 Inversion layers in hot Jupiter atmospheres . . . . .	7
1.4 Observing tool: high precision photometry . . . . .	8
1.5 GROUnd-based Secondary Eclipse project (GROUSE) . . . . .	10
1.6 This thesis . . . . .	11
1.7 Outlook . . . . .	12
<b>Chapter 2. The GROUSE project I: Ground-based detection of emission from TrES-3b</b>	<b>15</b>
2.1 Introduction . . . . .	16
2.2 Observations, data reduction and analysis . . . . .	16
2.2.1 The transit of TrES-3b . . . . .	16
2.2.2 The secondary eclipse of TrES-3b . . . . .	19
2.3 Results and discussion . . . . .	20
2.3.1 The transit of TrES-3b . . . . .	20
2.3.2 The secondary eclipse of TrES-3b . . . . .	22
2.4 Conclusions . . . . .	23
<b>Chapter 3. The GROUSE project II: The secondary eclipse of HAT-P-1b</b>	<b>25</b>
3.1 Introduction . . . . .	26
3.2 Observations, data reduction and analysis . . . . .	27
3.2.1 Crosstalk, non-linearity corrections and flat-fielding . . . . .	28
3.2.2 Removal of bad-pixels . . . . .	28
3.2.3 Background subtraction . . . . .	28
3.2.4 Diffraction spokes from the secondary mirror support . . . . .	29
3.2.5 Aperture Photometry . . . . .	29
3.2.6 Correction for systematic effects . . . . .	31
3.3 Results . . . . .	32
3.3.1 Atmospheric models . . . . .	33
3.4 Conclusion . . . . .	37
<b>Chapter 4. The GROUSE project III: The secondary eclipse of WASP-33b</b>	<b>39</b>
4.1 Introduction . . . . .	40
4.2 Observations and data reduction . . . . .	41
4.2.1 Observations . . . . .	41

4.2.2	Data reduction . . . . .	43
4.3	Correction for systematic effects and stellar pulsations . . . . .	43
4.3.1	Stellar pulsations . . . . .	43
4.3.2	Light curve fitting . . . . .	45
4.4	Results and discussion . . . . .	53
4.4.1	A low albedo and rapid re-radiation of incident light . . . . .	53
4.5	Conclusion . . . . .	55
<b>Chapter 5. Transmission spectroscopy of GJ1214b</b>		<b>57</b>
5.1	Introduction . . . . .	58
5.2	Observations . . . . .	60
5.2.1	WFC observations . . . . .	60
5.2.2	GROND griz-band observations . . . . .	60
5.2.3	NOTCam $K_s$ -band observations . . . . .	60
5.2.4	LIRIS $K_c$ -band observations . . . . .	61
5.3	Data reduction . . . . .	61
5.3.1	Optical data . . . . .	61
5.3.2	Near-infrared data . . . . .	64
5.4	Transit fitting . . . . .	65
5.4.1	Optical transits . . . . .	65
5.4.2	Near-infrared transits . . . . .	66
5.5	Stellar variability . . . . .	67
5.5.1	Correcting for the stellar variability . . . . .	69
5.6	Discussion . . . . .	70
5.6.1	The transmission spectrum of GJ1214b . . . . .	70
5.6.2	Atmospheric models . . . . .	70
5.6.3	Comparison with previous measurements . . . . .	71
5.6.4	The impact of unocculted starspots . . . . .	74
5.7	Conclusions . . . . .	75
<b>Chapter 6. An ensemble study of the day-side spectra of hot Jupiters</b>		<b>79</b>
6.1	Introduction . . . . .	80
6.2	Data . . . . .	81
6.2.1	Secondary eclipse measurements . . . . .	81
6.2.2	System parameters . . . . .	87
6.2.3	Conversion to physical units . . . . .	87
6.3	Correlations with brightness temperature . . . . .	93
6.3.1	Relation with incident radiation . . . . .	93
6.3.2	Relation with stellar activity . . . . .	93
6.4	The average emission spectrum of a hot Jupiter . . . . .	98
6.5	Atmosphere models . . . . .	101
6.6	Discussion . . . . .	104
6.6.1	The effective temperatures of hot Jupiters . . . . .	104
6.6.2	Stellar activity and the presence of an inversion layer . . . . .	105
6.7	Conclusion . . . . .	107



**Nederlandse samenvatting**

**111**

**Curriculum Vitae**

**119**

**Nawoord**

**121**



---

# Chapter 1

---

## Introduction

For a long time humankind has wondered whether there are planets outside our solar system, and in particular whether there is life possible on such extrasolar planets. Until  $\sim 16$  years ago no planets were known to orbit any other star than the Sun. Since then more than 500 planets have been confirmed, and more planets are discovered on a weekly basis. An up-to-date list of exoplanets can be found on [exoplanet.eu](http://exoplanet.eu) (Schneider et al. 2011).

Interestingly, most exoplanet systems do not resemble our solar system in any way. While the interior planets around our Sun (Mercury, Venus, Earth and Mars) are all low-mass rocky planets with the four giant gaseous planets (Jupiter, Saturn, Uranus and Neptune) orbiting far away, many of the exoplanets discovered so far are giant planets orbiting their stars at separations smaller than the Earth-Sun distance. This can be partly explained by an observational bias, since it is easier to discover massive planets orbiting close to their star. In recent years more and more lower-mass planets have been discovered, and the discovery of the first earth-sized planets could be announced in the near future. However, whether these Earth-sized planets will be in orbits as in the solar system remains to be seen.

In this thesis I investigate the properties of the atmospheres of several transiting exoplanets, studying both their thermal emission in the near-infrared, for which I present the first ground-based detection, as well as the transmission-spectrum of a super-Earth. In addition I perform an ensemble study of the thermal emission properties of hot Jupiters across multiple wavebands, constructing their average emission spectrum, as well as average spectra for subsamples selected on the incident radiation and the level of activity of their host-star.

### 1.1 Discovering exoplanets

Six methods are currently used to detect extrasolar planets:

#### **a) Timing variations**

The first planet mass objects discovered outside our solar-system orbit a pulsar (Wolszczan & Frail 1992). These planets were discovered by measuring the variation in the time of arrival of the pulses from pulsar PSR1257+12, as it orbits the center of mass of the system. A similar technique has been used to discover planets around eclipsing binaries, with variations in the time of mid-eclipse as the regularly timed signal, caused by the binary orbiting the common center of mass with the circumbinary planet. So far eight circumbinary planets have been discovered in this way (e.g. Lee et al. 2009).

**b) Radial velocity**

A star with a planet orbits the common center of mass. The radial velocity technique aims to measure the changes in the star's velocity along the line of sight. From these measurements the period, semi-major axis, and a lower limit of the mass of the planet can be determined.

The first planet discovered using this technique was 51 Pegasi b (Mayor & Queloz 1995), a hot Jupiter in a 4.2 day orbit around a solar-type star. Since its discovery, approximately 400 additional planets have been found in this way. Although these observations allow the statistics of planetary orbits and planetary masses to be studied, it does not provide much information on the intrinsic properties of the planets, e.g. size, density and atmospheric composition.

**c) Astrometry**

Rather than measuring the changes in velocity of the star along the line-of-sight, it is also possible to measure the changes in position of the star in the plane of the sky. This technique has been successfully used in combination with the radial velocity technique providing all three components of the stellar velocity and yielding the true mass of the planet (e.g. McArthur et al. 2010). Although several planet discoveries have been announced using this technique (e.g. Pravdo & Shaklan 2009), none of these planets have been confirmed with follow-up observations (e.g. Bean et al. 2010b). However, very accurate astrometry from the GAIA mission should allow many planets to be discovered using astrometric measurements.

**d) Microlensing**

When light passes through the gravitational potential of an object, its trajectory will be slightly bend, making the mass act as a lens. When a mass passes between the Earth and a background star, the scales are too small to visibly distort the image of the star, as is seen for instance in a galaxy cluster lensing a background galaxy, but it causes the background star to brighten for some time. The duration of the brightening mainly depends on the mass of the lensing object (and its velocity on the plane of the sky), which can be well constrained in a statistical sense. Unfortunately, each detection is a one-off measurement, i.e. the planet is discovered by the brightening of the background star, but it is not possible to observe it again after the lensing event has past. This method is therefore capable of delivering statistics on the masses and semi-major axes of planets, but cannot be used to provide planets which can be studied in more detail. So far thirteen planetary systems have been discovered using this technique (e.g. Bond et al. 2004). In addition Sumi et al. (2011) used the microlensing technique to find ten possible free floating planet candidates, which could not have been found with the other methods described here.

**e) Direct imaging**

The four previous methods all use indirect ways to find exoplanets. Direct imaging on the other hand aims to spatially separate the light from the star and the planet. The first planet discovered by this technique orbits a brown dwarf (Chauvin et al. 2005). However, in 2008 three new planetary systems orbiting A-type main sequence stars were announced (Kalas et al. 2008; Marois et al. 2008; Lagrange et al. 2009). One of these systems, HR8799, now contains four directly imaged planets (Marois et al. 2010). Currently several instruments are being built for the direct imaging of exoplanets (e.g. SPHERE at the VLT and GPI on the Gemini South telescope), which are expected to revolutionize this field of research. Observations of exoplanets at multi-

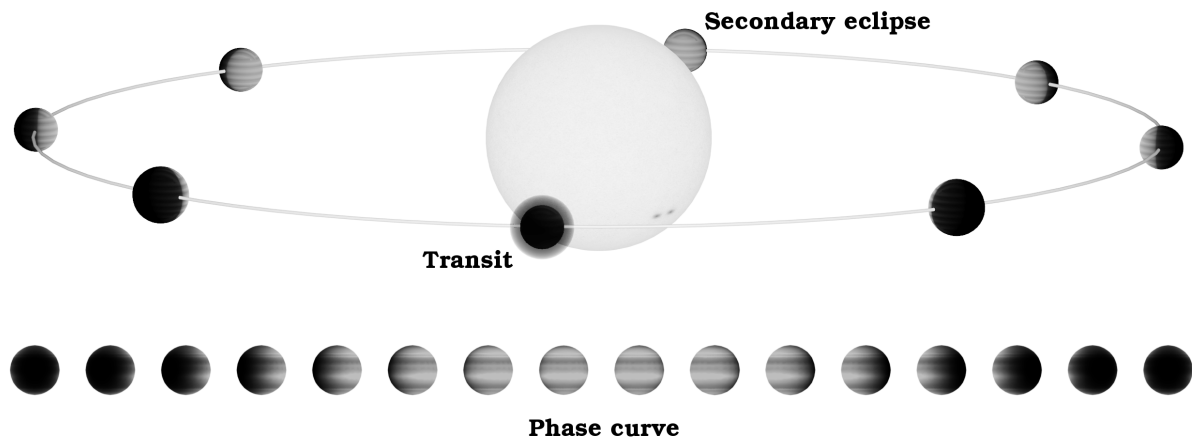


**Figure 1.1** — Illustration of the three different methods with which the atmosphere of an exoplanet can be studied. An illustration of a lightcurve for a full orbit is shown in Fig. 1.3.

ple wavelengths allow the properties of the planet’s atmosphere to be measured, with the caveat that the planet’s radius is unknown, which leads to degeneracies between the atmospheric temperature and planetary radius.

#### **f) Transit method**

When the orbital plane of the planet is aligned in such a way that the planet passes directly between the Earth and its host-star, the planet transits the stellar disk blocking part of the stellar light. The decrease in the observed light from the star is directly related to the planet-to-star size ratio, therefore allowing the radius of the planet to be determined. In addition, the fact that the planet transits its star means that the inclination is close to 90 degrees, and therefore the true mass of the planet can be determined from radial velocity measurements. From the combination of the planet’s mass and its radius, the density can be derived, which gives an indication of the composition of the planet. In addition, transiting planets allow for a whole range of interesting follow-up, including measurements of their atmospheres, which is the main subject of this thesis, and measurement of the angle between the axis of the planet’s orbit and that of the stellar rotation through the Rossiter-MacLaughlin effect (e.g. Queloz et al. 2000; Winn et al. 2006).

It is also possible to use the timing of the transits of the transiting planet to search for additional planets in the system. The gravitational interaction between the transiting planet and the additional planet will cause the time of mid-transit to vary. By measuring these variations the mass of the additional planet(s) can be determined (e.g. Lissauer et al. 2011).

## **1.2 Studying atmospheres of transiting exoplanets**

The atmospheres of transiting exoplanets can be studied in three ways (illustrated in Fig. 1.1):

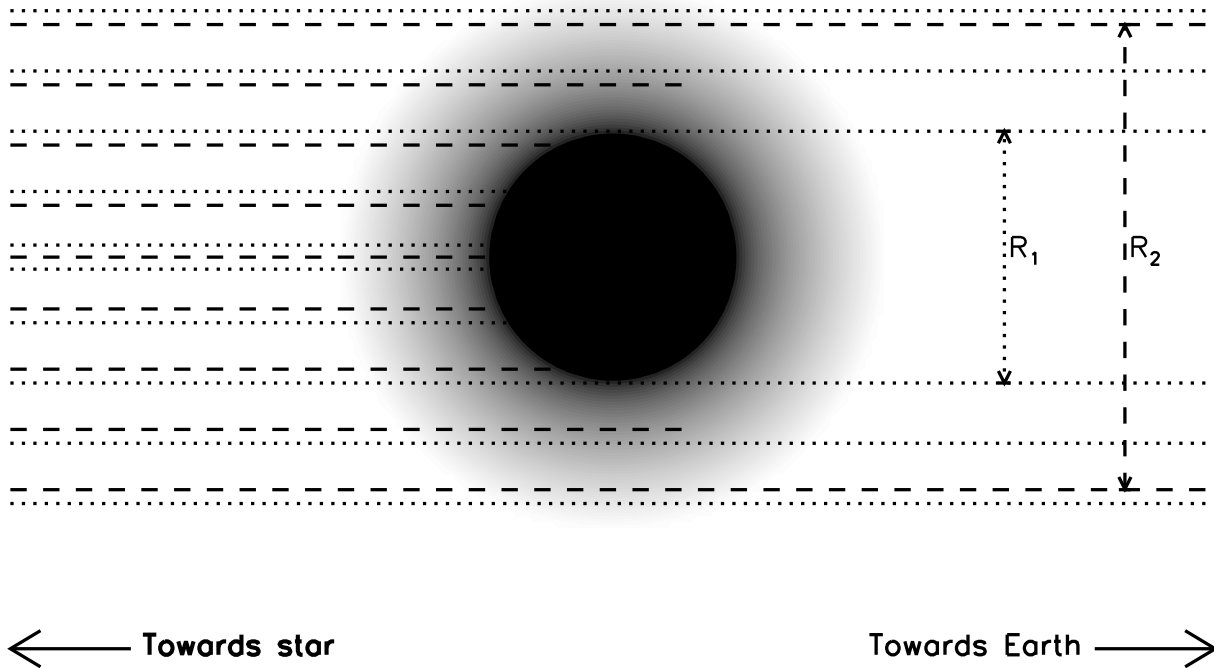


**Figure 1.2** — Illustration of transmission spectroscopy. The dashed and dotted lines indicate light at two different wavelengths, at high and low opacity respectively. At low opacity the stellar light can pass through the planet’s atmosphere unhindered, while at high opacity, the atmosphere only becomes transparent at a high altitude. This results in an increase in the observed planetary radius at a high opacity compared to that at a low opacity.

### a) Transmission spectroscopy

During the transit the planet passes in front of the star, partially blocking the light of the star. The amount of this dimming is a direct measure of the relative size of the planet compared to the size of the star. If the planet has an atmosphere, the stellar light that passes through the atmosphere is absorbed by atoms and molecules. It will make the effective size of the planet appear larger at particular wavelengths of high absorption. When looking in an absorption line, the required column density for total absorption is low, which means that the stellar light can be absorbed higher up in the atmosphere, increasing the planet-to-star ratio at that wavelength compared to a wavelength away from absorption lines (Fig. 1.2). The fractional increase in transit depth in an absorption line is  $\Delta F/F = 2\Delta R_p/R_* R_p/R_*$ , where  $R_p$  is the planetary radius,  $\Delta R_p$  is the change in radius due to absorption by a molecule and  $R_*$  is the stellar radius. The typical size variation as a function of wavelength is proportional to the atmospheric scale-height,  $H = kT/\mu g$ , where  $g$  is the planet’s surface gravity,  $T$  the atmospheric temperature and  $\mu$  the mean molecular weight of the gas. For the Earth this scale-height is about 10 km, while for a typical hot Jupiter, the scale-height is a few hundred kilometer. This corresponds to an increase in transit depth of  $\sim 10^{-7}$  and  $10^{-4}$ , for the Earth and a typical hot Jupiter respectively.

Using transmission spectroscopy the signatures of several atoms and molecules have been discovered in the atmospheres of exoplanets. The detected species include sodium (e.g. Charbonneau et al. 2002; Snellen et al. 2008; Redfield et al. 2008), potassium (Sing et al. 2011a; Colon et al. 2010), hydrogen (Vidal-Madjar et al. 2003), carbon (Vidal-Madjar et al. 2004)

and oxygen (Vidal-Madjar et al. 2004), as well as water (Tinetti et al. 2007), methane (Swain et al. 2008) and carbon-monoxide (Snellen et al. 2010). In addition, a gradual increase of the planet-to-star radius ratio of HD189733b has been detected toward shorter wavelengths, which has been attributed to the scattering by haze particles (Pont et al. 2008; Sing et al. 2011b). Many of the detections of molecules in the atmospheres of exoplanets were made using low-resolution spectroscopy and broad-band photometry, but detections at high spectral resolution (e.g. Snellen et al. 2010) are often necessary to make an unambiguous identification of the different molecules in the atmosphere.

### b) Secondary eclipse

When the planet passes behind the star, the light from the planet is blocked for the observer. By comparing the flux before, during and after the eclipse the light reflected from and/or emitted by the planet can be measured.

In the case of reflected light, the strength of the signal is proportional to the albedo,  $A$ , times the square of the ratio between the radius of the planet,  $R_p$ , and the orbital separation,  $a$ :  $\Delta F/F = A(R_p/a)^2$ . For an Earth-sized planet orbiting at  $\sim 1$  AU this leads to  $\Delta F/F < 1.8 \cdot 10^{-9}$ , while for a  $1.3 R_{\text{Jup}}$  in a  $0.03$  AU orbit (typical for the very hot Jupiters),  $\Delta F/F < 4 \cdot 10^{-4}$ . A planet's albedo governs the amount of stellar radiation that is absorbed by the planet, and therefore its equilibrium temperature.

If the thermal emission rather than reflected light from the planet is measured, the eclipse depth is proportional to the planet-to-star surface brightness ratio, multiplied with the transit depth:  $\Delta F/F = F_p/F_* (R_p/R_*)^2$ . For a typical hot Jupiter in the Ks-band the eclipse depth is  $\Delta F/F \sim 1 \cdot 10^{-3}$ . Observations of thermal emission are sensitive to both the temperature structure of the planet as well as to its chemical composition. When measurements of thermal emission at multiple wavelengths, especially around the peak of the planet's spectral energy distribution, are combined, they also allow the effective temperature of the planet to be determined. The day-side effective temperature is a measure of the total flux emitted by the planet, and depends on the level of incident stellar radiation, the planet's albedo and the efficiency at which the energy absorbed on the planet's day-side is redistributed to the planet's night-side.

### c) Phase curve

Throughout the orbit, the planet's day- and night-side rotate in and out of view. This results in small variations in the amount of light. At optical wavelengths, the variations in the light mostly come from the reflected stellar light, and therefore allow the albedo of the planet to be measured. This is similar to what is seen in the solar-system for the inner planets and the moon. When observing the planet's thermal emission, the variations in light are caused by the temperature distribution in the planet's atmosphere. If both the day- and night-side have the same temperature no phase variations are seen, while the strongest variations are seen if the day-side re-emits all the absorbed stellar radiation before it can be transported to the planet's night-side. Therefore phase curve measurements of the thermal emission from planets allow the re-distribution of the absorbed stellar light from the day- to the night-side to be determined. The efficiency of the energy redistribution helps constrain the energy budgets of the planets, and can give insights in the dominant jet streams in the planetary atmosphere. In Fig. 1.3 an illustration of a full phase-curve, including the transit and the secondary eclipse is shown.

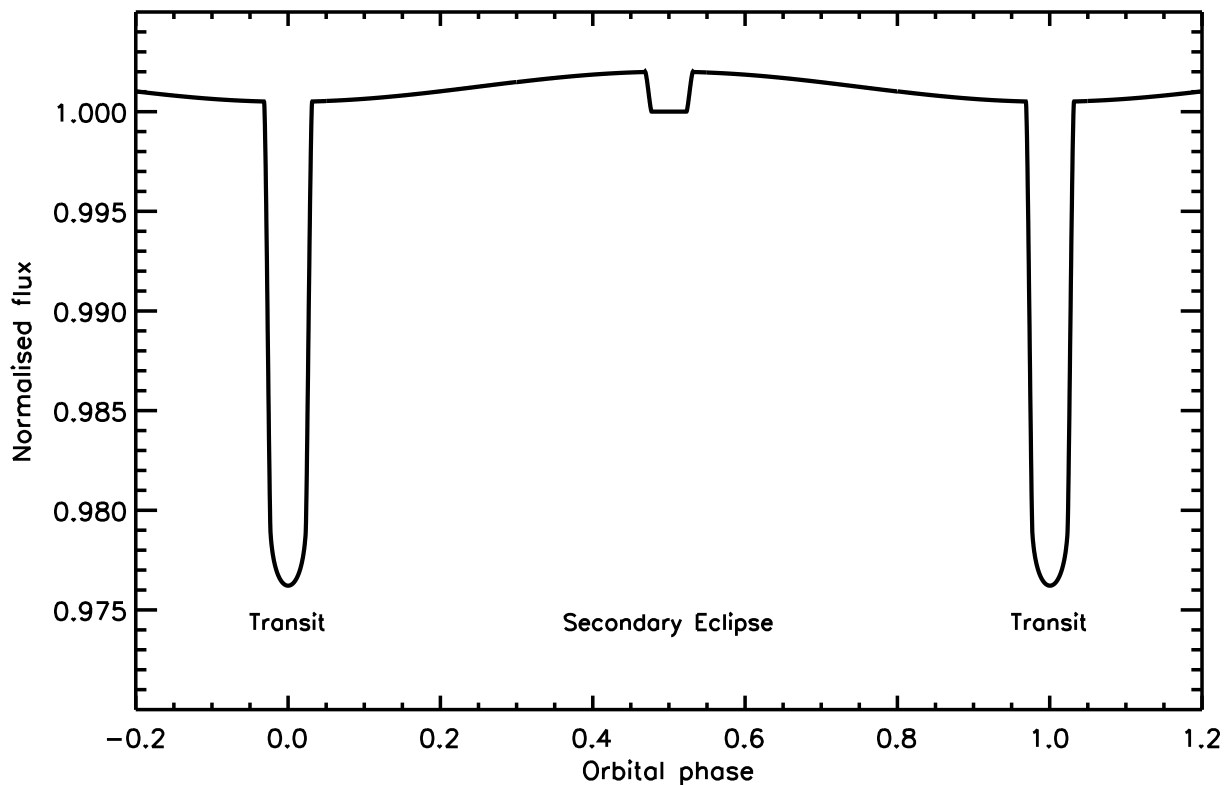


**Figure 1.3** — Illustration of a full phase curve, the slight increase between the transit and the secondary eclipse is due to the day-side of the planet rotating into view.

## 1.3 Hot Jupiter atmospheres

All the three methods discussed in the previous section probe the atmospheres of hot Jupiters in different ways. In the case of transmission spectroscopy, observations probe the atmosphere along the terminator of the planet, and are most sensitive to the composition and scale-height of the atmosphere. In the case of secondary eclipse observations which probe the thermal emission, the observations are sensitive to the chemical composition and the temperature structure of the atmosphere as described below. If the secondary eclipse measurements probe reflected starlight (for hot Jupiters this occurs at blue, optical wavelengths due to Rayleigh scattering), the measured eclipse depth provides the planet’s albedo, which in turn is important to constrain its energy budget. The measurements of the phase curve can probe both the albedo in the case of reflected light, and/or the temperature distribution between the planet’s day and night-side, which shed light on the redistribution of absorbed stellar energy on the planet.

### 1.3.1 The atmospheric temperature structure

The temperature structure of the atmosphere, together with atmospheric composition, is one of the main parameters that determines the emission spectrum of an exoplanet. The structure of the atmosphere is usually given in terms of the temperature-pressure (T-P) profile, where pressure is a measure of the altitude in the planet’s atmosphere, typically decreasing exponentially with height. There are two basic classes of T-P profile, illustrated in Fig. 1.4. In the first class the



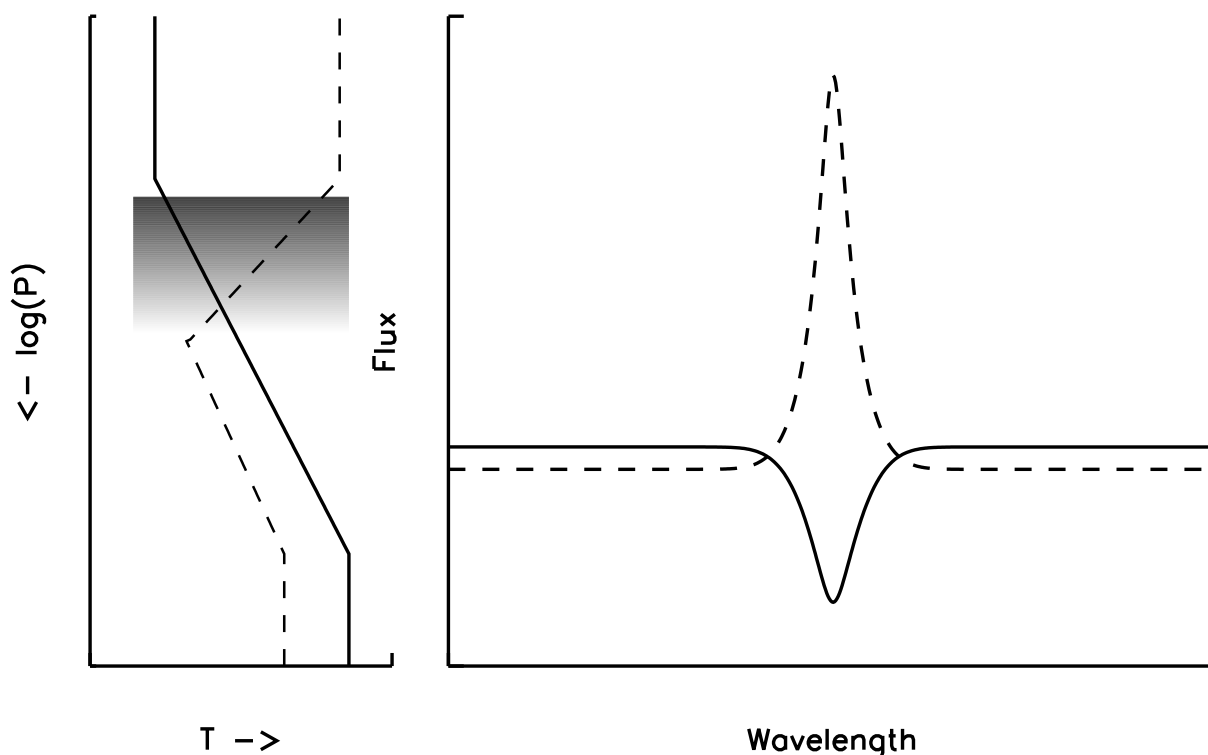


**Figure 1.4** — *Left panel:* Schematic temperature-pressure (T-P) profiles for the two types of temperature structures thought to be present in hot Jupiters. The pressure increases towards the bottom of the plot, while the altitude goes the other way. The solid line shows the  $T - P$  profile for an atmosphere without an inversion layer, while the dashed line is the  $T - P$  profile for an atmosphere with an inversion layer. The shaded area is the region in the atmosphere where a hypothetical molecule can absorb. The darkest region is where the center of the absorption line of the molecule absorbs most efficiently, while the lighter areas are towards the wings of the line. *Right panel:* Example of the resultant spectrum around a hypothetical molecular line for the two different T-P profiles. The line is seen in absorption in the case of the atmosphere without an inversion layer, since the emission in the core of line is generated in a cooler region of the atmosphere, while for the atmosphere with an inversion layer the line is seen in emission, since it probes a hotter region than the wings of the line.

temperature decreases with decreasing pressure, while in the second class the temperature starts to decrease towards higher altitudes, but then heats up again, giving rise to what is known as a temperature inversion. To get an inversion layer, a significant amount of energy needs to be deposited near the top of this layer. The Earth's stratosphere is such inversion layer, for which the increase in temperature compared to the top of the troposphere (the lowest part of the Earth's atmosphere) is caused by the absorption of ultraviolet light by ozone.

### 1.3.2 Inversion layers in hot Jupiter atmospheres

From observations of the thermal emission from hot Jupiter atmospheres, it is apparent that some planets exhibit an atmospheric inversion layer (e.g. HD209458b Knutson et al. 2008), while other planets do not (e.g. HD189733b Knutson et al. 2009). This raises the question what is responsible for the presence (or absence) of such an inversion. As mentioned above,

to get a temperature inversion, there needs to be efficient absorption of stellar radiation at the pressure-level of the inversion layer. The compounds in hot Jupiter atmospheres responsible for such absorption have not yet been identified, and the cause for their presence or absence is still unknown. However there are two competing theories that could explain this.

Fortney et al. (2008) and Burrows et al. (2008) propose that the underlying cause is the level of incident stellar radiation at the planet. When the incident radiation is above a certain level, the higher layers of the atmosphere will become hot enough to allow the absorbing compound to remain in the gas phase at these low pressures and cause the absorption. At lower temperatures the compound condenses out. As a possible candidate Burrows et al. (2008) suggest titanium-oxide and vanadium oxide (TiO/VO), which are very efficient absorbers at optical wavelengths where the bulk of the stellar energy is emitted. In this scenario the division between inversion layer and no inversion layer is around an incident stellar flux of  $10^9 \text{ erg s}^{-1} \text{ cm}^{-2}$ . In analogy with low-mass stars, Fortney et al. (2008) call the planets with a thermal inversion pM-class planets, and planets without an inversion layer pL-class planets. Recently, however, several planets have been found that receive a stellar flux well above this amount, but do not seem to have an inversion layer (e.g Fressin et al. 2010), or are below the dividing line yet do show the signs of an inversion layer (e.g. Machalek et al. 2008).

Knutson et al. (2010) investigated the stellar activity of the host star of hot Jupiters, and compared this activity with a diagnostic for the presence of an inversion layer. They found that planets around active stars do not show an inversion layer, while planets around quiet stars do. An explanation for this would be that the higher levels of UV radiation emitted by active stars destroy the compound responsible for an inversion layer. This compound could for instance be sulphur based (Zahnle et al. 2009).

The robustness of the inference of an inversion layer has recently been questioned by Madhusudhan & Seager (2010), however, who investigated the atmospheres of four hot Jupiters which were considered to have a thermal inversion in their atmospheres, using a grid of atmospheric models spanning a large range of compositions and T-P profiles. They find that for two of the four planets in their sample the spectra can be equally well fit with models with and without an inversion layer, making it questionable whether they have such a layer or not. A large part of the degeneracy in the models is due to the use of broadband filters. Observations of the day-side emission of hot Jupiters at high spectral resolution, where the individual lines can be resolved, should be able to answer the question whether a planet has a thermal inversion.

## 1.4 Observing tool: high precision photometry

To study the atmospheres of hot Jupiters, as in this thesis, it is necessary to obtain photometry with a very high signal-to-noise ratio. For instance in the near infrared the secondary eclipse depth is typically less than 3 millimagnitudes ( $\Delta F/F \lesssim 3 \cdot 10^{-3}$ ). For secondary eclipse measurements at optical wavelengths, the eclipse depths become even smaller, typically  $\lesssim 100$  micromagnitudes ( $\Delta F/F \lesssim 10^{-4}$ ).

To reach these high precisions, in particular using ground-based telescopes as used in this thesis, requires special techniques to reduce systematic effects. To correct for variations in the atmospheric transmission, differential photometry is used, in which the target is observed simultaneously with one or more reference stars. The lightcurves from these reference stars are then

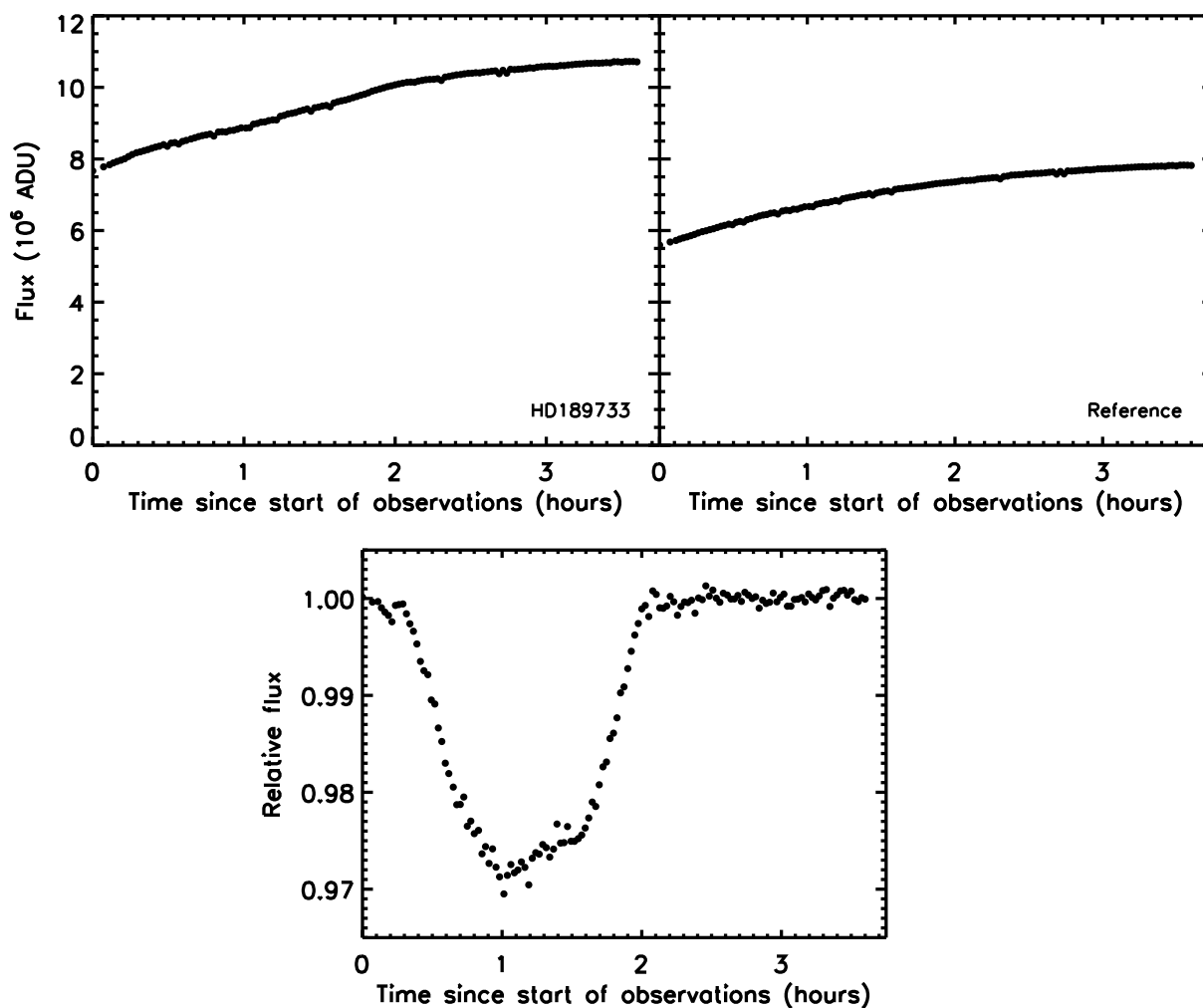


**Figure 1.5** — Example of differential photometry. Top panels: Raw lightcurves of HD189733 (left panel) and a reference star (right panel). Bottom panel: Lightcurve of HD189733 normalised by that of the reference star.

combined, and subsequently the lightcurve of the target is divided by this reference lightcurve. This takes out all the variations that the target and the reference stars have in common. In Fig. 1.5 the method is illustrated with U-band transit observations of HD189733b obtained with the Isaac Newton Telescope on La Palma. The lightcurve on the top left of the figure is for HD189733, while the lightcurve in the top right panel is for the reference star. The transit is barely visible as it is masked by a large apparent increase in flux, which is due to the decrease in airmass during the observations. By dividing the lightcurve of the target by that of the reference star, the transit becomes very clear (bottom panel of Fig. 1.5).

Unfortunately, not all systematic effects can be removed in this way, for instance uncertainties in the pixel-to-pixel variations of the flatfield can change the relative photometry between the target and reference star when the point spread function (PSF) covers different pixels during the night. These changes could be due to shifts in position of the targets on the detector, or due to seeing fluctuations. One of the solutions for this is to defocus the telescope, which causes the light to be spread over many pixels, which significantly reduces the impact of the pixel-to-pixel

sensitivity variations. This comes at a cost, however, since the light of the target is spread out over many pixels, so that the contribution of the sky-background in the aperture becomes larger, increasing the noise.

A second step to reduce the effects of the pixel-to-pixel variations is to keep the star as much as possible positioned on the same pixel. In the near-infrared this is opposite to the normal observing strategy, since normally the target is dithered to different positions on the chip so that a background map can be created, which is subsequently subtracted from the image. However, these changes in position cause significant flux variations in the lightcurve, and it is therefore preferable to keep everything as stable as possible and use a staring mode.

## 1.5 GROUnd-based Secondary Eclipse project (GROUSE)

The bulk of the emission from hot Jupiters is emitted in the near infrared ( $\lambda \lesssim 2.5\mu\text{m}$ ), at the expected peak of their spectral energy distributions (SEDs). Observations at these wavelengths are therefore crucial for constraining the energy budgets of hot Jupiters. Windows in the Earth's atmosphere allow ground-based observations in several bands in these wavelength regions. A significant part of this thesis is dedicated to secondary eclipse observations in the near-infrared of hot Jupiters, using different facilities. The project is called the GROUnd-based Secondary Eclipse project (GROUSE). The first observations for GROUSE were those of TrES-3b, and are presented in chapter 2. Subsequently many more observations have been acquired, and currently the results of two additional objects are presented in chapters 3 and 4.

The observing strategy for this project is chosen to maximize the stability. All observations are carried out in staring mode, with guiding, to minimize the change in position of the target on the detector and avoid pixel-to-pixel sensitivity variations. Since the staring mode observations do not allow us to use the eclipse observations for the background subtraction, we observe a blank field before and/or after the observations using a regular dither-pattern in order to create a background map which is subsequently scaled and subtracted from the individual science frames during the data reduction.

As explained above, we also try to minimize the systematic effects by defocusing the telescope, which causes the light to be spread over many pixels. This helps by both reducing the influence of pixel-to-pixel sensitivity variations, and allowing for longer integration times for the bright ( $K \lesssim 11$ ) targets in the program without saturating the detector. Furthermore, if possible, we try to obtain an out-of-eclipse baseline that is as long as possible, both to allow a good determination of the eclipse depth, which is measured with respect to this baseline, and to allow a good correction of systematic effects.

The current sample of planets for which we have acquired eclipse observations as part of the GROUSE-project consists mainly of very hot Jupiters: TrES-3b (chapter 2), WASP-33b (chapter 4), WASP-18b, WASP-12b, CoRoT-1b, HAT-P-7b, WASP-3b, but we also have already results of a planet receiving a lower level of incident radiation, HAT-P-1b (chapter 3). In the coming years we want to expand this project to cover also optical wavelengths ( $\lambda \lesssim 1\mu\text{m}$ ), which have a high sensitivity to the planet's effective temperature, because they probe the planet's emission spectrum in the Wien limit.

## 1.6 This thesis

In **chapter 2** we present secondary eclipse photometry of TrES-3b, which are the first results from the GROUSE project. TrES-3b is a highly irradiated planet, orbiting its star in 1.3 days. In addition we also present near-infrared transit photometry of this planet. The detection of this secondary eclipse is, together with the detection of the secondary eclipse of OGLE-TR-56b by Sing & López-Morales (2009), the first ground-based measurement of an exoplanet’s secondary eclipse.

The results from the GROUSE project on planet HAT-P-1b are presented in **chapter 3**. HAT-P-1b orbits its host-star at approximately twice the distance of TrES-3b, and therefore receives a significantly lower level of stellar radiation, placing it below the pL-boundary of Fortney et al. (2008). We find an eclipse depth of  $1.09 \pm 0.25 \cdot 10^{-3}$ , corresponding to a brightness temperature of  $2140^{+150}_{-170}$  K. The brightness temperature is much higher than both the expected equilibrium temperature and the measured brightness temperatures at longer wavelengths, and is difficult to fit with current atmospheric models.

In **chapter 4** we present the results from two nights of secondary eclipse observations of the extremely hot Jupiter WASP-33b. This planet is the first planet discovered to transit an A-type star. Its host-star also belongs to the  $\delta$  Scuti class of pulsators. Due to its very short orbital period, and the high temperature of its host-star, WASP-33b is the strongest irradiated transiting planet known to date, with an expected equilibrium temperature in excess of 3200 K. We detect the secondary eclipse at the  $12\text{-}\sigma$  level with a depth of  $0.244^{+0.027}_{-0.020}\%$ . This depth corresponds to a brightness temperature of  $3270^{+115}_{-160}$  K. Combining our measurement with the measurement of Smith et al. (2011) at optical wavelengths, we calculate an equilibrium temperature of  $3370^{+95}_{-100}$  K, which implies a very low albedo and a very inefficient energy transport of absorbed stellar radiation from the day to the night-side.

GJ1214b, the subject of **chapter 5**, is the first super-Earth discovered to transit a M-dwarf. Its low density and large planet-to-star radius ratio makes it an ideal target to search for the signs of a much cooler atmosphere. We present the results from multi-band transmission spectroscopy of this planet, which we use to investigate whether it is a mini-Neptune or a waterworld. The first will show a much stronger modulation both due to molecular absorption features as well as Rayleigh scattering, while the latter gives rise to very weak variations in the planet-to-star size ratio as a function of wavelength. We have obtained observations of this planet in eight different filters during four different transits ranging from the g-band ( $\lambda_c=460$  nm) to the  $K_c$ -band ( $\lambda_c=2.27$   $\mu\text{m}$ ). We find a  $2\text{-}\sigma$  increase in the planetary radius in the g-band compared to the measured radii at longer wavelengths, which could be due to Rayleigh scattering. In addition we find a slightly larger radius in the  $K_s$ -band which would be indicative of absorption by molecules in the planetary atmosphere. The increase in the planetary radius in both the  $K_s$  and  $K_c$  bands is smaller than expected for a solar composition model, and would require a low methane abundance. This is consistent with the measurements from Désert et al. (2011) at 3.6 and 4.5  $\mu\text{m}$ .

In **chapter 6** we present an ensemble study of hot Jupiters. With the large number of hot Jupiters for which there have been secondary eclipse measurements presented in the literature, it has now become possible to study the emission properties of a significant sample of them. We investigate the dependence of the brightness temperatures at different wavelengths on the environment of the planet. We also construct an average emission spectrum for the entire sam-

ple of hot Jupiters as well as for subsamples based on the level of incident radiation and the stellar activity. We find that the difference in the average spectrum between the planets orbiting active and quiet stars is larger than between high and lower levels of incident radiation they receive. The average spectra for planets around quiet stars and the strongest irradiated planets are consistent with models for an atmosphere with an inversion layer, while the average spectra of planets around active stars and planets receiving a lower level of stellar radiation are consistent with models with an atmosphere that does not have such thermal inversion. We also find that for determination of the effective temperature, which gives information on the albedo and energy redistribution efficiencies when coupled with the incident radiation, depends strongly on the wavelength coverage in the near-infrared, where the bulk of the planetary emission is radiated.

## 1.7 Outlook

In this thesis I show that it is possible to measure secondary eclipses of exoplanets using ground-based telescopes. In addition I show that observations in the near-infrared are very important for understanding the energy-budgets of hot Jupiters. Further secondary eclipse observations at these wavelengths are therefore necessary to constrain the properties of hot Jupiter atmospheres. Ground-based observations can be a real help with this, although it will be very important to understand the systematic effects that affect the photometric accuracy, both to get more precise measurements, as well as to push to even lower planet-to-star flux-ratios, which are expected for the cooler planets.

In addition, other techniques such as differential spectrophotometry (e.g. Bean et al. 2010a) should be developed further to allow measurements of the emission properties of hot Jupiters at higher spectral resolution, giving more insights into the structure and compositions of their atmospheres. Observations of the day-side of hot Jupiters at very high spectral resolution ( $R \sim 100,000$ ), which are able to detect the individual lines of molecules, will allow an unambiguous determination of the presence or absence of a thermal inversion in their atmospheres.

## Bibliography

- Bean, J. L., Kempton, E., & Homeier, D. 2010a, *Nature*, 468, 669
- Bean, J. L., Seifahrt, A., Hartman, H., et al. 2010b, *ApJ*, 711, L19
- Bond, I. A., Udalski, A., Jaroszyński, M., et al. 2004, *ApJ*, 606, L155
- Burrows, A., Budaj, J., & Hubeny, I. 2008, *ApJ*, 678, 1436
- Charbonneau, D., Brown, T. M., Noyes, R. W., & Gilliland, R. L. 2002, *ApJ*, 568, 377
- Chauvin, G., Lagrange, A.-M., Dumas, C., et al. 2005, *A&A*, 438, L25
- Colon, K. D., Ford, E. B., Redfield, S., et al. 2010, *ArXiv:1008.4800* [astro-ph.EP]
- Désert, J.-M., Bean, J., Miller-Ricci Kempton, E., et al. 2011, *ApJ*, 731, L40+
- Fortney, J. J., Lodders, K., Marley, M. S., & Freedman, R. S. 2008, *ApJ*, 678, 1419
- Fressin, F., Knutson, H. A., Charbonneau, D., et al. 2010, *ApJ*, 711, 374
- Kalas, P., Graham, J. R., Chiang, E., et al. 2008, *Science*, 322, 1345
- Knutson, H. A., Charbonneau, D., Allen, L. E., Burrows, A., & Megeath, S. T. 2008, *ApJ*, 673, 526
- Knutson, H. A., Charbonneau, D., Cowan, N. B., et al. 2009, *ApJ*, 690, 822
- Knutson, H. A., Howard, A. W., & Isaacson, H. 2010, *ApJ*, 720, 1569
- Lagrange, A.-M., Gratadour, D., Chauvin, G., et al. 2009, *A&A*, 493, L21
- Lee, J. W., Kim, S.-L., Kim, C.-H., et al. 2009, *AJ*, 137, 3181
- Lissauer, J. J., Fabrycky, D. C., Ford, E. B., et al. 2011, *Nature*, 470, 53
- Machalek, P., McCullough, P. R., Burke, C. J., et al. 2008, *ApJ*, 684, 1427
- Madhusudhan, N. & Seager, S. 2010, *ApJ*, 725, 261
- Marois, C., Macintosh, B., Barman, T., et al. 2008, *Science*, 322, 1348
- Marois, C., Zuckerman, B., Konopacky, Q. M., Macintosh, B., & Barman, T. 2010, *Nature*, 468, 1080
- Mayor, M. & Queloz, D. 1995, *Nature*, 378, 355
- McArthur, B. E., Benedict, G. F., Barnes, R., et al. 2010, *ApJ*, 715, 1203
- Pont, F., Knutson, H., Gilliland, R. L., Moutou, C., & Charbonneau, D. 2008, *MNRAS*, 385, 109
- Pravdo, S. H. & Shaklan, S. B. 2009, *ApJ*, 700, 623
- Queloz, D., Eggenberger, A., Mayor, M., et al. 2000, *A&A*, 359, L13
- Redfield, S., Endl, M., Cochran, W. D., & Koesterke, L. 2008, *ApJ*, 673, L87
- Schneider, J., Dedieu, C., Le Sidaner, P., Savalle, R., & Zolotukhin, I. 2011, *A&A*, 532, A79+
- Sing, D. K., Désert, J., Fortney, J. J., et al. 2011a, *A&A*, 527, A73+
- Sing, D. K. & López-Morales, M. 2009, *A&A*, 493, L31
- Sing, D. K., Pont, F., Aigrain, S., et al. 2011b, *ArXiv:1103.0026* [astro-ph.EP]
- Smith, A. M. S., Anderson, D. R., Skillen, I., Collier Cameron, A., & Smalley, B. 2011, *ArXiv:1101.2432v2* [astro-ph.EP]
- Snellen, I. A. G., Albrecht, S., de Mooij, E. J. W., & Le Poole, R. S. 2008, *A&A*, 487, 357
- Snellen, I. A. G., de Kok, R. J., de Mooij, E. J. W., & Albrecht, S. 2010, *Nature*, 465, 1049
- Sumi, T., Kamiya, K., Bennett, D. P., et al. 2011, *Nature*, 473, 349
- Swain, M. R., Vasisht, G., & Tinetti, G. 2008, *Nature*, 452, 329
- Tinetti, G., Vidal-Madjar, A., Liang, M., et al. 2007, *Nature*, 448, 169
- Vidal-Madjar, A., Désert, J., Lecavelier des Etangs, A., et al. 2004, *ApJ*, 604, L69
- Vidal-Madjar, A., Lecavelier des Etangs, A., Désert, J., et al. 2003, *Nature*, 422, 143

Winn, J. N., Johnson, J. A., Marcy, G. W., et al. 2006, ApJ, 653, L69

Wolszczan, A. & Frail, D. A. 1992, Nature, 355, 145

Zahnle, K., Marley, M. S., Freedman, R. S., Lodders, K., & Fortney, J. J. 2009, ApJ, 701, L20



---

## Chapter 2

---

# The GROUSE project I: Ground-based K-band detection of thermal emission from the exoplanet TrES-3b

*Context.* Secondary eclipse measurements of transiting extrasolar planets with the Spitzer Space Telescope have yielded several direct detections of thermal exoplanet light. Since Spitzer operates at wavelengths longward of  $3.6\mu\text{m}$ , arguably one of the most interesting parts of the planet spectrum (from 1 to  $3\mu\text{m}$ ) is inaccessible with this satellite. This region is at the peak of the planet's spectral energy distribution and is also the regime where molecular absorption bands can significantly influence the measured emission.

*Aims.* So far,  $2.2\mu\text{m}$  K-band secondary eclipse measurements, which are possible from the ground, have not yet lead to secure detections. The aim of this paper is to measure the secondary eclipse of the very hot Jupiter TrES-3b in K-band, and in addition to observe its transit, to obtain an accurate planet radius in the near infrared.

*Methods.* We have used the William Herschel Telescope (WHT) to observe the secondary eclipse, and the United Kingdom Infrared Telescope (UKIRT) to observe the transit of TrES-3b. Both observations involved significant defocusing of the telescope, aimed to produce high-cadence time series of several thousand frames at high efficiency, with the starlight spread out over many pixels.

*Results.* We detect the secondary eclipse of TrES-3b with a depth of  $-0.241\pm 0.043\%$  ( $\sim 6\sigma$ ). This corresponds to a day-side brightness temperature of  $T_{\text{B}}(2.2\mu\text{m})=2040\pm 185\text{ K}$ , which is consistent with current models of the physical properties of this planet's upper atmosphere. The centre of the eclipse seems slightly offset from phase  $\phi=0.5$  by  $\Delta\phi=-0.0042\pm 0.0027$ , which could indicate that the orbit of TrES-3b is non-circular.

Analysis of the transit data shows that TrES-3b has a near-infrared radius of  $1.338\pm 0.016R_{\text{jup}}$ , showing no significant deviation from optical measurements.

E.J.W. de Mooij & I.A.G. Snellen  
A&A 493, L35 (2009)

## 2.1 Introduction

During the secondary eclipse of an extrasolar planet (the moment the planet moves behind its host star), the contribution from the direct planet light can be measured. Until now such measurements have been the domain of the Spitzer Space Telescope, which have led to the first detections of thermal emission from extrasolar planets (Charbonneau et al. 2005; Deming et al. 2005). Until now a handful of planets has been observed at several wavelengths between  $3.6\mu\text{m}$  and  $24\mu\text{m}$ , with one of the highlights so far being the measurement of the day/night-side temperature contrast of the exoplanet HD189733b (Knutson et al. 2007).

Unfortunately, a very interesting part of the broad spectral energy distribution of hot Jupiters between 1 and  $3\mu\text{m}$  is short-ward of the observing window of Spitzer. This region contains the overall peak of the planet's emission spectrum, and can also be strongly influenced by molecular bands (e.g. from water, methane and CO) in the planets' upper atmosphere. However, ground-based observations, which could access this spectral region, have thus far proven very challenging. Several methods have been tried. Richardson et al. (2003) used a differential spectroscopic method, searching for the wavelength dependent shape of the planet spectrum, but no eclipse was detected. In addition, observations of the secondary eclipse of TrES-1b in L-band with the NIRI spectrograph on Gemini North by Knutson et al. (2007) only resulted in an upper limit.

Photometric attempts to detect the secondary eclipse of extrasolar planets have been presented by Snellen (2005) and Snellen & Covino (2007). Two partial eclipses of HD209458b were observed in K-band by Snellen (2005), while the telescope was significantly defocused to avoid saturation of the array by the bright star. Although milli-magnitude precisions were reached, nothing was detected, probably because of the lack of baseline on both sides of the eclipse (Snellen 2005). Subsequently, OGLE-TR-113b was observed (Snellen & Covino 2007), which has the great advantage that it has several other stars in its field. It was shown that randomly offsetting the telescope randomises the photometric errors down to 0.1-0.2% per hour. It resulted in a tentative detection of its secondary eclipse of  $0.17\pm 0.05\%$ .

In this chapter we present our results for K-band photometry of the transit and secondary eclipse of the planet TrES-3b (O'Donovan et al. 2007). This planet is significantly more suitable for secondary eclipse photometry than previous targets, since it is in a very close orbit ( $P\sim 1.31$  days) and its radius is significantly inflated ( $R\sim 1.3 R_{\text{jup}}$ ). Furthermore there is a nearby reference star, which can be used for differential photometry. In section 2.2 we present our observations and data reduction. In section 2.3 we present and discuss our results.

## 2.2 Observations, data reduction and analysis

### 2.2.1 The transit of TrES-3b

We have observed the transit of the exoplanet TrES-3b with the United Kingdom Infrared Telescope (UKIRT) using its Fast Track Imager (UFTI; Roche et al. 2003) on June 20, 2008. The observations, carried out in queue scheduling, lasted for almost 4 hours, starting  $\sim 0.6$  hour before ingress and ending  $\sim 1.7$  hours after egress. The field of view of UFTI is  $93\times 93$  arcsec, with a pixel scale of 0.091 arcsec/pixel. Since the distance between TrES-3 ( $K=10.61$ ) and the nearby reference star (2MASS J175225.15+373422.1,  $K\sim 9.77$ ) is  $\sim 4$  arcminutes, we

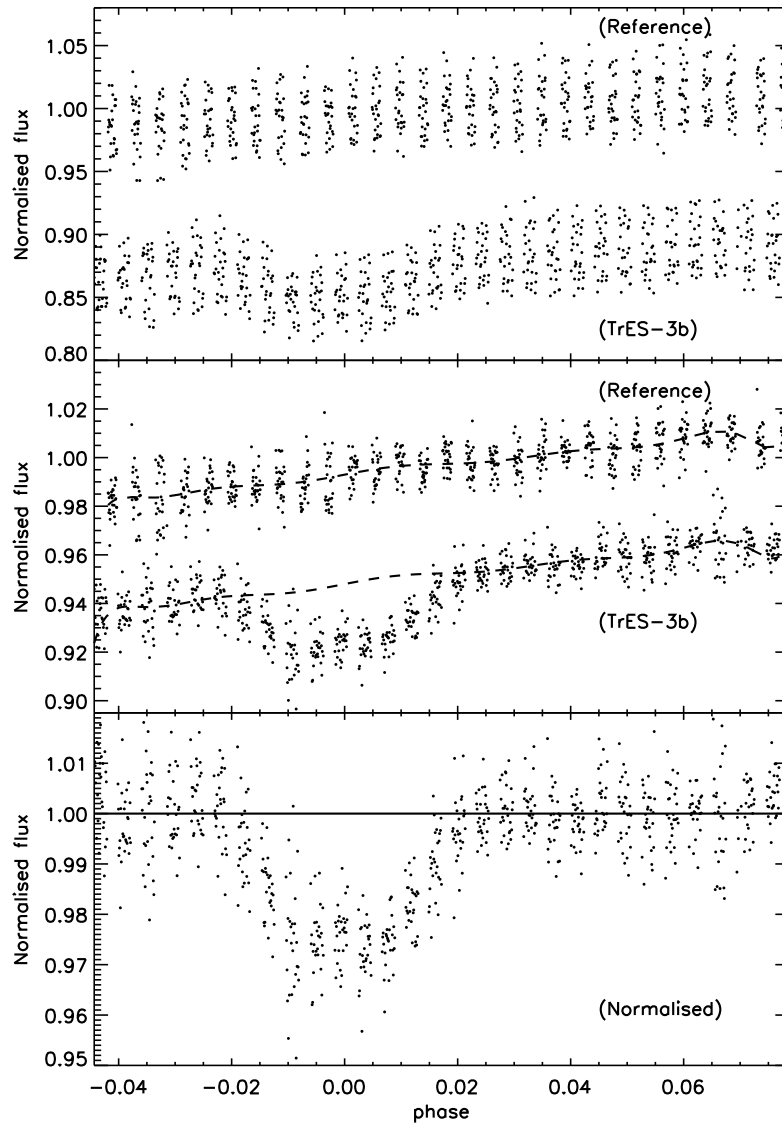


**Figure 2.1** — K-band lightcurves from the UKIRT transit observations. The top panel shows the lightcurve of the reference star and TrES-3b before correcting for the positional dependence of the flux. The middle panel shows the fluxes of both stars corrected for this effect. The dashed line is a polynomial fit to the flux of the reference star. The bottom panel shows the final corrected unbinned lightcurve of TrES-3b.

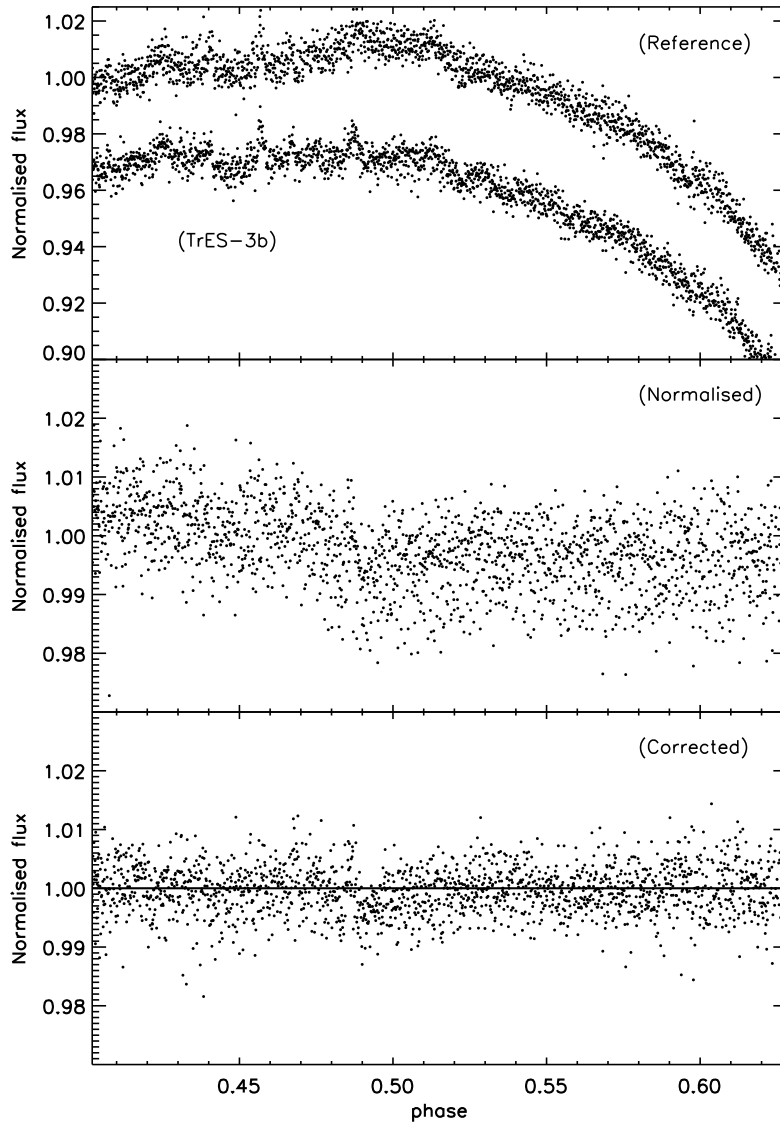


**Figure 2.2** — K-band lightcurves from the WHT secondary eclipse observations. The top panel shows the raw lightcurve for the reference star and *TrES-3b*. The middle panel shows the lightcurve of *TrES-3b* divided by that of the reference star. The bottom panel shows the final, fully corrected, lightcurve.

were forced to alternate observations between the target and the reference, in order to correct for time dependent atmospheric and instrumental effects. To reduce overheads from detector read-out, the detector was windowed to a single quadrant ( $512 \times 512$  pixels,  $46.6 \times 46.6$  arcsec) which increased the cycle speed. During each sequence we repeated a nine point dither pattern three times before switching to the other star. The exposure time was 5 seconds for the TrES-3, and 2 seconds for the reference star. With a typical overhead of 5 seconds per frame, the time required to complete an entire target-reference sequence was  $\sim 8$  minutes.

The telescope was significantly defocused to 1) reduce intrapixel variations, 2) minimise the influence of flatfield inaccuracies, and 3) prevent the count levels from reaching the non-linear range of the detector. Due to the fact that the telescope optics had not yet been realigned after the recent switch to the Cassegrain focus, the defocused telescope produced a significantly asymmetric PSF, which could be covered by a circular aperture of  $\sim 40$  pixels ( $\sim 4''$ ) in radius.

The data was flatfielded using a sky flat constructed from a series of frames taken just before the start of the observations of TrES-3. No dark subtraction was performed, because any dark-current was seen as a contribution to the sky background and removed together with the sky. The positions of the hot and cold pixels were determined from both the flat field and separate dark frames. These pixels were replaced by the values of 3rd order polynomial surfaces fitted to the  $7 \times 7$  pixels surrounding these pixels.

To determine the sky background, first all stars in the field were masked using circular masks of 30 pixels. A median sky value for the masked image was calculated and subtracted in order to remove temporal fluctuations in the background. The final sky level was determined by averaging the 27 masked frames from one cycle, and removed from the images.

Subsequently, aperture photometry was performed using the APER procedure from the IDL Astronomy User's Library<sup>1</sup> with an aperture radius of 42 pixels. Any possible residual sky fluctuations were corrected for by measuring the background value in a 42 to 70 pixel annulus around the object.

The results from the aperture photometry can be found in the top panel of Figure 2.1. Both the flux from the target and the reference star was found to be a function of dither position, therefore the data were normalised for each dither position separately. These corrected lightcurves are shown in the middle panel of Figure 2.1. To remove time dependent effects, we fitted a high order polynomial to the binned lightcurve of the reference star. This fit was used to correct the lightcurve of TrES-3. The final unbinned lightcurve for TrES-3b is shown in the bottom panel of Figure 2.1.

### 2.2.2 The secondary eclipse of TrES-3b

On July 3-4, 2008 the secondary eclipse of TrES-3b was observed with the Long-slit Intermediate Resolution Infrared Spectrograph (LIRIS; Acosta-Pulido et al. 2002) at the William Herschel Telescope (WHT) on La Palma, with the observations lasting for the entire night, starting about  $\sim 3$  hours before, and ending  $\sim 4$  hours after the expected centre of the secondary eclipse (at 1:31UT on July 4th). We used the full  $1024 \times 1024$  pixel array for these observations, which combined with the pixel size of LIRIS of  $0.25''/\text{pixel}$ , yields a field of view of  $256 \times 256$  arcseconds. This larger field of view enabled us to place both TrES-3 and the reference star si-

---

<sup>1</sup><http://idlastro.gsfc.nasa.gov>

multaneously on the detector, making these observations  $\sim 80\%$  more efficient relative to those obtained with UKIRT. We used a 9 point dither pattern, including small random offsets from the nominal positions of each dither point. We used an exposure time of 7.5 seconds, with typical overheads of 7 seconds per frame.

As for the UKIRT observations, we defocused the telescope, which resulted in a ringshaped PSF with a radius of about 4 pixels.

Since the LIRIS detector is non linear at high count levels, we applied the following empirical non-linearity correction to the data before flat fielding:

$$F_{true} = F_{meas} \cdot \frac{1}{1 - c \cdot F_{meas}^6} \quad (2.1)$$

with  $F_{true}$  the flux after correction,  $F_{meas}$  the measured flux and  $c = 6 \cdot 10^{-29}$  a constant describing the strength of the correction term. The value of  $c$  was determined by minimising the noise of the reference star over the entire night, and comparing this value to non-linearity measurements taken by the LIRIS team<sup>2</sup>.

All frames were corrected for crosstalk between the quadrants, which was found to be present in a co-add of all the reduced science frames at a level of  $10^{-5}$  of the total flux along a row of a quadrant. This correction was done on a row by row basis. A flat field was created from a series of domeflats taken with the domelight both on and off. These were subtracted from each other (to eliminate structure from the emission by the dome and telescope) and averaged.

The small number of hot and cold pixels in the image were replaced by a median of the neighbouring pixels in a  $3 \times 3$  grid. The sky was determined from the combination of the 9 images in each dither sequence, for which all the stars were masked out. We used a circular aperture with a radius of 13 pixels to determine the stellar flux and an annulus of 30 to 90 pixels to determine the level of possible residual flux in the background after sky-subtraction.

The individual raw lightcurves of TrES-3b and the reference star are plotted in the top panel of Figure 2.2. Before further analysis we divided the lightcurve of TrES-3 by that of the reference star, shown in the middle panel of Figure 2.2. The relative fluxes of the two stars are correlated with their positions on the detector. These effects are corrected for by fitting linear functions between the  $x, y$ -positions and the relative flux for data outside of the expected eclipse. These fits are then applied to the whole dataset. In a similar way a small dependence on airmass was removed. The corrected unbinned lightcurve of TrES-3b can be found in the lower panel of Figure 2.2.

## 2.3 Results and discussion

### 2.3.1 The transit of TrES-3b

The final transit lightcurve binned per 9-point dither cycle is shown in Figure 2.3. The RMS-noise level out of transit is 0.0060, while the theoretical noise level for these observations is 0.0029, which is actually dominated by the detector's readnoise of  $26e^-/\text{pixel}$ , due to the large aperture used.

<sup>2</sup>[http://www.ing.iac.es/Astronomy/instruments/liris/liris\\_detector.html](http://www.ing.iac.es/Astronomy/instruments/liris/liris_detector.html)

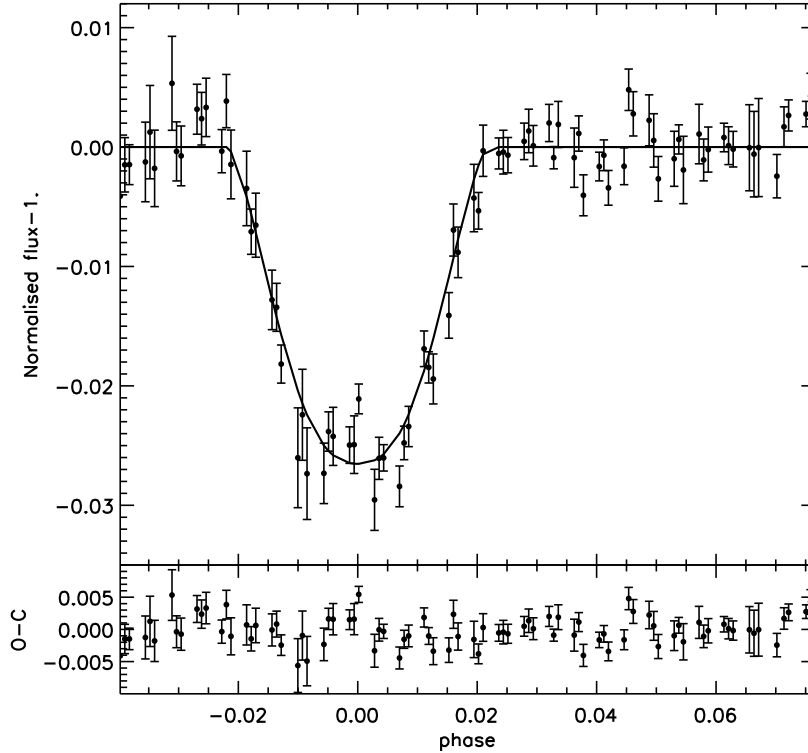


**Figure 2.3** — The 9-point binned lightcurve of the transit of TrES-3b. The solid line shows the best fitting model with  $R_p = 1.338 \pm 0.016 R_{\text{jup}}$ . The bottom panel shows the residuals after subtracting this model fit.

Since a dependence of the transit depth on wavelength can reveal characteristics of the planet atmosphere, we fitted the radius of TrES-3b, keeping the parameters of the host star and the planet’s orbit (mean stellar density, orbital inclination and ephemeris) fixed with respect to the values of Sozzetti et al. (2009). For the limb darkening we used parameters from Claret (2000), assuming a temperature of  $T = 5750\text{K}$  for the host star of TrES-3b, a metallicity of  $\log[\text{Fe}/\text{H}] = -0.2$  and a surface gravity of  $\log(g) = 4.5$ . The transit was modelled using the IDL procedures from Mandel & Agol (2002), resulting in a radius of  $1.338 \pm 0.013 R_{\text{jup}}$  at  $\chi^2/\nu = 1.58$ . The reduced  $\chi^2$  is significantly larger than unity. Since we fitted to the binned lightcurve, this indicates that the noise does not scale with  $\sqrt{N}$ , meaning that we have an additional, unknown, source of correlated noise. To obtain a better estimate of the uncertainty in the planet radius, we forced  $\chi^2/\nu = 1$  by scaling up our errors in the binned lightcurve uniformly. In this way we obtain  $R_p = 1.338 \pm 0.016 R_{\text{jup}}$ . The K-band radius shows no significant deviation from the optical radius of  $1.336^{+0.031}_{-0.037} R_{\text{jup}}$ , as measured by Sozzetti et al. (2009). The uncertainty in our K-band radius appears smaller, but this is solely due to the fact that we keep the parameters for the host star and the planet’s orbit fixed.

We show that we can obtain the K-band radius of an exoplanet at a precision of  $\sim 1\%$ . This could be further improved by observing the reference star and target at the same time both because of the increase in the number of frames during transit and because rapid atmospheric fluctuations can be corrected for.

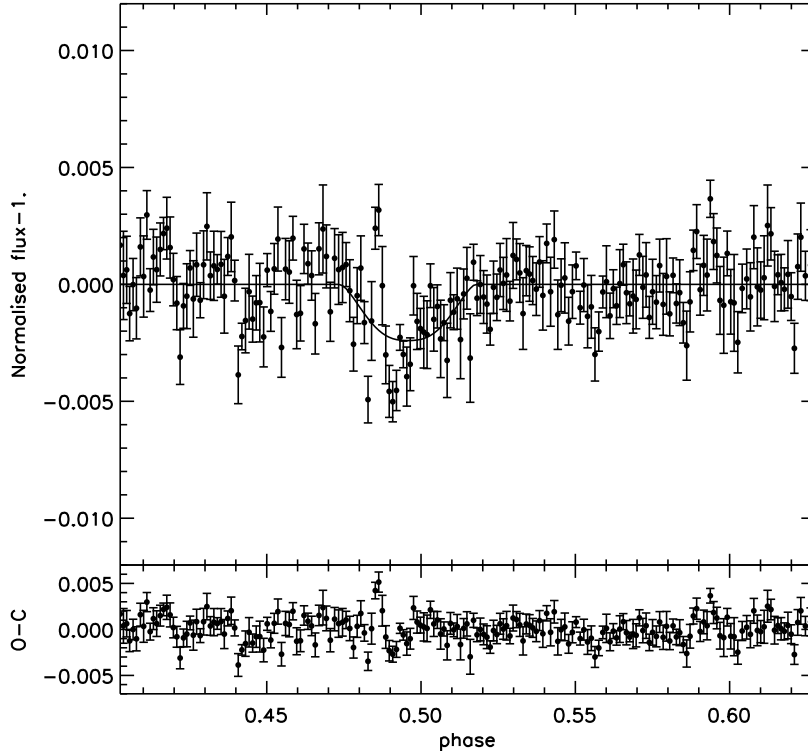


**Figure 2.4** — Final, 9-point binned lightcurve of the secondary eclipse. The solid line is the best fitting model with  $\Delta F = -0.241 \pm 0.043\%$  and an offset from phase 0.5 of  $\Delta\phi = -0.0042 \pm 0.0027$ . The bottom panel shows the residuals after subtracting the best fitting model.

### 2.3.2 The secondary eclipse of TrES-3b

The fully corrected lightcurve binned by one 9 point dither cycle is shown in Figure 2.4. Before binning, and after subtracting the best fitting model (see below), we clipped the lightcurve at  $\pm 0.01$ , removing 43 of the 1800 points (2.3%), of which 3 points (0.9%) during the eclipse. The binned lightcurve was fitted using the Mandel & Agol (2002) procedures, with all the parameters fixed to the transit model, except the centre and the depth of the eclipse (of course without limb darkening).

The best fitted lightcurve is over-plotted in the top panel of Figure 2.4, with the bottom panel showing the residuals. The out of eclipse RMS noise is 0.0038, while the expectation from theoretical noise statistics is 0.0015. The dominant source of noise in these noise calculations is the sky contribution. The total flux from the sky within the aperture is, even for the brighter reference star,  $\sim 50\%$  higher than the stellar flux.

The fitted depth of the secondary eclipse is  $\Delta F = -0.241 \pm 0.021\%$ , with a reduced chi-squared of  $\chi^2/\nu = 1.72$ . As for the transit data, the reduced  $\chi^2$  for the fit to the binned lightcurve is greater than unity, indicating that we have some extra systematic noise. We also find a timing difference in phase of  $\Delta\phi = -0.0041 \pm 0.0013$  (at  $\chi^2/\nu = 1.72$ ). The offset in the timing is intriguing, because it may indicate that the orbit of TrES-3b is not circular but slightly eccentric, with  $e\cos\omega = -0.0066 \pm 0.0021$ . Although the formal significance of the offset is  $\sim 3\sigma$ , the residual systematic noise in the lightcurve decreases its significance, in particular due to several points



around  $\phi = 0.49$ . We also refitted the data with the centre of the eclipse fixed to  $\phi=0.5$ , and obtained in this case a depth of  $-0.233\pm 0.020$  at  $\chi^2/\nu=1.77$ .

To test the influence of the more deviated points around  $\phi=0.49$ , we repeated the fit while excluding them. The depth subsequently becomes  $-0.190^{+0.034}_{-0.037}$ , with an offset in phase of  $\Delta\phi = -0.0036^{+0.0022}_{-0.0020}$  ( $\chi^2/\nu=1.39$ ). Although the significance of the fit is reduced, we still detect the secondary eclipse at a  $6\sigma$ -level.

Because it is clear that red noise dominates the uncertainties in our measurements, we tried to characterise the uncertainty using the "residual permutation" bootstrap method as used by Winn et al. (2009). The best fitting model was subtracted from the data, after which the residuals were shifted between 1 and 1800 points and added to the model light curve. These light curves were refitted for each individual shift. The resulting distributions of parameter values represent better estimates of the real uncertainties in the data. With this analysis we find an uncertainty of  $4.3\cdot 10^{-4}$  in the eclipse depth and  $2.7\cdot 10^{-3}$  for the offset in phase, which we use in the remainder of the paper.

Assuming a blackbody model for the thermal emission spectrum of TrES-3b, we can estimate the day-side brightness temperature in the K-band. For the stellar temperature, we use  $T_{\text{eff}}=5650\pm 75$  K (Sozzetti et al. 2009). From the fit to the eclipse depth using the full lightcurve we obtain  $T_b=2040\pm 185$  K (90% confidence interval).

Due to the high incident stellar flux, Fortney et al. (2008) classify this planet as belonging to the pM class of planets. This class is expected to have an inversion layer in their upper atmospheres and to show a large day/night contrast. Comparing the depth of the secondary eclipse with their model (their Figure 14), we see that our results are indeed consistent with this model. However, since we have measured the brightness temperature of TrES-3b at only single wavelength, Spitzer measurements at longer wavelengths are needed to confirm the presence of an inversion layer and thus classify TrES-3b as a pM planet.

## 2.4 Conclusions

We have detected the secondary eclipse of the exoplanet TrES-3b in K-band at a level of  $-0.241\pm 0.043\%$ , indicating a brightness temperature of  $T_b(2.2\mu\text{m})=2040\pm 185$  K. The eclipse timing shows a small offset from  $\phi=0.5$ , which would imply a non-circular orbit, but this needs to be confirmed by Spitzer observations. Also the radius of TrES-3b is determined in K-band to be  $1.338\pm 0.016 R_{\text{jup}}$ , showing no deviations from optical measurements.

## Acknowledgements

We are grateful to the UKIRT observers and the staff of both the UKIRT and WHT telescopes. The United Kingdom Infrared Telescope is operated by the Joint Astronomy Centre on behalf of the Science and Technology Facilities Council of the U.K. The William Herschel Telescope is operated on the island of La Palma by the Isaac Newton Group in the Spanish Observatorio del Roque de los Muchachos of the Instituto de Astrofísica de Canarias.

## Bibliography

- Acosta-Pulido, J., Ballesteros, E., Barreto, M., et al. 2002, *The Newsletter of the Isaac Newton Group of Telescopes*, 6, 22
- Charbonneau, D., Allen, L. E., Megeath, S. T., et al. 2005, *ApJ*, 626, 523
- Claret, A. 2000, *A&A*, 363, 1081
- Deming, D., Seager, S., Richardson, L. J., & Harrington, J. 2005, *Nature*, 434, 740
- Fortney, J. J., Lodders, K., Marley, M. S., & Freedman, R. S. 2008, *ApJ*, 678, 1419
- Knutson, H. A., Charbonneau, D., Allen, L. E., et al. 2007, *Nature*, 447, 183
- Mandel, K. & Agol, E. 2002, *ApJ*, 580, L171
- O'Donovan, F. T., Charbonneau, D., Bakos, G. Á., et al. 2007, *ApJ*, 663, L37
- Richardson, L. J., Deming, D., & Seager, S. 2003, *ApJ*, 597, 581
- Roche, P. F., Lucas, P. W., Mackay, C. D., et al. 2003, in *Proc. SPIE*, Vol. 4841, *Proc. SPIE*, ed. M. Iye & A. F. M. Moorwood, 901–912
- Snellen, I. A. G. 2005, *MNRAS*, 363, 211
- Snellen, I. A. G. & Covino, E. 2007, *MNRAS*, 375, 307
- Sozzetti, A., Torres, G., Charbonneau, D., et al. 2009, *ApJ*, 691, 1145
- Winn, J. N., Holman, M. J., Henry, G. W., et al. 2009, *ApJ*, 693, 794

---

## Chapter 3

---

# The GROUSE project II: Detection of the Ks-band secondary eclipse of exoplanet HAT-P-1b

*Context.* Only recently it has become possible to measure the thermal emission from hot Jupiters at near-Infrared wavelengths using ground-based telescopes, by secondary eclipse observations. This allows the planet flux to be probed around the peak of its spectral energy distribution, which is vital for the understanding of its energy budget.

*Aims.* The aim of the reported work is to measure the eclipse depth of the planet HAT-P-1b at  $2.2\mu\text{m}$ . This planet is an interesting case, since the amount of stellar irradiation it receives falls in between that of the two best studied systems (HD209458b and HD189733b), and it has been suggested to have a weak thermal inversion layer.

*Methods.* We have used the LIRIS instrument on the William Herschel Telescope (WHT) to observe the secondary eclipse of HAT-P-1b in the  $K_s$ -band, as part of our Ground-based secondary eclipse (GROUSE) project. The observations were done in staring mode, while significantly defocusing the telescope to avoid saturation on the  $K=8.4$  star. With an average cadence of 2.5 seconds, we collected 6520 frames during one night.

*Results.* The eclipse is detected at the  $4\text{-}\sigma$  level, the measured depth being  $0.109\pm 0.025\%$ . The uncertainties are dominated by residual systematic effects, as estimated from different reduction/analysis procedures. The measured depth corresponds to a brightness temperature of  $2136^{+150}_{-170}$  K. This brightness temperature is significantly higher than those derived from longer wavelengths, making it difficult to fit all available data points with a plausible atmospheric model. However, it may be that we underestimate the true uncertainties of our measurements, since it is notoriously difficult to assign precise statistical significance to a result when systematic effects are important.

E.J.W. de Mooij, R.J. de Kok, S.V. Nefs & I.A.G. Snellen  
A&A 528, A49 (2011)

### 3.1 Introduction

Measurements of the secondary eclipse of an exoplanet, the moment it passes behind its host star, allow us to probe the properties of the atmosphere on the day-side of the planet. The first successful secondary eclipse measurements have been obtained with the Spitzer Space Telescope (Charbonneau et al. 2005; Deming et al. 2005), followed by many more secondary eclipse measurements from  $3.6\mu\text{m}$  to  $24\mu\text{m}$  (e.g. Knutson et al. 2008; Machalek et al. 2008), see also the review by Deming (2009).

These Spitzer observations indicate that some planets exhibit a thermal inversion in their atmospheres (e.g. Knutson et al. 2008). This inversion is apparent when molecular bands in the infrared change from absorption to emission, resulting in a different shape of the planet's spectral energy distribution. Fortney et al. (2008) and Burrows et al. (2008) have proposed that such an inversion layer could be due to the presence of a strong optical absorber high in the planet's atmosphere, depending on the amount of stellar radiation the planet receives. Only for the planets receiving very high levels of irradiation, the hypothetical absorbing compound can stay in the gas-phase high up in the atmosphere, absorbing the stellar light very efficiently and causing the thermal inversion. As a possible absorber, Hubeny et al. (2003) suggested TiO and VO, although recent work (Spiegel et al. 2009) show that it might be difficult to keep these molecules in the gas phase. At lower levels of stellar irradiation, the compound possibly condenses out and is subsequently removed from the higher layers of the atmosphere. Fortney et al. (2008) dub these two classes pM and pL respectively, in analogy with L and M stellar dwarfs.

With the increase in the number of exoplanets studied with the Spitzer Space Telescope, it became clear that the above scheme cannot be solely dependent on the level of stellar irradiation. There are planets apparently exhibiting an inversion layer which receive less light from their host-star than required to keep the proposed absorber in the gas-phase (e.g. XO-1b, Machalek et al. 2008), while there are also planets that receive very high levels of irradiation, which do not apparently exhibit an inversion layer (e.g. TrES-3b, Fressin et al. 2010). Recently, Knutson et al. (2010), showed that there appears to be a trend between the presence of an inversion layer and the stellar activity (as determined from the calcium lines), with only planets around stars with low activity exhibiting an inversion layer. Madhusudhan & Seager (2010) showed that the inference of a thermal inversion is not robust, and can also depend on the chemical composition of the atmosphere.

Recently, several groups have presented measurements for a number of exoplanets in the near-infrared using ground-based telescopes (Chapter 2, Sing & López-Morales 2009; Gillon et al. 2009; Rogers et al. 2009; Anderson et al. 2010; Alonso et al. 2010; Gibson et al. 2010; Croll et al. 2010a; López-Morales et al. 2010; Croll et al. 2010b, 2011). Data in this wavelength region are very interesting because they probe the thermal emission at, or close to, the peak of the spectral energy distribution of hot Jupiters, which is vital for the understanding of their energy budgets.

Here we present the second result from the GROUnD-based Secondary Eclipse project (GROUSE), which aims to use telescopes at a variety of observatories for exoplanet secondary eclipse observations. As part of this survey we have already published our detection of the secondary eclipse of TrES-3b (Chapter 2), which we retrospectively include as paper I.

In this paper we present observations of the secondary eclipse of the hot Jupiter HAT-P-1b

(Bakos et al. 2007) in  $K_s$ -band as obtained with the Long-slit Intermediate Resolution Infrared Spectrograph (LIRIS; Acosta-Pulido et al. 2002) instrument on the William Herschel Telescope (WHT). HAT-P-1b, with a mass of  $0.52M_{\text{jup}}$  and a radius of  $1.2R_{\text{jup}}$ , orbits its G0V stellar host with a period of  $P=4.5$  days at a distance of 0.055 AU. This large orbital separation places HAT-P-1b on the lower edge of the proposed pM/pL transition boundary of Fortney et al. (2008). Recent observations of this planet by Todorov et al. (2010), who used the IRAC instrument on the Spitzer Space Telescope to determine the infrared brightness of HAT-P-1, showed evidence for a weak inversion layer. Its host star appears not to be very active (Knutson et al. 2010), which provides an alternative explanation for the planet's inversion layer, in the case that stellar variability is one of the driving factors for the structure of the atmosphere.

In Sect. 3.2 we present our observations and data-reduction. In Sect. 3.3 we will present and discuss the results, and in Sect. 3.4 we will give our conclusions.

## 3.2 Observations, data reduction and analysis

The secondary eclipse of HAT-P-1b was observed on October 2, 2009 using the imaging mode of the Long-slit Intermediate Resolution Infrared Spectrograph (LIRIS; Acosta-Pulido et al. 2002) instrument on the William Herschel Telescope (WHT) on La Palma. The expected time of mid-eclipse was  $21^{\text{h}}:55^{\text{m}}$ UT. The observations started at  $19^{\text{h}}:59^{\text{m}}$ UT and lasted for 6.5 hours, although  $\sim 15$  minutes were lost because the observer got locked up in the bathroom due to a broken door handle. Since this caused a gap in the photometry, we excluded the final 630 frames from further analysis. The exposures were taken in sequences of 50 or 100 frames. The first two frames of every sequence are known to suffer from a reset-anomaly<sup>1</sup>, visible by a very strong gradient in the background. We excluded the frames affected by the anomaly from further analysis.

The LIRIS detector was windowed to one sub-array of 512 by 512 pixels in order to increase the observing cadence. The pixel-scale of LIRIS is 0.25 arcsec per pixel, hence the field of view for these windowed observations was 128 by 128 arcseconds. Since HAT-P-1b has a slightly brighter companion star nearby, the field of view was enough to allow us to observe both HAT-P-1 ( $K=8.86$ ) and the reference star, ADS 16402 A ( $K=8.41$ ), simultaneously.

The observations were performed in staring mode, keeping the stars as much as possible at the same position on the chip. Despite guiding, a slow drift of 3 pixels over 4 hours is visible, and subsequently a sudden jump of 5 pixels in right ascension occurs. The stars also slowly drifted by 2 pixels in declination during the night.

The exposure times were varied between 1.3 and 2 seconds, in order to keep the flux-levels of the star in the linear regime of the detector. To allow these relatively long exposure times for these rather bright stars, we strongly defocused the telescope. This resulted in a donut-shaped PSF with a diameter of 15 pixels (3.75 arcsec). Despite the defocus, the PSF was still small enough to avoid overlap between the target and the reference star (which are separated by  $\sim 11.2$  arcsec), although the diffraction spikes originating from the support of the secondary mirror did overlap for certain periods (see section 3.2.4).

<sup>1</sup>[http://www.ing.iac.es/astronomy/instruments/liris/liris\\_cookbook.pdf](http://www.ing.iac.es/astronomy/instruments/liris/liris_cookbook.pdf)

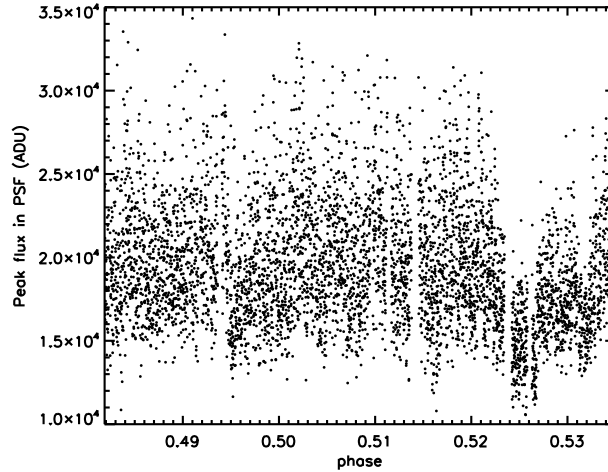


**Figure 3.1** — The flux in the highest pixel of the PSF of the brightest star as a function of time.

### 3.2.1 Crosstalk, non-linearity corrections and flat-fielding

As a first step in the data reduction we removed the intra-quadrant crosstalk, which is present as an additional flux in each pixel at the level of  $10^{-5}$  of the total flux along its row. We subsequently performed a non-linearity correction, for which we obtained a new set of measurements in August 2010. A plot of the value of the highest pixel in the PSF of the brightest star is shown in Fig. 3.1. For the non-linearity correction we observed several sequences of  $K_s$ -band dome-flats with varying exposure times to which we subsequently fitted a second order polynomial to the non-linearity for each pixel of the detector. Our current results show that the detector is non-linear for all fluxes, reaching  $\sim 8.5\%$  at 30000 ADU, above this flux level the non-linearity increases rapidly. We used this non-linearity solution to correct all our frames. We excluded all frames with the peak flux of the brightest star above 30000 ADU.

All the frames were flatfielded using a flatfield created from a set of dome flats, both with the dome-lights on and off to remove both the effects of emission from the telescope structure, as well as structure due to the dark-current from the detector. The flat-field images were corrected for the intra-quadrant crosstalk and non-linearity in the same way as the science images.

### 3.2.2 Removal of bad-pixels

During most of the observations, one hot-pixel is located within the PSF of the target. This hot-pixel was corrected for by replacing it with the flux of the corresponding pixel in the reference star, scaled by the flux ratio of the stars. Since the position difference between the two stars is not an integer, and the precise flux in inner edge of the donut is a strong function of position, we interpolated the PSF of the reference star to the same grid as HAT-P-1 before measuring the flux in the corresponding pixel.

### 3.2.3 Background subtraction

The background level during the observations varied, and the variation of the background per pixel is shown in Fig. 3.2. A background map was constructed from a separate set of observa-

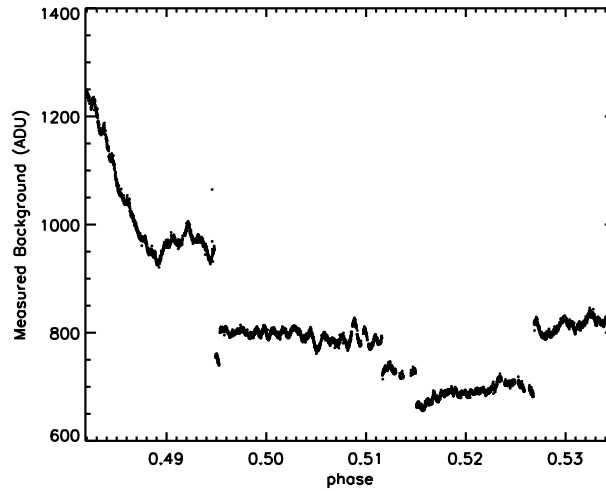


**Figure 3.2** — The variation of the sky background during the night.

tions of a different field taken on the same night. After subtracting this background map from the images, a small gradient was still apparent along the y-axis, which we believe is due to different exposure times (and dark currents) for the images used for the creation of the background map and the science images. To remove this gradient, we first masked out all the stars and bad-pixels and subsequently determined the mean along a row of the detector, rejecting outliers deviating by more than 3 times the standard deviation from the median of the row. The resultant profile along the y-axis was then fitted with a polynomial, in order to create a smooth background map, which was subsequently subtracted from all the columns of the image.

The overall impact of the subtraction of a background image on the results is small, but not subtracting the background image results in an increased noise-level.

### 3.2.4 Diffraction spikes from the secondary mirror support

The close proximity of the reference star causes the diffraction pattern from the support structure for the secondary mirror to overlap with the other star's PSF. Since the WHT is on an alt-az mount, the instrument is rotated to maintain the same position angle on the sky. This causes the diffraction spikes at certain times to overlap, depending on the position-angle of the mount. In Fig. 3.3 two images are shown, on the left side with a rotator angle of  $-79.2$  degrees, with the diffraction spikes not overlapping, while in the right side the rotator angle was  $+55$  degrees, where the diffraction spikes do overlap. To account for this, the amount of flux in a region offset by the same amount as the separation between the two stars was measured, and subsequently subtracted from the measured flux values of the stars, after accounting for the difference in flux levels.

### 3.2.5 Aperture Photometry

Subsequently, we performed aperture photometry on the two stars, with a radius of 14 pixels (3.5 arcsec), chosen to maximise the flux, but minimise the influence of the background. Any residual background was determined by measuring the mean flux in two boxes located 60 pixels

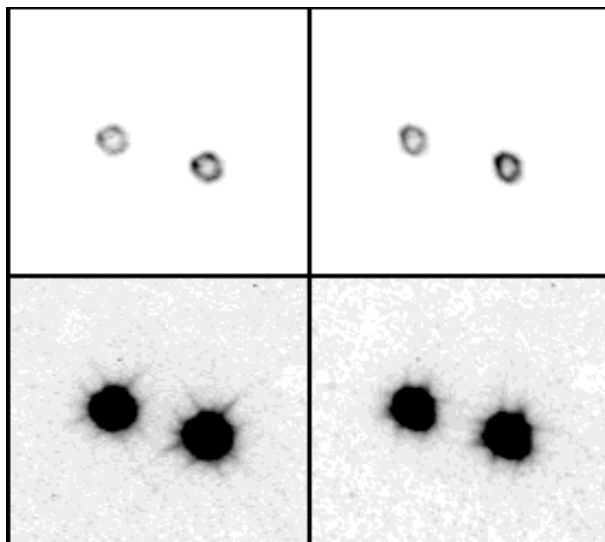


**Figure 3.3** — Sample of PSFs for our observations at high and low count-levels for different mount rotator angles. Left panels: mount rotator angle of  $-79.2$  degrees. Right panels:  $+55.0$  degrees. The spokes caused by the support structure of the secondary mirror can be clearly seen to rotate due to the alt-az mounting of the telescope.

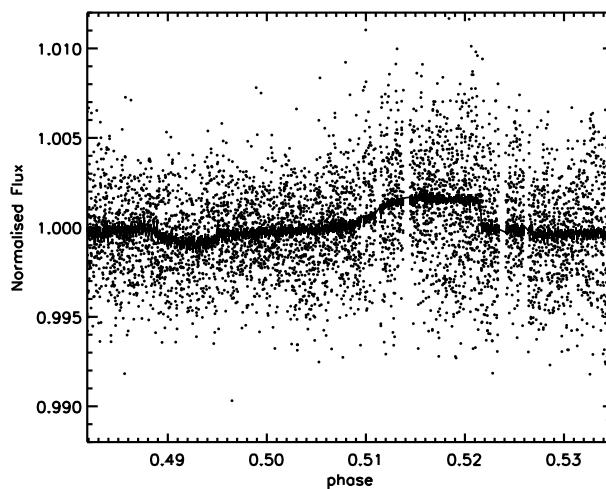


**Figure 3.4** — Data points show the uncorrected lightcurve of HAT-P-1b with the WHT on La Palma. The solid line indicates the best fitting model where we fit simultaneous for both the systematic effects as well as the eclipse depth.

(15 arcsec) above and below the midpoint between the two stars, with a box-size of 131 by 41 pixels (32.75 by 10.25 arcsec). In these boxes, we excluded bad-pixels from the background-determination, as well as masked the areas that can be affected by the diffraction spikes from the secondary mirror support.



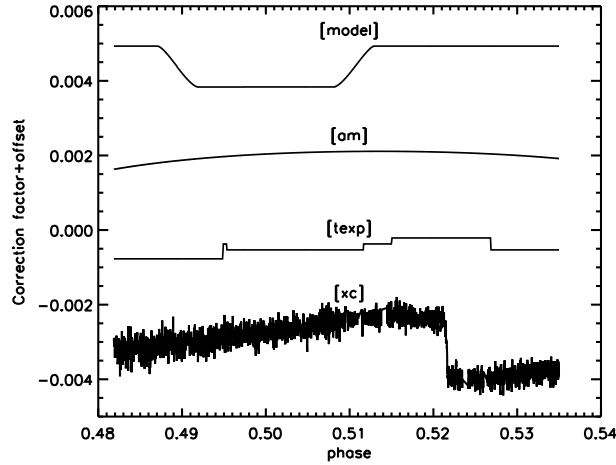


**Figure 3.5** — Different components fitted to the lightcurve due to the eclipse and systematic effects. Shown are, from top to bottom, the eclipse model, the airmass, the exposure time and the x position on the detector. The different parameters are offset for clarity.

**Table 3.1** — Parameters for HAT-P-1. References: (1) Winn et al. (2007); (2) Johnson et al. (2008); (3) this work; (4) Todorov et al. (2010)

parameter	Value	Reference
Semi-major axis $a$ (au)	$0.0551 \pm 0.0015$	(1)
$R_*$ ( $R_\odot$ )	$1.115 \pm 0.043$	(1)
$R_p$ ( $R_{\text{jup}}$ )	$1.204 \pm 0.051$	(1)
$i$ (deg)	$86.22 \pm 0.24$	(1)
$P$ (days)	$4.4652934 \pm 0.00072$	(2)
$b$	$0.701 \pm 0.023$	(1)
$R_p/R_*$	$0.11295 \pm 0.00073$	(2)
Eclipse depth at $2.2\mu\text{m}$	$0.109 \pm 0.025\%$	(3)
Eclipse depth at $3.6\mu\text{m}$	$0.080 \pm 0.008\%$	(4)
Eclipse depth at $4.5\mu\text{m}$	$0.135 \pm 0.022\%$	(4)
Eclipse depth at $5.8\mu\text{m}$	$0.203 \pm 0.031\%$	(4)
Eclipse depth at $8.0\mu\text{m}$	$0.238 \pm 0.040\%$	(4)

### 3.2.6 Correction for systematic effects

The lightcurve of HAT-P-1b, corrected for the hot-pixel, diffraction spikes, and normalised with that of the reference star, is shown in Fig. 3.4. Although the eclipse is already visible, the lightcurve is still clearly influenced by systematic effects, which we found to be correlated with the x-position on the detector, the exposure time and the geometric airmass. We fitted for these effects simultaneously with the eclipse depth. Other parameters, such as the background level, were tried, but resulted in no difference in the final lightcurve. For the model of the secondary eclipse, we used the formalism from Mandel & Agol (2002), where all the orbital parameters were kept fixed to the literature values (given in Table 3.1), with the limbdarkening set to 0, and the timing of the secondary eclipse fixed. We did not fit for a time offset, because Todorov et al.

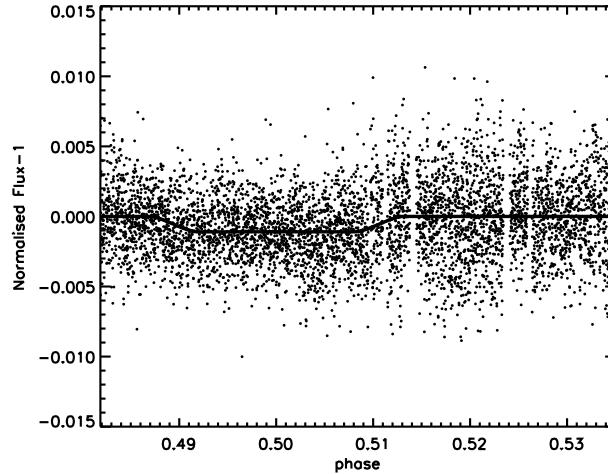


**Figure 3.6** — The lightcurve for the secondary eclipse of HAT-P-1b corrected for systematic effects. Overplotted is our best fitting eclipse model.

(2010) already showed that the timing of the secondary eclipses measured using the Spitzer Space Telescope shows no indication of any offset, using higher signal-to-noise data.

We performed the fit both using the standard multi-linear regression algorithm in IDL (`regress.pro`) as well as using a Monte-Carlo Markov Chain (MCMC) analysis. After an initial fit, we performed a clipping of the residuals by excluding all points within bins of 38 pixels, for which the binned value deviate by more than  $1.5 \cdot 10^{-3}$ . In this way we removed 228 unbinned points. After this clipping we performed an MCMC analysis. For the MCMC analysis, we created 5 chains with a length of 2 million steps each, using different starting positions. We trimmed away the first 200,000 points of each chain, to make sure that the initial starting point no longer influences the measured parameters.

The best fitting model, overplotted on the data, is shown in Fig. 3.4, while the contributions for the individual components are shown in Fig. 3.5.

### 3.3 Results

The final, corrected lightcurve is shown in Fig. 3.6, with its binned (by 41 points) version in Fig. 3.7. Assuming pure, white, Gaussian noise, we find an eclipse depth of  $0.1089 \pm 0.01\%$  ( $11\sigma$ ). However, clear residual systematic effects are visible in the binned lightcurve. The level of this red noise was estimated by comparing the standard deviation in the unbinned data with that of gradually increased binned lightcurves. From this we estimate a red noise component at the level of  $0.023\%$ , which we added in quadrature to our eclipse depth uncertainty to become  $0.109 \pm 0.025\%$ . We also performed the residual permutation (“Prayer Bead”) method (e.g. Gillon et al. 2007), where we add the best fit model to the residuals, after shifting the residuals by  $N$ -points. Points are wrapped around when performing the shift. By refitting the data for all possible shifts between 0 and the number of data points, and measuring the best-fit eclipse depth, we can get an estimate for the true uncertainties in the data. We find a depth of  $0.1089^{+0.024}_{-0.025}\%$ , which is fully consistent with the uncertainties estimated from the red-noise.

This results overall in an eclipse depth of  $0.109 \pm 0.025\%$ , which corresponds to a bright-

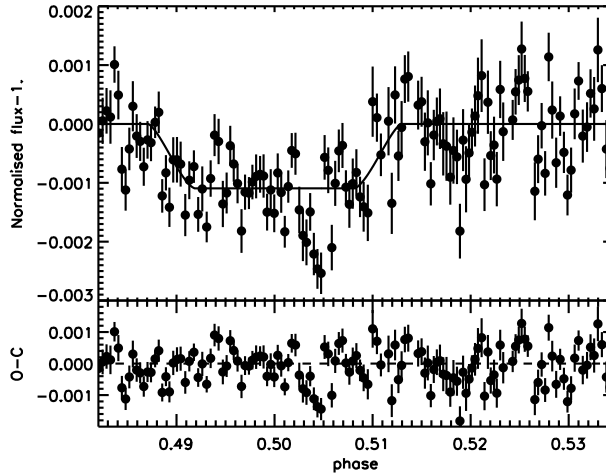


**Figure 3.7** — The same as Fig. 3.6, but binned by 41 points.

ness temperature in the  $K_s$ -band of  $T_b = 2136^{+150}_{-170}$  K. This brightness temperature is significantly higher than the expected equilibrium temperature of this planet, which lies between  $T_{eq} = 1540$  K for an albedo of 0 and inefficient energy redistribution from the dayside to the nightside ( $P_n = 0$ ), and  $T_{eq} = 1190$  K for an albedo of 0.3 and efficient redistribution of energy from the dayside to the nightside ( $P_n = 0.5$ ). The higher brightness temperature could be due to the fact that in the  $K_s$ -band we are looking deeper into the atmosphere, where the layers are warmer.

Todorov et al. (2010) observed the secondary eclipse of HAT-P-1b with the IRAC instrument on board the Spitzer Space Telescope, at 3.6, 4.5, 5.8 and 8.0  $\mu\text{m}$ , and find eclipse depths of  $0.080 \pm 0.008\%$ ,  $0.135 \pm 0.022\%$ ,  $0.203 \pm 0.031\%$  and  $0.238 \pm 0.040\%$  in the different bands respectively. Combining our own measurement of the secondary eclipse in  $K_s$ -band with the IRAC measurements, we can construct a spectral energy distribution (SED) from the near-infrared to the mid-infrared, which is shown in Fig. 3.9, and compare it to atmospheric models.

### 3.3.1 Atmospheric models

We modelled the thermal emission spectra for a few ad hoc cases to try to understand what type of atmosphere would be needed to fit the measured eclipse depths, including our new measurement in  $K_s$ -band. We used a radiative transfer model that can calculate multiple scattering of the thermal radiation, since we included a case with scattering clouds (see below). The scattering is calculated using the doubling-adding method, which makes use of the fact that one can calculate the reflection and transmission properties of a combination of two atmospheric layers from the properties of the individual layers. For each layer in the model atmosphere we started with an optically thin layer with the same scattering properties as the model layer. For the optical thin case analytical expressions are available to calculate the layer transmission and reflection. The thin layer was then doubled several times to match the real optical depth of the model layer. Subsequently, the different model layers were added to calculate the spectra for the entire inhomogeneous atmosphere. For more explanations we refer to Wauben et al. (1994), who describe the model in great detail. Spectra were calculated at 10 different emission angles, from which a disc-averaged spectrum was calculated.

We included absorption of water and CO, whose absorption properties were taken from the

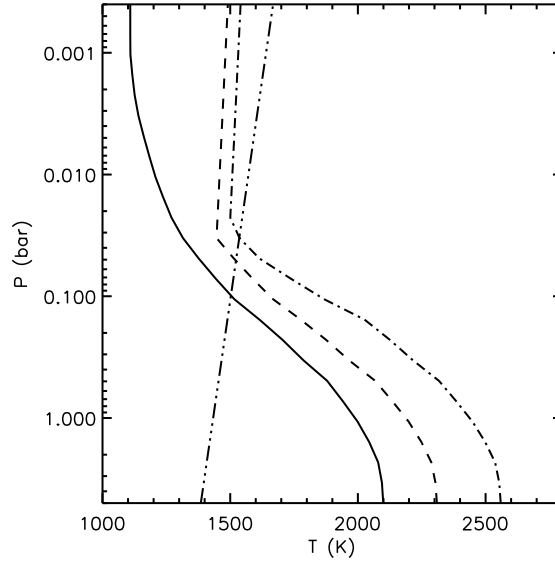


**Figure 3.8** — The temperature-pressure (T-P) profile for the atmospheric models used for modelling the secondary eclipse depth. The solid line shows the uninverted model from Fortney et al. (2008), the dashed-triple dotted line is for a model with an ad-hoc temperature inversion as in Todorov et al. (2010), the dashed line shows the temperature pressure profile for an atmosphere with a normal troposphere and an inversion, and the dash-dotted line is for an atmosphere with Venus-like clouds. The temperatures for the latter profiles are chosen to provide a reasonable fit to the IRAC bands longward of  $4 \mu\text{m}$ .

(old) HITEMP database (Rothman et al. 1995). Although the water data in this database is not the most up-to-date, a line-by-line comparison in K-band with the new HITEMP database (Rothman et al. 2010) yielded only differences many times smaller than the errors on the measured eclipse depths, which we neglect for this qualitative assessment. For speedy calculations, we pre-computed absorption properties at a range of temperatures and pressure using the correlated-k method (Lacis & Oinas 1991) with a spectral resolution of  $0.01 \mu\text{m}$  between  $1.8 \mu\text{m}$  and  $5 \mu\text{m}$  and  $0.1 \mu\text{m}$  between  $5 \mu\text{m}$  and  $10 \mu\text{m}$ , and a Voigt line shape. Assumed mixing ratios of water and CO were  $2 \cdot 10^{-4}$  and  $5 \cdot 10^{-4}$  respectively for all cases.

The models extend from  $1.8 \mu\text{m}$  to  $10 \mu\text{m}$ , and were made for different temperature-pressure (T-P) profiles and compositions. We have made models for the T-P profile for this planet from Fortney et al. (2008), which does not include an inversion layer, as well as for models with an inversion layer. We also varied the composition of the atmosphere and made a model with Venus-like clouds. In Fig. 3.8 we show the temperature-pressure profiles for the different models, and in Fig. 3.9 we show the expected eclipse depths within the observed bands for the different models, binned to a resolution of  $0.1 \mu\text{m}$ .

Fig. 3.9 shows that an atmosphere calculated from first principles (Fortney et al. 2008) cannot reproduce the Spitzer measurements, and that a weak inversion is needed (Todorov et al. 2010). However, a weak inversion throughout the atmosphere produces a very low planet signal in Ks-band, unlike what we derive from our measurements. The reason for this is that Ks-band is a region of very low absorption and hence we see deep in the planet atmosphere, where temperatures are relatively low in the inversion-only case (dashed-triple dotted lines). Contribution

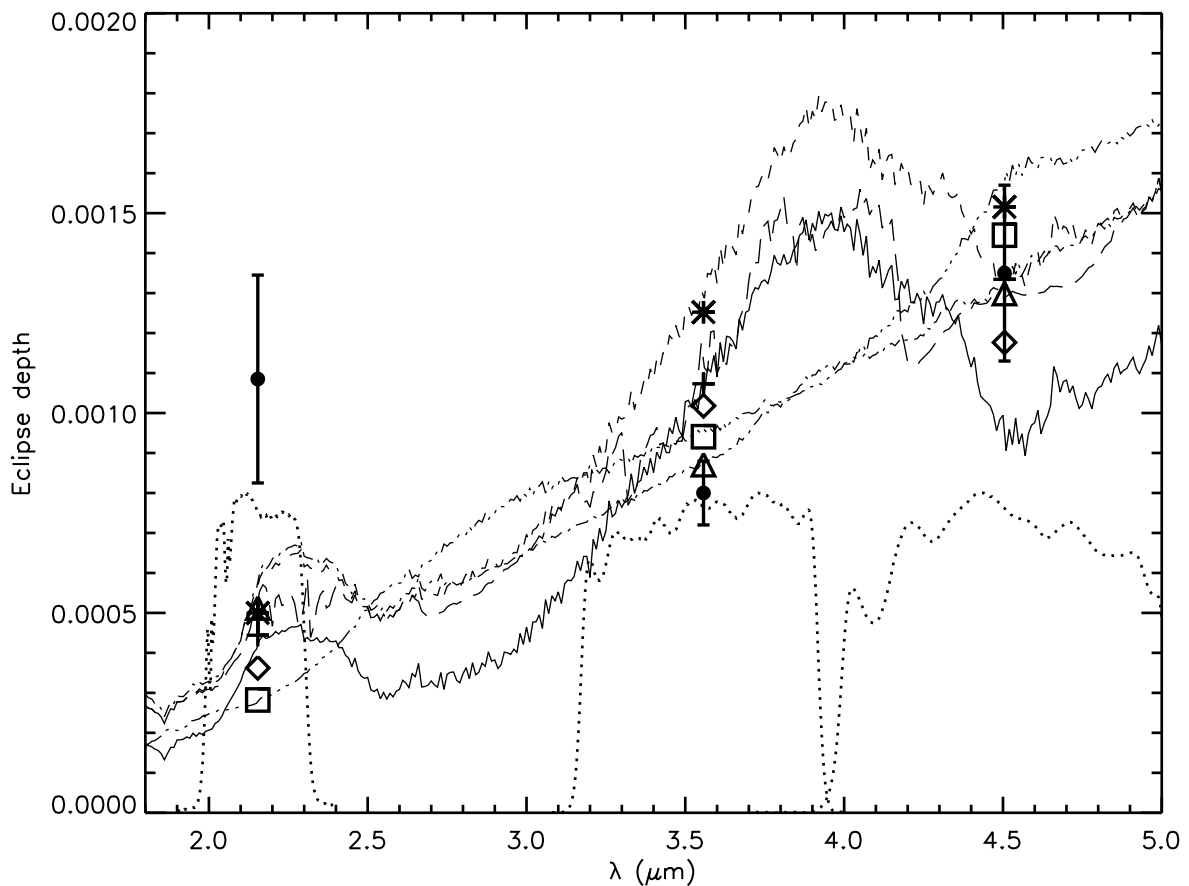


**Figure 3.9** — Models for the emission from the atmosphere of HAT-P-1b, for the T-P profiles of Fig. 3.8, using the same line-style scheme. The symbols indicate the expected flux within the observed bands for the different models, the diamonds are for the non-inverted models, the squares are for the model with the ad-hoc inversion-layer from Todorov et al. (2010), the stars for the model with a troposphere and an inversion layer and the triangles show the expected fluxes for the model with the Venus-like clouds. The points with errorbars indicate the observational data. The dotted lines indicate the transmission curves of the different bands. In addition, a long dashed curve is shown for an atmosphere with the same T-P profile as the short dashed curve, but with a high concentration of methane and carbon-dioxide ( $1 \cdot 10^{-4}$  and  $2 \cdot 10^{-5}$  respectively), the expected fluxes in the different bands for this model are indicate with a crosses.

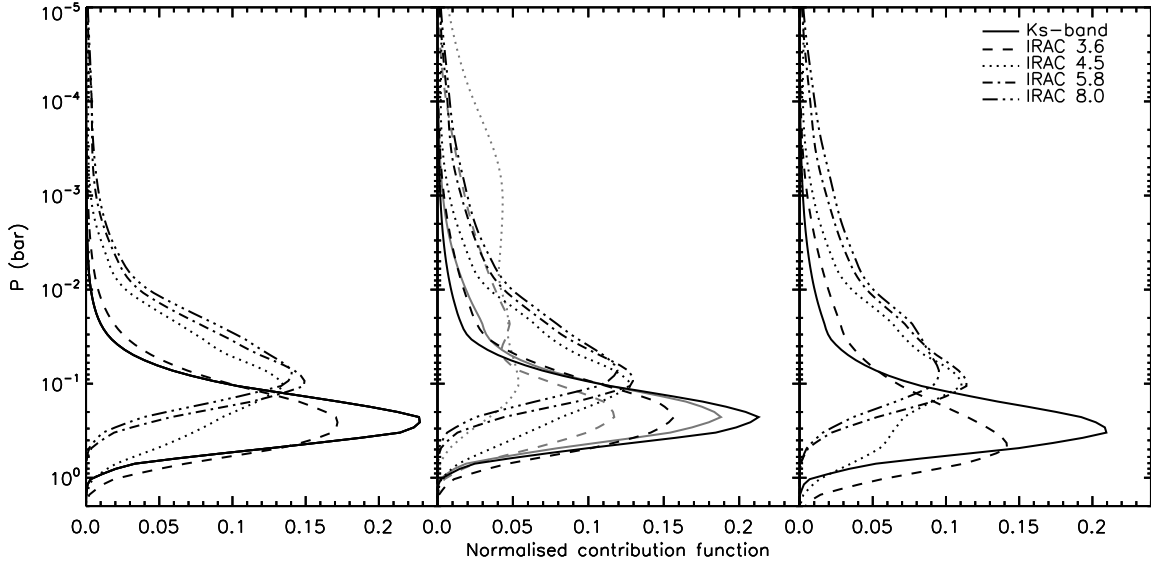


**Figure 3.10** — Normalised contribution functions for the atmospheric emission of HAT-P-1b in the  $K_s$ -band and the different IRAC channels, the different linestyles are now used for different bands. The distribution functions are normalised by their sum. The left panel shows the contribution functions for the non-inverted model from Fortney et al. (2008), the middle panel shows the contribution functions for the models with both a troposphere and an inversion layer, with the light grey lines for the high concentrations of methane and carbon-dioxide, and the right panel shows the same for the ad-hoc temperature inversion used in Todorov et al. (2010)

functions for the different wavelengths are shown in Fig. 3.10. To increase the eclipse depth in  $K_s$ -band the lower atmosphere needs to be made hotter. However, this also increases the eclipse depth in L-band, another spectral region of low absorption (dashed curve in Fig. 3.9). L-band emission can be suppressed somewhat by including large amounts of  $\text{CO}_2$  and  $\text{CH}_4$  (calculated here from HITEMP and HITRAN 2008 (Rothman et al. 2009) data respectively), but this also reduces the signal in  $K_s$ -band (long-dashed curve in Fig. 3.9). Reducing the water or CO abundances also do not produce a better fit. Hence, we cannot fit all data points well using any clear atmosphere with gases that are predicted to be abundant on hot exoplanets. One remedy to fit both the Spitzer data and our  $K_s$ -band eclipse depth is to include a Venus-like cloud. The clouds on Venus are made of concentrated sulphuric acid droplets, which have the property that they are strongly scattering below wavelengths of  $\sim 3\mu\text{m}$  and strongly absorbing above  $3\mu\text{m}$ , with only little variation of extinction with wavelength (e.g. Grinspoon et al. 1993). Because of the scattering nature of the clouds, radiation from Venus' hot lower atmosphere still reaches space at the night side below  $3\mu\text{m}$ , despite an optically thick cloud layer surrounding the planet. Above  $3\mu\text{m}$  the night side emission originates from the clouds. To show this potential effect for HAT-P-1b, we inserted a cloud layer with an optical depth of 1.5 at the tropopause with properties identical to those of Venus'  $1\text{-}\mu\text{m}$  sized cloud-particles. Indeed, brightness temperatures at  $K_s$ -band are higher than anywhere else in Fig. 3.9 and all data points could potentially be fitted well if the lower atmosphere is made even hotter. However, we could not find a physically plausible candidate for cloud materials that could mimic Venus' clouds on a hot exoplanet. So, at present we do not find any suitable atmosphere that could explain the high  $K_s$ -band eclipse

depth.

### 3.4 Conclusion

Using the LIRIS infrared camera on the WHT, we determine the eclipse depth of the extrasolar planet HAT-P-1b in  $K_s$ -band to be  $0.109 \pm 0.025\%$  ( $\sim 4\sigma$ ), with the uncertainties in the eclipse depth dominated by residual systematic effects, as estimated from different reduction/analysis procedures. The measured depth corresponds to a brightness temperature of  $2136_{-170}^{+150}$  K. This brightness temperature is significantly higher than those derived from longer wavelengths, making it difficult to fit all available data points with a plausible atmospheric model. It may be that we underestimate the true uncertainties of our measurements, since it is notoriously difficult to assign precise statistical significance to a result when systematic effects are important.

### Acknowledgements

We are grateful to the staff of the WHT telescope for their assistance with these observations. The William Herschel Telescope is operated on the island of La Palma by the Isaac Newton Group in the Spanish Observatorio del Roque de los Muchachos of the Instituto de Astrofísica de Canarias.

## Bibliography

- Acosta-Pulido, J., Ballesteros, E., Barreto, M., et al. 2002, *The Newsletter of the Isaac Newton Group of Telescopes*, 6, 22
- Alonso, R., Deeg, H. J., Kabath, P., & Rabus, M. 2010, *AJ*, 139, 1481
- Anderson, D. R., Gillon, M., Maxted, P. F. L., et al. 2010, *A&A*, 513, L3+
- Bakos, G. Á., Noyes, R. W., Kovács, G., et al. 2007, *ApJ*, 656, 552
- Burrows, A., Budaj, J., & Hubeny, I. 2008, *ApJ*, 678, 1436
- Charbonneau, D., Allen, L. E., Megeath, S. T., et al. 2005, *ApJ*, 626, 523
- Croll, B., Albert, L., Lafrenière, D., Jayawardhana, R., & Fortney, J. J. 2010a, *ApJ*, 717, 1084
- Croll, B., Jayawardhana, R., Fortney, J. J., Lafrenière, D., & Albert, L. 2010b, *ApJ*, 718, 920
- Croll, B., Lafrenière, D., Albert, L., et al. 2011, *AJ*, 141, 30
- Deming, D. 2009, in *IAU Symposium*, Vol. 253, *IAU Symposium*, 197–207
- Deming, D., Seager, S., Richardson, L. J., & Harrington, J. 2005, *Nature*, 434, 740
- Fortney, J. J., Lodders, K., Marley, M. S., & Freedman, R. S. 2008, *ApJ*, 678, 1419
- Fressin, F., Knutson, H. A., Charbonneau, D., et al. 2010, *ApJ*, 711, 374
- Gibson, N. P., Aigrain, S., Pollacco, D. L., et al. 2010, *MNRAS*, 404, L114
- Gillon, M., Demory, B., Barman, T., et al. 2007, *A&A*, 471, L51
- Gillon, M., Demory, B., Triaud, A. H. M. J., et al. 2009, *A&A*, 506, 359
- Grinspoon, D. H., Pollack, J. B., Sitton, B. R., et al. 1993, *Planet. Space Sci.*, 41, 515
- Hubeny, I., Burrows, A., & Sudarsky, D. 2003, *ApJ*, 594, 1011
- Johnson, J. A., Winn, J. N., Narita, N., et al. 2008, *ApJ*, 686, 649
- Knutson, H. A., Charbonneau, D., Allen, L. E., Burrows, A., & Megeath, S. T. 2008, *ApJ*, 673, 526
- Knutson, H. A., Howard, A. W., & Isaacson, H. 2010, *ApJ*, 720, 1569
- Lacis, A. A. & Oinas, V. 1991, *J. Geophys. Res.*, 96, 9027
- López-Morales, M., Coughlin, J. L., Sing, D. K., et al. 2010, *ApJ*, 716, L36
- Machalek, P., McCullough, P. R., Burke, C. J., et al. 2008, *ApJ*, 684, 1427
- Madhusudhan, N. & Seager, S. 2010, *ApJ*, 725, 261
- Mandel, K. & Agol, E. 2002, *ApJ*, 580, L171
- Rogers, J. C., Apai, D., López-Morales, M., Sing, D. K., & Burrows, A. 2009, *ApJ*, 707, 1707
- Rothman, L. S., Gordon, I. E., Barbe, A., et al. 2009, *J. Quant. Spec. Radiat. Transf.*, 110, 533
- Rothman, L. S., Gordon, I. E., Barber, R. J., et al. 2010, *J. Quant. Spec. Radiat. Transf.*, 111, 2139
- Rothman, L. S., Wattson, R. B., Gamache, R., Schroeder, J. W., & McCann, A. 1995, in *Society of Photo-Optical Instrumentation Engineers (SPIE) Conference Series*, Vol. 2471, *Society of Photo-Optical Instrumentation Engineers (SPIE) Conference Series*, ed. J. C. Dainty, 105–111
- Sing, D. K. & López-Morales, M. 2009, *A&A*, 493, L31
- Spiegel, D. S., Silverio, K., & Burrows, A. 2009, *ApJ*, 699, 1487
- Todorov, K., Deming, D., Harrington, J., et al. 2010, *ApJ*, 708, 498
- Wauben, W. M. F., de Haan, J. F., & Hovenier, J. W. 1994, *A&A*, 282, 277
- Winn, J. N., Holman, M. J., Bakos, G. Á., et al. 2007, *AJ*, 134, 1707



---

## Chapter 4

---

# The GROUSE project III: Ks-band observations of the thermal emission from WASP-33b

*Context.* In recent years, day-side emission from about ten hot Jupiters has been detected through ground-based secondary eclipse observations in the near-infrared. These near-infrared observations are vital for determining the energy budgets of hot Jupiters, since they probe the planet's spectral energy distribution near its peak.

*Aims.* The aim of this work is to measure the K<sub>s</sub>-band secondary eclipse depth of WASP-33b, the first planet discovered to transit an A-type star. This planet receives the highest level of irradiation of all the transiting planets discovered to date. Furthermore, its host star shows pulsations and is classified as a low amplitude  $\delta$  Scuti.

*Methods.* As part of our GROUNd-based Secondary Eclipse (GROUSE) project we have obtained observations of two separate secondary eclipses of WASP-33b using the LIRIS instrument on the William Herschel Telescope (WHT). The telescope was significantly defocused to avoid saturation of the detector for this bright star ( $K \sim 7.5$ ). To increase the stability and the cadence of the observations, they were performed in staring mode. We collected a total of 5100 and 6900 frames for the first and the second night respectively, both with an average cadence of 3.3 seconds.

*Results.* Unfortunately, the first night of data is unsuitable for any eclipse determination because the baseline was too short and a strong stellar pulsation peak occurred during the eclipse. On the second night the eclipse is detected at the  $12 - \sigma$  level, with a measured eclipse depth of  $0.244^{+0.027}_{-0.020}$  %. This eclipse depth corresponds to a brightness temperature of  $3270^{+115}_{-160}$  K. The measured brightness temperature on the second night is consistent with the expected equilibrium temperature for a planet with a very low albedo and a rapid re-radiation of the absorbed stellar light.

E.J.W. de Mooij, M. Brogi, R.J. de Kok, I.A.G. Snellen & M.A. Kenworthy  
To be submitted to A&A

## 4.1 Introduction

In recent years, there have been many measurements of thermal emission from the atmospheres of hot Jupiters, especially in the mid-infrared using the *Spitzer* Space Telescope (e.g. the review by Deming 2009). All the *Spitzer* observations probe the thermal emission of hot Jupiters only redward of the peak of their spectral energy distribution, and thus measure the planet's light in the Rayleigh-Jeans tail of their emission spectrum.

Observations in the near-infrared, on the other hand, typically probe the planet's emission spectrum around or even blue-ward of its peak, and therefore provide essential information on the planet's total energy budget. During the past three years many measurements of planetary emission shortward of  $2.5\mu\text{m}$  have been obtained (Chapters 2 & 3 Sing & López-Morales 2009; Gillon et al. 2009; Rogers et al. 2009; Anderson et al. 2010; Alonso et al. 2010; Gibson et al. 2010; Croll et al. 2010a; López-Morales et al. 2010; Croll et al. 2010b, 2011; Smith et al. 2011; Caceres et al. 2011), most of these in the K-band ( $\lambda=2.15\mu\text{m}$ ) where the planet-to-star contrast is most-favourable for observations with ground-based telescopes through the available atmospheric windows.

From the combination of the measurements at multiple wavelengths, a picture is emerging that there are (at least) two classes of hot Jupiters, one class which shows a thermal inversion in their atmosphere, and a second class which do not. Fortney et al. (2008) propose that the presence of the inversion layer is set by the stellar irradiation, where at high levels of irradiation the planet's stratosphere is hot enough to keep a strongly absorbing compound in the gas phase, while at lower irradiation levels the compound condenses out and disappears from the gas-phase.

Knutson et al. (2010) proposed an alternative scenario for the presence or absence of a strong absorber in the highest layers of the planetary atmosphere. In their scenario the absorber can be destroyed by strong UV emission from the planet's host star, which is caused by the stellar activity. For higher levels of stellar activity, which result in a higher UV flux, the absorbing compound is removed, resulting in a non-inverted atmosphere. Note that the inference of an inversion layer has recently been questioned by Madhusudhan & Seager (2010), who point out that for several planets there is a degeneracy between the atmospheric temperature structure and the chemical composition of the planet's atmosphere.

In this paper we present observations of two secondary eclipses of the very hot Jupiter WASP-33b (Collier Cameron et al. 2010) in  $K_s$ -band. These are part of the GROUNd-based Secondary Eclipse project (GROUSE), which aims to use ground-based telescopes for exoplanet secondary eclipse observations in the optical and near-infrared. As part of this project we have already published our  $K_s$ -band detections of the secondary eclipses of TrES-3b (Chapter 2) and HAT-P-1b (Chapter 3).

WASP-33b is currently the only known planet to transit an A-type star ( $T_{\text{eff}}=7430\pm 100\text{K}$ ) orbiting its host star in  $\sim 1.22$  days. This makes WASP-33b the most irradiated planet known to date, with an irradiation of  $1.2\cdot 10^{10}$  erg/sec/cm<sup>2</sup>. This high level irradiation results in an expected day-side equilibrium temperature of 3250K. Recent observations by Smith et al. (2011) indeed show a very high brightness temperature at  $0.9\mu\text{m}$ . In addition, since the host star is relatively hot, the expected UV flux it receives is also high, approximately  $1.7\cdot 10^5$  ergs/sec/cm<sup>2</sup> for wavelengths short-wards of 1500, making it an ideal candidate to investigate the influence of a high UV flux.

In addition to being the first transiting planet discovered to orbit an A-type star, WASP-33b is also the first planet discovered to transit a pulsating star. In the discovery paper, Collier Cameron et al. (2010) find evidence for non-radial pulsations in their spectral time-series, and tentatively classified WASP-33 as a  $\gamma$  Doradus pulsator, which is a class of non-radial pulsators with periods around 0.3 days and longer (see e.g. Handler & Shobbrook 2002). Recently, Herrero et al. (2011) analysed photometric time series for WASP-33 and found a pulsation period of 67 minutes, which, when converted into the pulsation parameter  $Q$ , the product of the pulsation period and the square-root of the mean stellar density (e.g. Breger 1990; Handler & Shobbrook 2002), is comparable to that of  $\delta$  Scuti stars, and well outside the range of  $\gamma$  Doradus stars. The observed stellar pulsations will have a measurable impact on the transit and eclipse measurements for this planet.

In Sect. 4.2 we present our observations and data reduction. In Sect. 4.3 stellar pulsations and the light curve fitting are presented. Subsequently we discuss the results in Sect. 4.4, and finally we will give our conclusions in Sect. 4.5.

## 4.2 Observations and data reduction

### 4.2.1 Observations

The first secondary eclipse of WASP-33b was observed in the  $K_s$ -band with the Long-slit Intermediate Resolution Infrared Spectrograph (LIRIS; Acosta-Pulido et al. 2002) instrument on the William Herschel Telescope (WHT) on La Palma during the night of August 18, 2010 (hereafter night I). The observations started at 00:45 UT and lasted for  $\sim 4.5$  hours. The weather conditions during the night were photometric, as can be seen from the raw light curves shown in the top panel of Fig. 4.1.

The pixel scale of LIRIS is 0.25 arcsec per pixel, yielding a field-of-view of 4.2 by 4.2 arcminutes, large enough to observe both WASP-33 and a reference star of similar brightness simultaneously. Since WASP-33 is very bright, exposure times of 1.5 seconds were used in order to avoid saturation of the detector. As an additional measure to prevent saturation, the telescope was strongly defocused. This is a well proven strategy also used for other GROUSE observations (Chapters 2 and 3), which should also reduce the impact of flat-field inaccuracies by spreading the light over many pixels. To keep the observations as stable as possible, and in order to reduce the cycle time, the observations were performed in staring mode. Since this method does not allow for background subtraction using the science frames, a set of 297 dedicated sky frames were obtained after the observations for sky-subtraction purposes. A total of 5100 science frames were obtained during the observations and the average cadence was 3.3 seconds. The first three frames of a sequence of frames are known to suffer from the reset anomaly, which is seen as an anomalous structure in the background. These frames are therefore excluded from further analysis, which results in the exclusion of 106 frames during this night.

On the night of September 20, 2010 (hereafter night II) another eclipse of WASP-33b was observed from 22:35 UT to 05:00UT. During the first part of the observations the conditions were photometric, however during the last few hours of the observations occasional clouds moved across the image, absorbing up to 65% of the light (see Fig. 4.1). The observational strategy was identical to that of the first night. In short, an exposure time of 1.5 seconds was

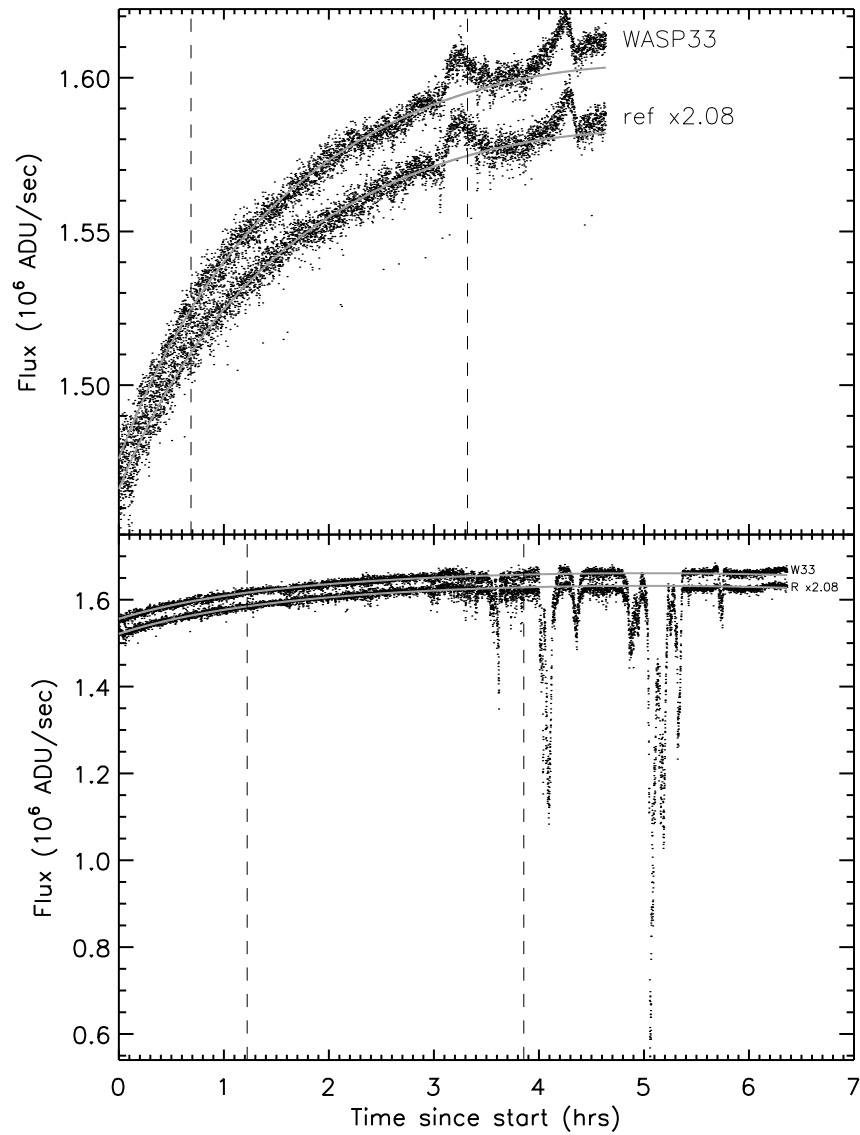


**Figure 4.1** — Raw lightcurves for WASP-33 and the reference star (multiplied by 2.08 for plotting purposes) for the night of August 18, 2010 (top panel) and for the night of September 20, 2010 (bottom panel). The vertical dashed lines indicate the expected beginning and end of the targeted eclipse. The solid, grey, lines show the airmass during the nights, scaled to match the stellar flux in the first hour of the observations.

used, the telescope was defocused, and the observations were performed in staring mode, with a separate set of 162 images at the end of the observations for background subtraction. A total of 6900 science frames were obtained with an average cadence of 3.3 seconds per frame. As with the first night the first three frames of every sequence were excluded (207 frames in total), since they suffer from the reset-anomaly.

## 4.2.2 Data reduction

The data-reduction for both nights was performed in the same way. All frames were corrected for crosstalk along rows of the detector, which is present at a level of  $10^{-5}$  of the total flux along the rows of all four quadrants. Subsequently we performed a non-linearity correction on all the frames using our own non-linearity measurements which were created from a set of dome-flats at a constant level of illumination but with varying exposure times. After these corrections all the images were flat-fielded using a flat-field created from bright and dark twilight flats.

A background map was constructed from the set of dithered images obtained after the eclipse observations. These images were reduced in the same way as the science images, and, after filtering out the discrepant pixels in time to remove (faint) stars, were subsequently combined. The resultant background map was then scaled and subtracted from the individual science images.

After background subtraction, aperture photometry was performed on both WASP-33 and the reference star using an aperture of 18 and 26 pixels for night I and night II respectively. Any residual sky background was determined in annuli between 30 and 50 pixels for night I and between 40 and 60 pixels for night II. The flux in the annuli was clipped at  $5\sigma$  to avoid outliers in the background (such as hot pixels) from affecting the data. Finally, the light curve of WASP-33 was normalised with that of the reference star, and the resultant light curves for the two nights are shown in the top panels of Figs. 4.3 and 4.4.

## 4.3 Correction for systematic effects and stellar pulsations

### 4.3.1 Stellar pulsations

In the discovery paper Collier Cameron et al. (2010) note that the host star of WASP-33b is a non-radial pulsator, possibly belonging to the  $\gamma$  Dor class of variable stars. Herrero et al. (2011) obtained observations of the star and found a dominant period of 68.5 minutes, which, using the criterion on the Q value (see Handler & Shobbrook 2002), leads them to classify the star as a probable  $\delta$  Scuti pulsator. Recently, Smith et al. (2011) observed a secondary eclipse of WASP-33b in a narrowband filter at  $0.91\mu\text{m}$ , and found three pulsation periods in their data, at 53.62, 76.52 and 41.85 minutes, all with amplitude between 0.4 mmag and 0.9 mmag.

For our data, the stellar pulsations are clearly visible in the light curve for night I, while for night 2 the variability is less apparent. In order to determine the period(s) of the stellar pulsations, a periodogram of the light curves was created. Since the planetary eclipse signal and possible systematic effects can influence the periods found in the data, both a scaled eclipse model as well as a model for the systematics based on instrumental effects (see section 4.3.2) were fitted to the data using a simple linear regression algorithm and subsequently subtracted

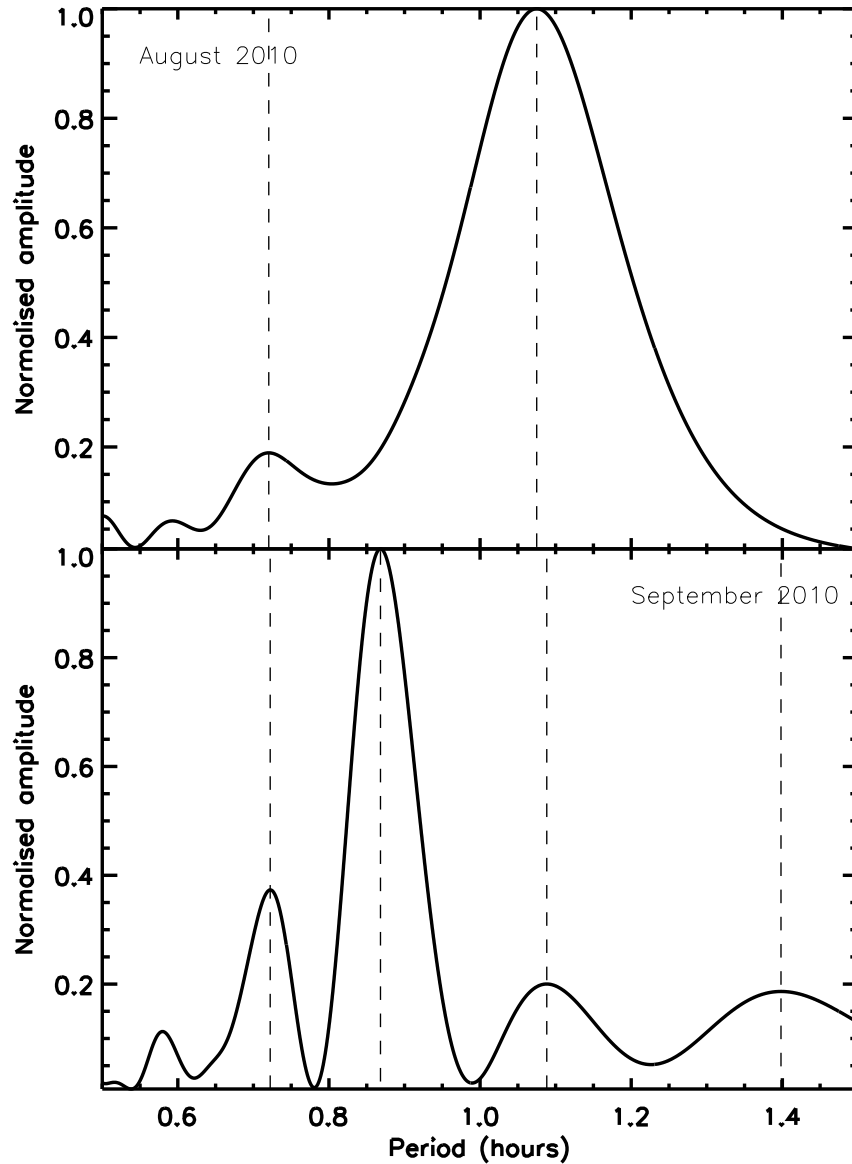


**Figure 4.2** — Normalised periodograms of the light curves for the two separate nights. The top panel shows the periodogram for night I and the bottom panel shows the periodogram for night II.

before determining the periodogram. The generalised Lomb-Scargle formalism from Zechmeister & Kürster (2009) was used to construct the periodogram, and the results for both nights are shown in Fig. 4.2.

For night I the strongest peak in the periodogram is found at a period of 64.5 minutes, and there is a weaker peak at 43.2 minutes. For night II, there are four peaks visible, the strongest peak is found at 52.1 minutes, while three weaker peaks are found at 43.3, 65.3 and 83.9 minutes. In both datasets we find a periodic signal at  $\sim 65$  minutes, which differs from the period of 68.5 minutes found by Herrero et al. (2011). However, the short time span covered during each night is not sufficient to get a very tight constraint on the period, and therefore the periods could be consistent with 68.5 minutes. The  $\sim 43$  minute period is seen in the measurements from both our nights, as well as in the data from Smith et al. (2011). The period around  $\sim 52$  minutes is

**Table 4.1** — Fitted parameters and uncertainties from the MCMC analysis of the lightcurves of WASP-33b, for the method where the systematic effects are fit with instrumental parameters (x-position, airmass and sky level) and for the method where a polynomial ( $c_1$  to  $c_3$ ) is used to correct the baseline.  $P_1$  to  $P_4$  are the periods used for the stellar pulsations, and  $A_1$  to  $A_4$  are the corresponding amplitudes.

Parameter	unit	Night 1		Night 2	
		Ins.Pars.	Poly	Ins.Pars.	Poly
$F_p/F_*$	(%)	$0.140\pm 0.007$	$0.092\pm 0.017$	$0.245\pm 0.009$	$0.246\pm 0.018$
x		$0.06\pm 0.01$	—	$-0.12\pm 0.02$	—
airmass		$-0.76\pm 0.03$	—	$0.34\pm 0.03$	—
sky		$0.27\pm 0.03$	—	$-0.53\pm 0.03$	—
$c_1$		—	$0.42\pm 0.01$	—	$0.10\pm 0.01$
$c_2$		—	$-0.09\pm 0.02$	—	$-0.01\pm 0.02$
$c_3$		—	$0.10\pm 0.01$	—	$-0.13\pm 0.01$
$P_1$	(minutes)	$63.95\pm 0.39$	$62.00\pm 0.51$	$52.65\pm 0.39$	$52.28\pm 0.51$
$P_2$	(minutes)	43.22 (fixed)		43.34 (fixed)	
$P_3$	(minutes)	—		65.29 (fixed)	
$P_4$	(minutes)	—		83.90 (fixed)	
$A_1$	(%)	$0.095\pm 0.004$	$0.082\pm 0.005$	$0.056\pm 0.006$	$0.058\pm 0.006$
$A_2$	(%)	$0.041\pm 0.004$	$0.042\pm 0.004$	$0.017\pm 0.005$	$0.014\pm 0.005$
$A_3$	(%)	—		$0.011\pm 0.006$	$0.011\pm 0.006$
$A_4$	(%)	—		$0.031\pm 0.006$	$0.013\pm 0.006$

found in both our second night of data as well as in the data from Smith et al. (2011), although there it is not the dominant frequency. We caution, however, that the periodograms used for the frequency analysis were created with data that was only partially corrected for systematic effects, and therefore can still be influenced by residual (quasi) periodic systematic effects.

### 4.3.2 Light curve fitting

Since the light curve is the result of a combination of three effects, the stellar variability, systematic effects related to both the instrument and the Earth's atmosphere and the secondary eclipse of WASP-33b, a fit for all three effects is performed simultaneously.

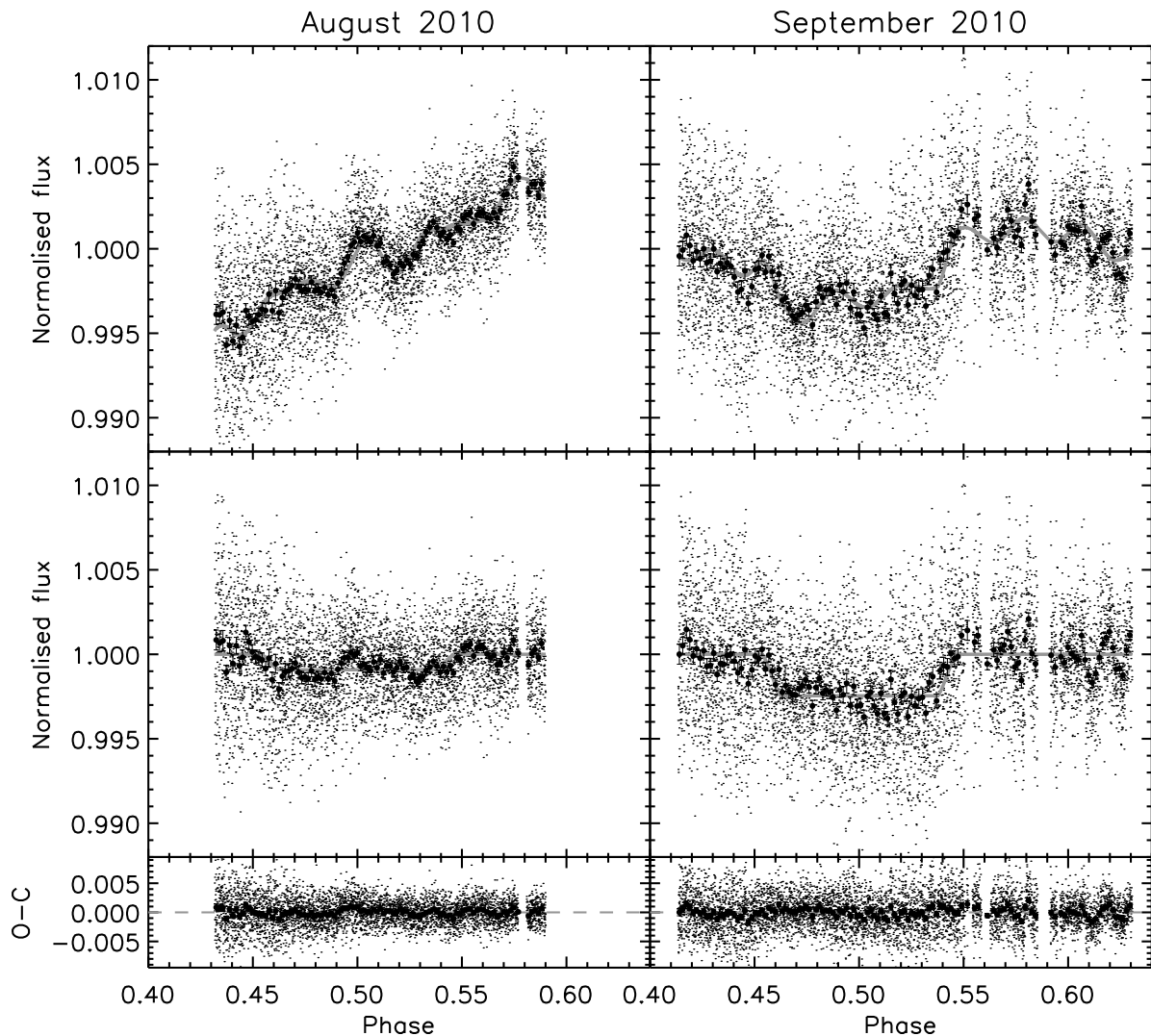


**Figure 4.3** — Light curves for the secondary eclipse of WASP-33b for the night I (left panels) and night II (right panels). Top panels: the light curves of WASP-33 normalised with those of the reference star, overplotted is the best fitting 'full' model with a low order polynomial baseline correction, stellar pulsations and the eclipse. Middle panels: The light curves corrected for the trends in the baseline and stellar pulsations, clearly showing the transit. Bottom panels: The residuals after subtracting the best-fit model. The thick points with errorbars in these figures show the data binned by 50 points.



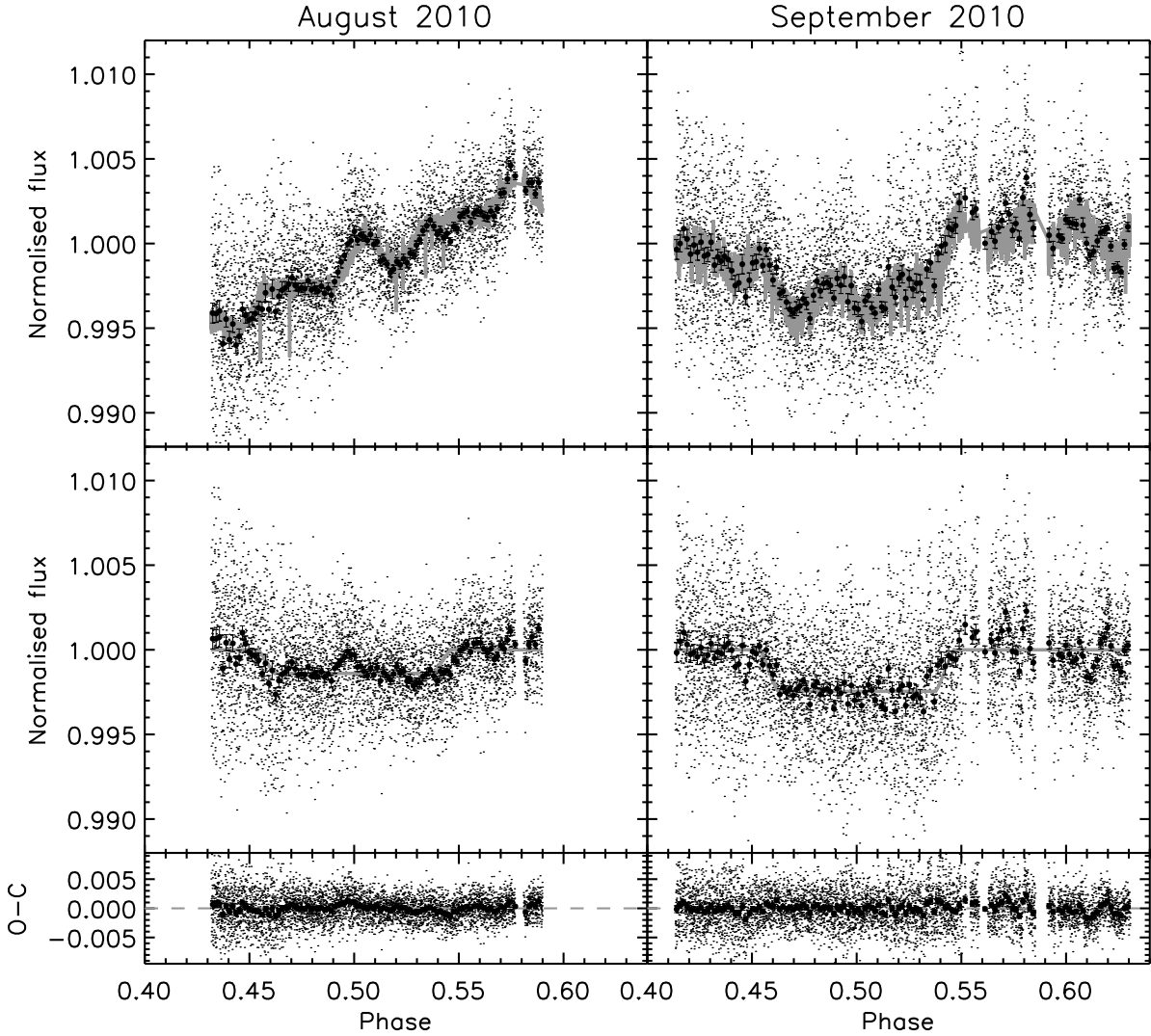


**Figure 4.4** — Same as Fig. 4.4 but the systematic effects are now modelled by linear relations with instrumental parameters.

For the stellar pulsations the period of the dominant mode is left as a free parameter, although with a penalty for the  $\chi^2$  of the form  $(P-P_0)^2/\sigma_p^2$ , with  $P_0$  the period determined from the periodogram, and  $\sigma_p$  set to 1 minute. The period of the other mode(s) was kept fixed to periods found in the analysis of the periodogram as described in the previous section. For all the modes the offset in phase and the amplitude of the pulsations were allowed to vary freely.

For the fitting of systematic effects two different methods were used, for the first method, the systematic effects are considered to be due to the change of position on the detector, the airmass and the difference in sky background between the two quadrants. This is similar to what was used in the previous papers from the GROUSE project (Chapters 2 and 3). In the second method, the systematic effects are modelled using low order polynomials, as also used in Chapter 5 for the near-infrared transit observations of GJ1214b.

The secondary eclipse was modelled using the Mandel & Agol (2002) formalism. We used the parameters from Collier Cameron et al. (2010) for the impact parameter, semi-major axis,

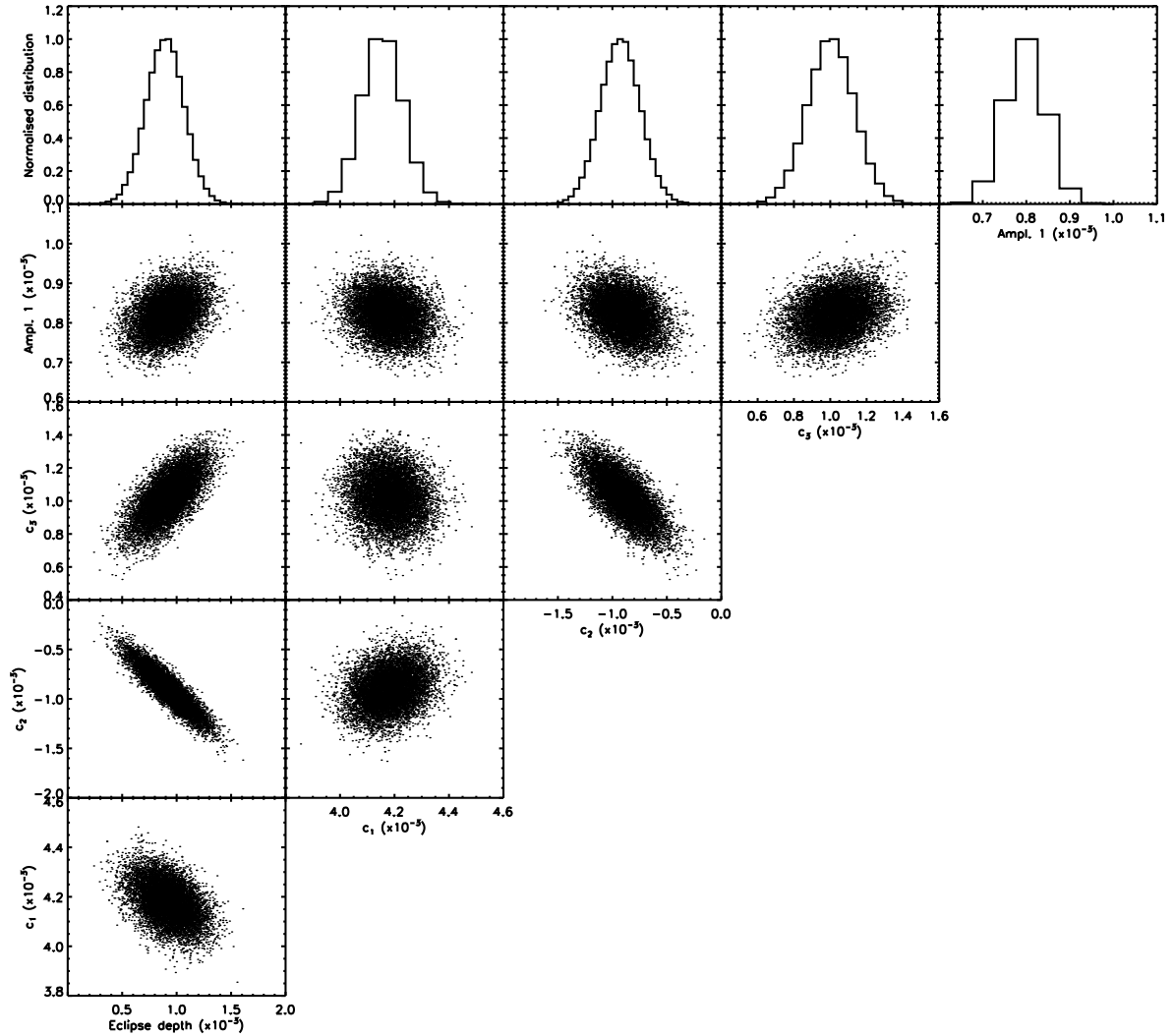


**Figure 4.5** — Correlations between different parameters from the MCMC analysis for night I. The baseline is modelled using a polynomial with coefficients  $c_1$  to  $c_3$ . The correlation between the parameters and the amplitudes of the stellar pulsation at lower significance are not shown, since their impact on any of the measured parameters will be minimal.

orbital period and planet-to-star size ratio, while the orbit of the planet is assumed to be circular. This assumption is reasonable since the planet orbits extremely close to its host star, which should result into a rapid damping of eccentricity. In addition, on the second night an eclipse-shaped dip in the light curve centered on  $\phi \sim 0.5$  is readily visible (see the right panel of Fig. 4.3).

In total the light curves were fitted with 9 free parameters (1 for the eclipse, 3 for the systematic effects and 5 for the stellar pulsations) for night I and 13 free parameters for night II, due to 2 additional periods found in the data. The fitting was done using a Markov-Chain Monte Carlo method, and the two nights were fitted separately. Per night 5 sequences of 2 million steps were generated, and after trimming the first 200,000 points to avoid any contamination from the initial conditions, and checking that the chains were well mixed (Gelman & Rubin 1992), these 5 chains were combined to give the final results.

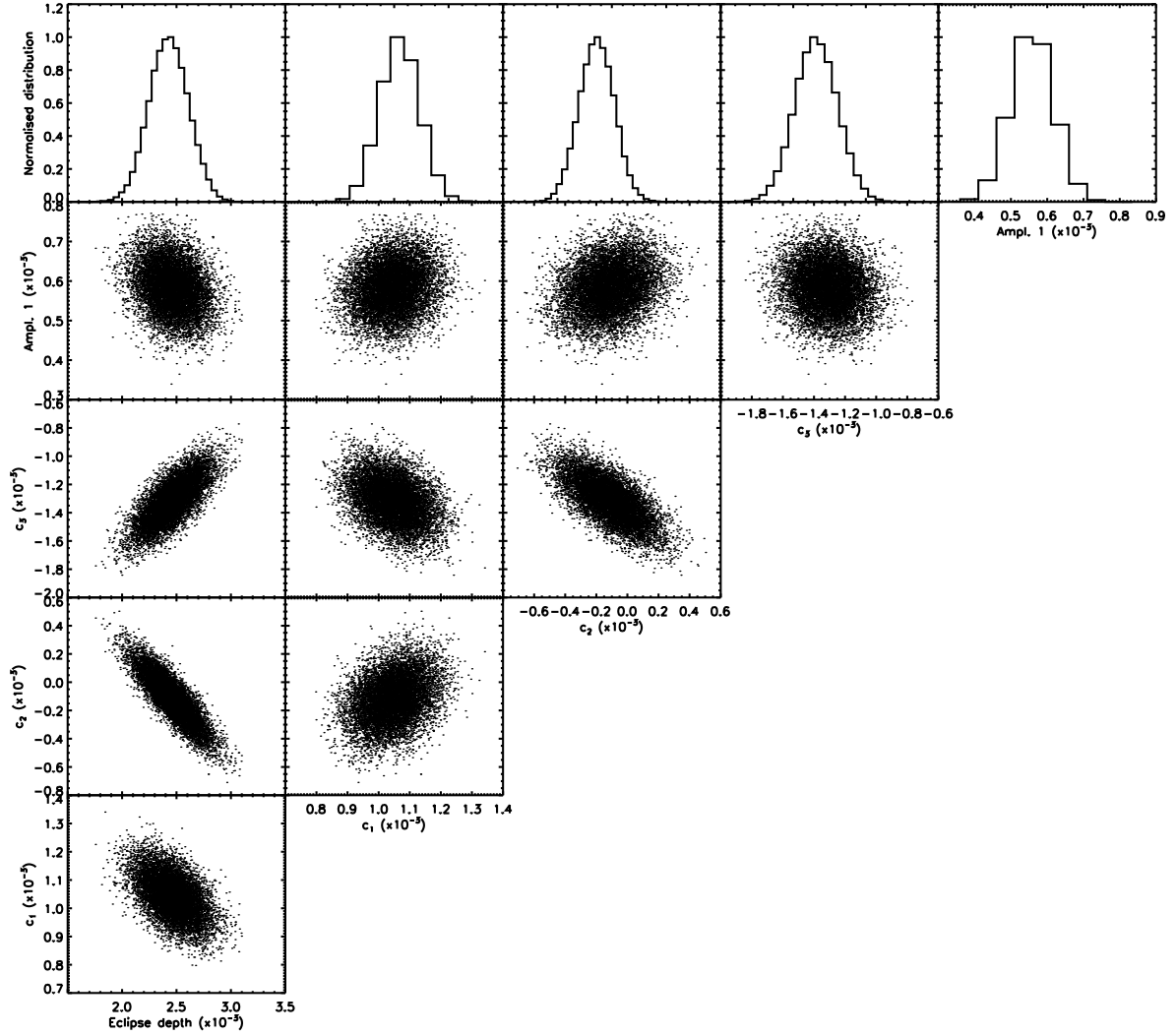


**Figure 4.6** — same as Fig. 4.5 but now for night II

Before fitting, outliers were removed by excluding all points that were more than 0.9% away from a median smoothed light curve, as well as all points for which the flux of the individual stars, corrected for airmass, dropped below 90%. In this way a total 21 and 414 points were excluded during the first and second night respectively. In addition, there is a feature present in both light curves at the same time after the start of the observations (after  $0.1795 \pm 0.0025$  days) that is not at an identical point during the planet’s orbit and therefore most likely due to an, as yet, unidentified instrumental effect. Excluding all the points that were obtained during this feature removes an additional 128 frames.

The best fit values of the eclipse depth for night I are  $0.140 \pm 0.007\%$  and  $0.092 \pm 0.017\%$  for the fit with instrumental parameters and polynomials respectively, while for night II the best-fit eclipse depths are  $0.245 \pm 0.009\%$  and  $0.245 \pm 0.018\%$  for the two respective cases. The results for the different fits can also be found in Table 4.1.

The difference in fits both between the two different nights as well as the differences for the first night between the two different fit methods are larger than the uncertainties in the eclipse depth as estimated from the MCMC analysis. This difference can mainly be attributed

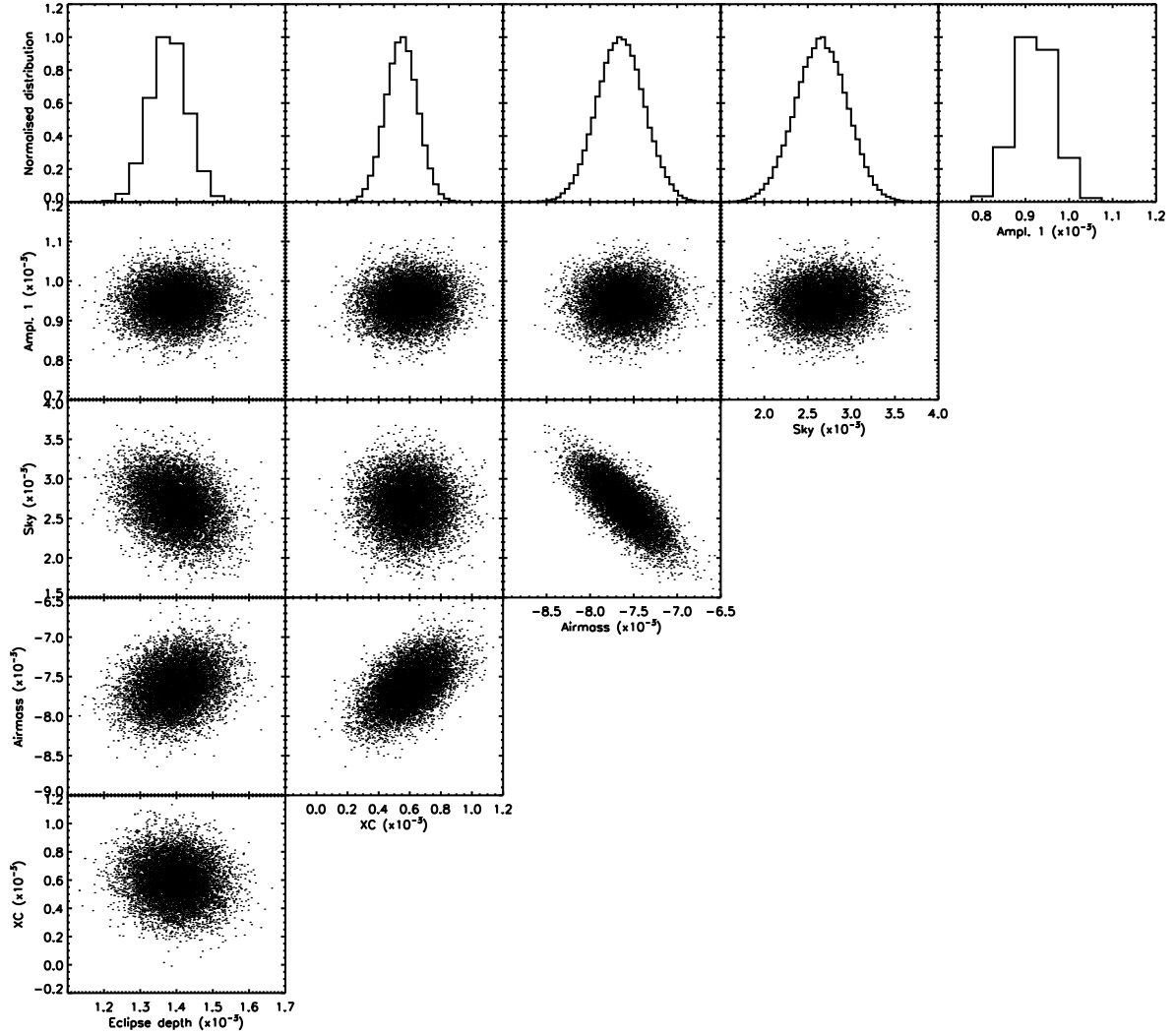


**Figure 4.7** — Correlations between different parameters from the MCMC analysis for night I. The baseline is modelled using the observed instrumental parameters. The correlation between the parameters and the amplitudes of the stellar pulsation at lower significance are not shown, since their impact on any of the measured parameters will be minimal.

to the relatively short out-of-eclipse baselines available for the first eclipse observation, which hamper the removal of the systematic effects from both the stellar pulsations as well as from the instrumental and atmospheric effects. This is clearly illustrated when looking at the correlations between the parameters used for the removal of the systematics and the eclipse depth, as shown in Figs. 4.5 to 4.8. Furthermore, the first night appears to suffer from a strong peak due to stellar pulsations right in the middle of the eclipse, which is not fully correctable. We therefore conclude that the first night of data is too unreliable for an eclipse measurement.

As a first step to assess the impact of correlated noise, we redid the analysis for the second night after binning the data by 50 points ( $\sim 3$  minutes). Although overall the parameters are the same, we find larger uncertainties in the eclipse depths with the best-fit values of  $0.255 \pm 0.028\%$  and  $0.242 \pm 0.035\%$  for the fit with instrumental parameters and polynomials respectively. To assess the impact of (uncorrected) red noise on the measured eclipse depths in another way,

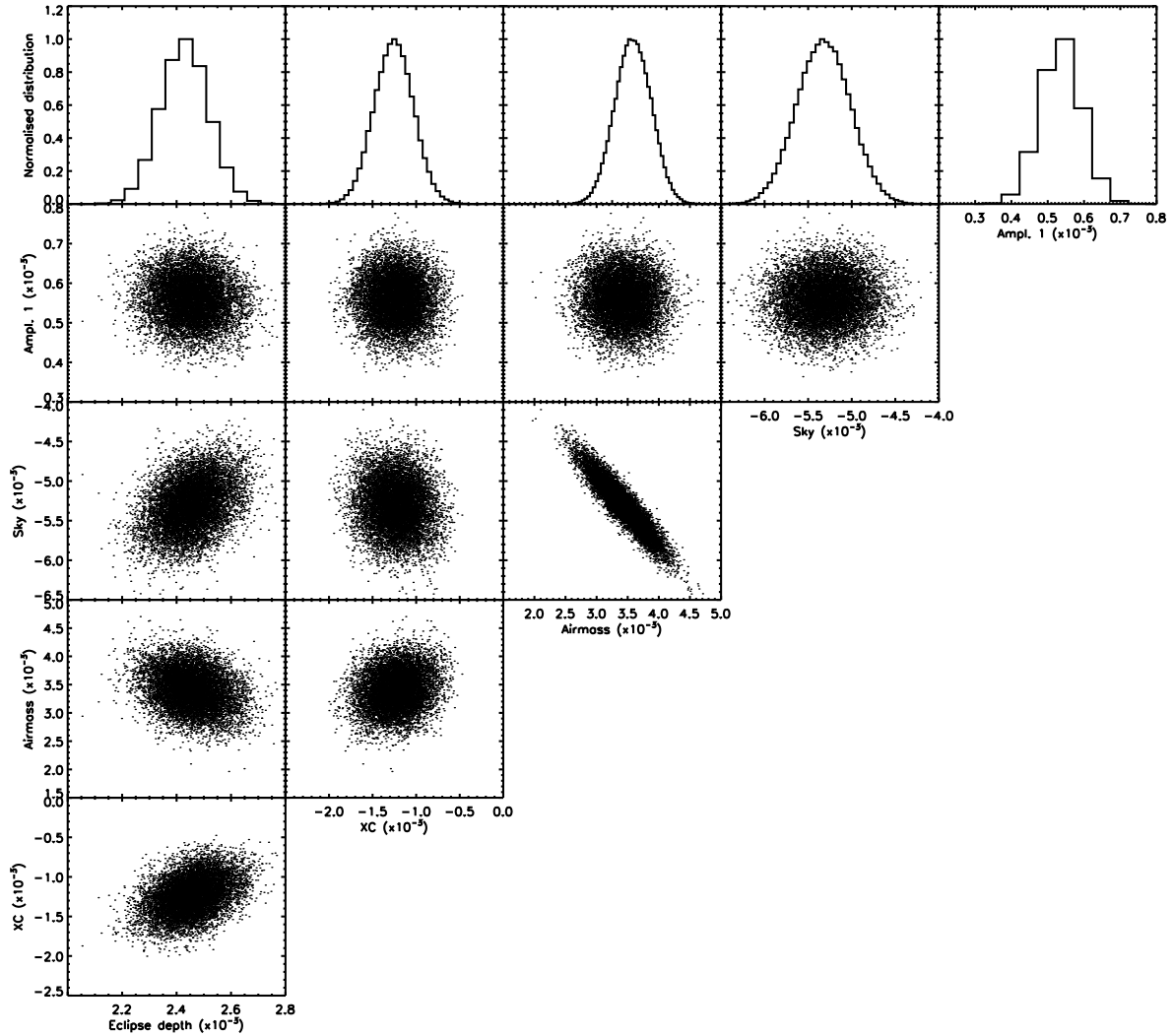


**Figure 4.8** — same as Fig. 4.7 but for night II

the residual permutation method was used. To assess the uncertainties the best fit model is subtracted from the light curve, and these residuals are then shifted by  $n$  points, wrapping the light curve around, so that the points that are shifted beyond the end of our observations are again inserted at the beginning. The best fit model is then added back to the data, and this new light curve is fitted again. The interval between 16% and 84% of the distribution of the best-fitting eclipse depths is used for the uncertainties on the eclipse depth. To speed up the residual permutation analysis, instead of adding back the full model, which includes the stellar pulsation, trends in the baseline and eclipse depth, we only used the trends in the baseline and eclipse depth, since the correlation between the parameters for the stellar pulsations and the eclipse depth is weak. From the residual permutation analysis we also find larger uncertainties for both decorrelation methods, with eclipse depths of  $0.244^{+0.027}_{-0.020}\%$  for a baseline fitted with instrumental parameters and  $0.249^{+0.033}_{-0.052}\%$  for a polynomial baseline fit. In all cases the uncertainties are higher than for the MCMC analysis of the unbinned data but comparable to the MCMC analysis of the binned data, which is expected if there is red noise present.

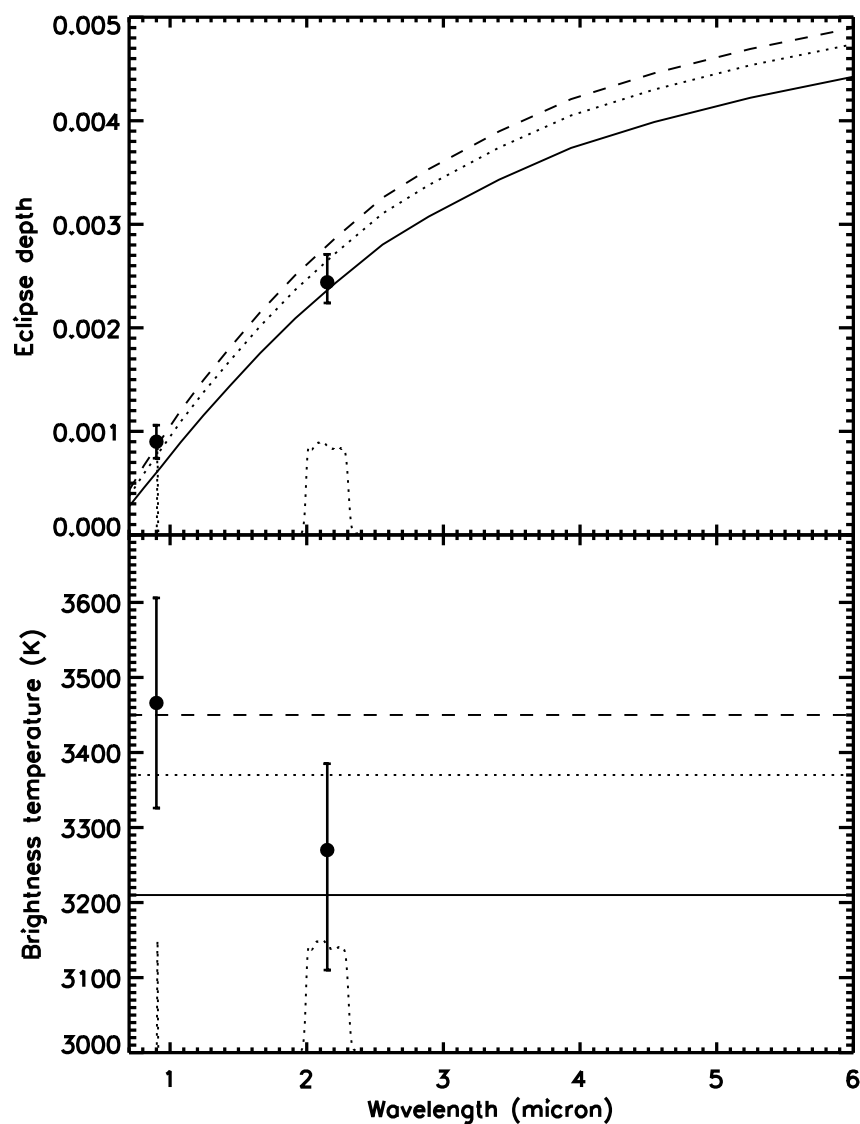


**Figure 4.9** — Spectral energy distribution of WASP-33b. Top panel: Eclipse depths in  $K_s$ -band (this work) and in the  $SII_{0.91\mu m}$ -filter from Smith et al. (2011). Bottom panel: brightness temperatures in the two bands. Overplotted in both panels are the expected eclipse depths/brightness temperatures for a zero-albedo homogeneous day-side (solid line), for an instantly re-radiating day-side (dashed line) and for the best-fit effective temperature (dotted line).

## 4.4 Results and discussion

As already mentioned in the previous section there is a large discrepancy in the eclipse depth measured on the two separate nights. It is clear from Figs.4.3 and 4.4 that the fit for the first night is poor, which is most likely due to a combination of uncorrected stellar pulsations and the short out-of-eclipse baseline available on that night. We therefore opt to not use the measurement of night I, and only use the measurement made during the second night for the rest of this paper. Furthermore, since there is a strong correlation between the coefficients for the polynomial baseline fit and the eclipse depth (see Fig. 4.6), we use the fit of the baseline with instrumental parameters for the remainder of the paper, since the correlation between different parameters is much weaker. We note that the polynomial baseline correction for this night gives the same eclipse depth, however with a larger uncertainty.

The measured eclipse depth of  $0.244^{+0.027}_{-0.020}$  % corresponds to a brightness temperature in the  $K_s$ -band of  $3270^{+115}_{-160}$  K. This brightness temperature was calculated using the solar-metallicity NextGen models (Hauschildt et al. 1999) interpolated to the stellar parameters of WASP-33 determined by Collier Cameron et al. (2010) ( $T_{\text{eff}}=7430\text{K}$ ,  $\log(g)=4.294$ ).

Currently there is only one other measurement available of a secondary eclipse of WASP-33b. This measurement by Smith et al. (2011), obtained in a narrowband filter at  $\sim 9100\text{\AA}$ , shows a depth of  $0.09\pm 0.016\%$ , which corresponds to a brightness temperature of  $3466\pm 140$  K. This narrow-band measurement probes the spectral energy distribution at the peak, and is therefore complementary to our  $K_s$ -band observations, which probes the SED in the Rayleigh-Jeans tail (Fig. 4.9).

If we assume that the SED can be well fit with a single blackbody function, we find an effective temperature for the combined measurements of  $T_{\text{eff,p}}=3370^{+95}_{-100}$  K.

As can be seen in the middle right panel of Fig. 4.4, the eclipse appears to end earlier than expected from the model. Although systematic effects are the most likely cause of this, it is worth noting that a narrower width of the eclipse would indicate that the orbit of WASP-33b is eccentric. If this is the case, by combining the ratio between the transit and secondary eclipse durations with the time of mid-eclipse, a direct measurement of both the eccentricity and the argument of periastron is possible (e.g. Charbonneau et al. 2005). Although a full fit is beyond the scope of this work, we can estimate the change in duration from the light curve. The duration of the secondary eclipse is shorter than the transit duration by 0.01 in phase, which corresponds 90% of transit duration. From this we estimate  $e\sin(\omega)\sim 0.05$ . Since the ingress appears to be at the expected time, the time of mid-eclipse is in this case also slightly earlier than expected. From the shift we estimate  $e\cos(\omega)\sim 0.008$ . Combining these two estimates we find an eccentricity of  $\sim 0.05$ . We again caution that systematics can easily give rise to an apparent non-zero determination of the eccentricity, which is for instance seen for the secondary eclipse of TrES-3b (Chapter 2, Fressin et al. 2010; Croll et al. 2010b). We therefore do not advocate this non-zero eccentricity scenario based on these data.

### 4.4.1 A low albedo and rapid re-radiation of incident light

Both currently available eclipse measurements for WASP-33b point towards a very hot day-side temperature. If we assume that the measured brightness temperatures are representative of WASP-33b's equilibrium temperature, and are not generated deep inside the planets atmo-

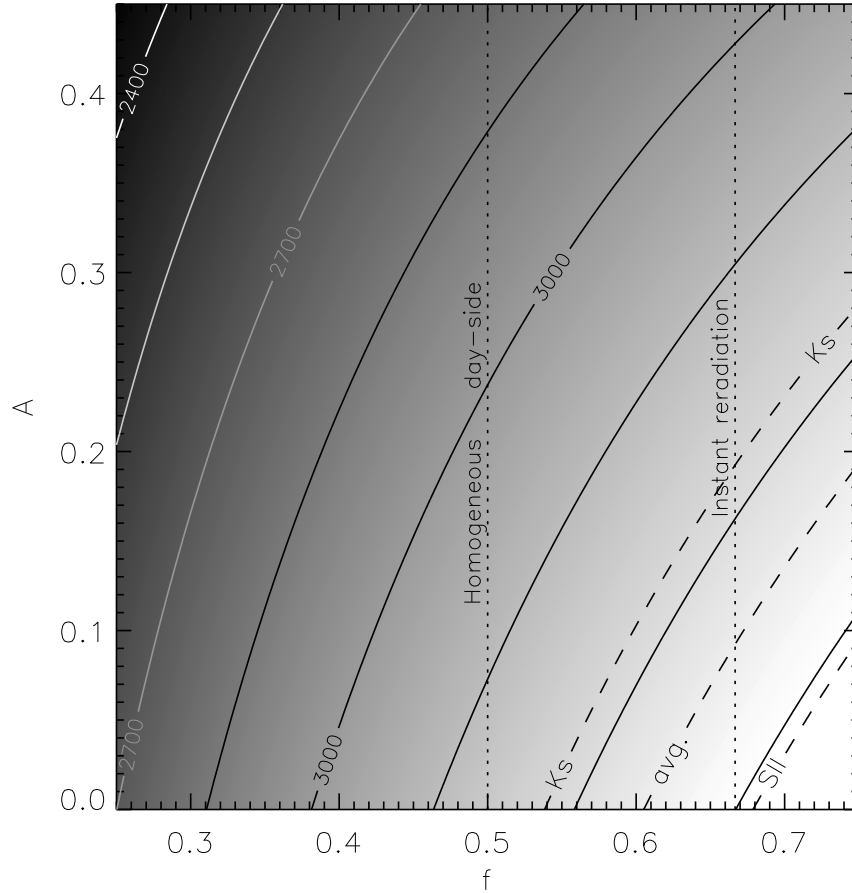


**Figure 4.10** — Equilibrium temperature of WASP-33b for different albedo and re-radiation factors. Solid contours show lines of constant temperatures and 150 K intervals. Overplotted are lines of constant temperature for the measured brightness temperatures (dashed lines), labeled with the bandpass they were observed in. The dashed line labeled “Avg.” indicates the line for constant temperature of the effective temperature determined from the two measurements. Vertical (dashed) lines indicate the reradiation factors for a homogeneous day-side temperature ( $f=1/2$ ), and for an instantly reradiating day-side ( $f=2/3$ ).

sphere, where the temperatures are high, we can constrain the reradiation factor and albedo. For the reradiation factor we used the  $f$  description, as for instance used by López-Morales & Seager (2007), which also allows for the case of an inhomogeneous temperature distribution on the day-side (for instant re-radiation  $f=2/3$ ).

In Fig. 4.10 we show a simple model of the equilibrium temperature as a function of albedo and reradiation factor. In this figure we show the contours of constant equilibrium temperature as a function of albedo and reradiation factor. In addition we show lines of constant temperature for the measured brightness temperatures, as well as for the effective temperature determined from these measurements. As can be seen the measurements require a very low albedo and a very short reradiation time scale, such that all the stellar flux is absorbed and rapidly reradiated without having time to advect to the night-side of the planet. This is consistent with the findings of Cowan & Agol (2011), who study the albedo and redistribution efficiencies for a large sample of hot Jupiters, and find that the hottest planets (in their sample) have a low albedo and a low efficiency of the advection of absorbed stellar flux to the planet’s night side.



The very low redistribution efficiency suggests that the planet has an inversion layer, where the re-radiation timescales are short (Fortney et al. 2008). Knutson et al. (2010) hypothesise that an increase in the UV-flux from an active star, especially in Lyman  $\alpha$ , can cause a shift in the photochemistry such that the efficient absorber is removed from the gas-phase. The high incident UV-flux on WASP-33b, which appears to have an inversion layer, would argue against this, although the flux in its Lyman  $\alpha$  line is relatively modest. To investigate the influence of the UV-radiation, photochemical modelling will be necessary (e.g. Zahnle et al. 2009).

## 4.5 Conclusion

We have presented our results of  $K_s$ -band observations of the secondary eclipse of WASP-33b, the most irradiated planet known to date. Although we have two nights of observations, the measurements on the first night suffer from strong residual systematics that cannot be fully corrected due to the short out-of-eclipse baseline. The measured eclipse depth for the second night is  $0.244^{+0.027}_{-0.020}$  %, which results in a brightness temperature of  $3270^{+115}_{-160}$  K. This high brightness temperature, if representative for the planet's equilibrium temperature, requires a very low albedo and a high ( $f \gtrsim 0.5$ ) reradiation factor.

Combining our  $K_s$ -band measurement with the measurement of Smith et al. (2011), we can fit a simple blackbody function to the spectral energy distribution, and determine an effective temperature of  $T_{\text{eff,p}} = 3370^{+95}_{-100}$  K.

We also find that stellar pulsations of the  $\delta$  Scuti host star, WASP-33, appears to have switched modes between the two nights, which are located a month apart, and also differ from the measurements by Herrero et al. (2011). We caution, however, that this could be due to systematic effects which could also have strong periodicities.

## Acknowledgements

We are grateful to the staff of the WHT telescope for their assistance with these observations. The William Herschel Telescope is operated on the island of La Palma by the Isaac Newton Group in the Spanish Observatorio del Roque de los Muchachos of the Instituto de Astrofísica de Canarias.

## Bibliography

- Acosta-Pulido, J., Ballesteros, E., Barreto, M., et al. 2002, The Newsletter of the Isaac Newton Group of Telescopes, 6, 22
- Alonso, R., Deeg, H. J., Kabath, P., & Rabus, M. 2010, AJ, 139, 1481
- Anderson, D. R., Gillon, M., Maxted, P. F. L., et al. 2010, A&A, 513, L3+
- Breger, M. 1990, Delta Scuti Star Newsletter, 2, 13
- Caceres, C., Ivanov, V. D., Minniti, D., et al. 2011, ArXiv:1104.0041 [astro-ph.EP]
- Charbonneau, D., Allen, L. E., Megeath, S. T., et al. 2005, ApJ, 626, 523
- Collier Cameron, A., Guenther, E., Smalley, B., et al. 2010, MNRAS, 407, 507
- Cowan, N. B. & Agol, E. 2011, ApJ, 729, 54
- Croll, B., Albert, L., Lafrenière, D., Jayawardhana, R., & Fortney, J. J. 2010a, ApJ, 717, 1084
- Croll, B., Jayawardhana, R., Fortney, J. J., Lafrenière, D., & Albert, L. 2010b, ApJ, 718, 920
- Croll, B., Lafrenière, D., Albert, L., et al. 2011, AJ, 141, 30
- Deming, D. 2009, in IAU Symposium, Vol. 253, IAU Symposium, 197–207
- Fortney, J. J., Lodders, K., Marley, M. S., & Freedman, R. S. 2008, ApJ, 678, 1419
- Fressin, F., Knutson, H. A., Charbonneau, D., et al. 2010, ApJ, 711, 374
- Gelman, A. & Rubin, D. B. 1992, Statistical Science, 7, 457
- Gibson, N. P., Aigrain, S., Pollacco, D. L., et al. 2010, MNRAS, 404, L114
- Gillon, M., Demory, B., Triaud, A. H. M. J., et al. 2009, A&A, 506, 359
- Handler, G. & Shobbrook, R. R. 2002, MNRAS, 333, 251
- Hauschildt, P. H., Allard, F., Ferguson, J., Baron, E., & Alexander, D. R. 1999, ApJ, 525, 871
- Herrero, E., Morales, J. C., Ribas, I., & Naves, R. 2011, A&A, 526, L10+
- Knutson, H. A., Howard, A. W., & Isaacson, H. 2010, ApJ, 720, 1569
- López-Morales, M., Coughlin, J. L., Sing, D. K., et al. 2010, ApJ, 716, L36
- López-Morales, M. & Seager, S. 2007, ApJ, 667, L191
- Madhusudhan, N. & Seager, S. 2010, ApJ, 725, 261
- Mandel, K. & Agol, E. 2002, ApJ, 580, L171
- Rogers, J. C., Apai, D., López-Morales, M., Sing, D. K., & Burrows, A. 2009, ApJ, 707, 1707
- Sing, D. K. & López-Morales, M. 2009, A&A, 493, L31
- Smith, A. M. S., Anderson, D. R., Skillen, I., Collier Cameron, A., & Smalley, B. 2011, ArXiv:1101.2432v2 [astro-ph.EP]
- Zahnle, K., Marley, M. S., Freedman, R. S., Lodders, K., & Fortney, J. J. 2009, ApJ, 701, L20
- Zechmeister, M. & Kürster, M. 2009, A&A, 496, 577

---

## Chapter 5

---

# Optical to near-infrared transit observations of super-Earth GJ1214b: water-world or mini-Neptune?

*Context.* GJ1214b, the 6.55 Earth-mass transiting planet recently discovered by the MEarth team, has a mean density of  $\sim 35\%$  of that of the Earth. It is thought that this planet is either a mini-Neptune, consisting of a rocky core with a thick, hydrogen-rich atmosphere, or a planet with a composition dominated by water.

*Aims.* In the case of a hydrogen-rich atmosphere, molecular absorption and scattering processes may result in detectable radius variations as a function of wavelength. The aim of this paper is to measure these variations.

*Methods.* We have obtained observations of the transit of GJ1214b in the r- and I-band with the Isaac Newton Telescope (INT), in the g-, r-, i- and z-bands with the 2.2 meter MPI/ESO telescope, in the  $K_s$ -band with the Nordic Optical Telescope (NOT), and in the  $K_c$ -band with the William Herschel Telescope (WHT). By comparing the transit depth between the the different bands, which is a measure for the planet-to-star size ratio, the atmosphere is investigated.

*Results.* We do not detect clearly significant variations in the planet-to-star size ratio as function of wavelength. However, the ratio at the shortest measured wavelength, in g-band, is  $2\sigma$  larger than in the other bands. The uncertainties in the  $K_s$  and  $K_c$  bands are large, due to systematic features in the light curves.

*Conclusions.* The larger planet-to-star size ratio at the shortest wavelength could be a sign of an increase in the effective planet-size due to Rayleigh scattering, which would require GJ1214b to have a hydrogen-rich atmosphere. If true, then the atmosphere has to have both clouds, to suppress planet-size variations at red optical wavelengths, as well as a sub-solar metallicity, to suppress strong molecular features in the near- and mid-infrared. However, star spots, which are known to be present on the host-star's surface, can (partly) cancel out the expected variations in planet-to-star size ratio, because the lower surface temperature of the spots causes the effective size of the star to vary with wavelength. A spot-fraction of  $\sim 10\%$ , corresponding to an average stellar dimming of  $\sim 5\%$  in the i-band, would be able to raise the near- and mid-infrared points sufficiently with respect to the optical measurements to be inconsistent with a water-dominated atmosphere. Modulation of the spot fraction due to the stellar rotation would in such case cause the observed flux variations of GJ1214.

E.J.W. de Mooij, M. Brogi, R.J. de Kok, J. Koppenhoefer, S.V. Nefs, I.A.G. Snellen, J. Greiner, J. Hanse, R.C. Heinsbroek, C.H. Lee & P.P. van der Werf  
A&A submitted

## 5.1 Introduction

During the transit of an exoplanet, the light from its host-star filters through the planet's atmosphere, and atmospheric signatures from molecules and atoms get imprinted on the transmission spectrum. The strength of the atmospheric features is dependent on the atmospheric scale height  $H$ , which in turn depends on the temperature  $T$ , the mean molecular weight  $\mu$  and the planet's surface gravity  $g$  as  $H = \frac{kT}{\mu g}$ . For hot-Jupiters this scale height is a few hundred kilometers. For instance, the expected atmospheric scale height of HD189733b for an  $H_2$  dominated atmosphere is  $\sim 200$  km, while for HD209458b this is about 700 km. For transit observations, the observable parameter we are interested in is  $\Delta R_p/R_* \sim H/R_*$ , which is  $\sim 0.0004$  for HD189733b, and  $\sim 0.0009$  for HD209458b. Nevertheless, signatures from the atmospheres of hot-Jupiters have been detected in transmission spectra, both from atoms, including sodium (eg. Charbonneau et al. 2002; Snellen et al. 2008; Redfield et al. 2008), potassium (Sing et al. 2011a; Colon et al. 2010), hydrogen (Vidal-Madjar et al. 2003), carbon (Vidal-Madjar et al. 2004) and oxygen (Vidal-Madjar et al. 2004), as well as from molecules such as water (Tinetti et al. 2007), methane (Swain et al. 2008) and carbon monoxide (Snellen et al. 2010). In addition, a gradual increase of the planet-to-star radius ratio of HD189733b has been detected toward shorter wavelengths, which has been attributed to the scattering by haze particles (Pont et al. 2008; Sing et al. 2011b).

For cooler and smaller planets, the scale height decreases, and the  $\Delta R_p/R_*$  becomes much smaller. For the Earth the scale height is only 8.5 km, which corresponds to a change in the radius ratio of  $\sim 10^{-5}$ , which is very small. However, for the recently discovered super-Earth GJ1214b (Charbonneau et al. 2009), the scale height can be similar to that of HD189733b, due to the low ( $\sim 0.35\rho_{earth}$ ) density of the planet, if the atmosphere is dominated by  $H_2$ . Since its host-star, GJ1214, is  $\sim 4$  times smaller than the host-star of HD189733b, the change in the planet-to-star radius ratio is  $\sim 4\times$  larger at  $\Delta R_p/R_*=0.0016$ . This makes GJ1214b an ideal candidate to search for the signatures of its atmosphere, despite its small mass and radius.

Rogers & Seager (2010) presented three formation scenarios for GJ1214b that explain its low density. These scenarios also provide predictions on the composition of the planets atmosphere. If GJ1214b formed as a predominantly water-rich planet, the atmospheric scale height would be small, since the mean molecular weight of water is high. However, if GJ1214b's low density is due to out-gassing from a rocky planet, or due to it being formed as a mini-Neptune, the atmosphere is expected to consist predominantly of hydrogen and helium, with a low mean molecular weight. Atmospheric models by Miller-Ricci & Fortney (2010) showed that it is possible to get detectable signatures from an atmosphere with a large scale height, especially from molecules in near-infrared, but also from the scattering of light in the optical part of the spectrum.

Recently, the first transit transmission results for the atmosphere of GJ1214b have been presented in the literature. Bean et al. (2010) found that their spectroscopy in the z-band showed no sign for the presence of a thick, hydrogen-rich atmosphere, which argues for a water-rich atmosphere, something which is also consistent with the mid-infrared observations of Désert et al. (2011). These observations are in contrast with the results from Croll et al. (2011), who show that the transit in the  $K_s$ -band is deeper than the transit in the J-band, and therefore consistent with an atmosphere with a large scale-height and low mean-molecular weight.

In this paper we present the results for our multiband transit photometry of GJ1214b, cov-

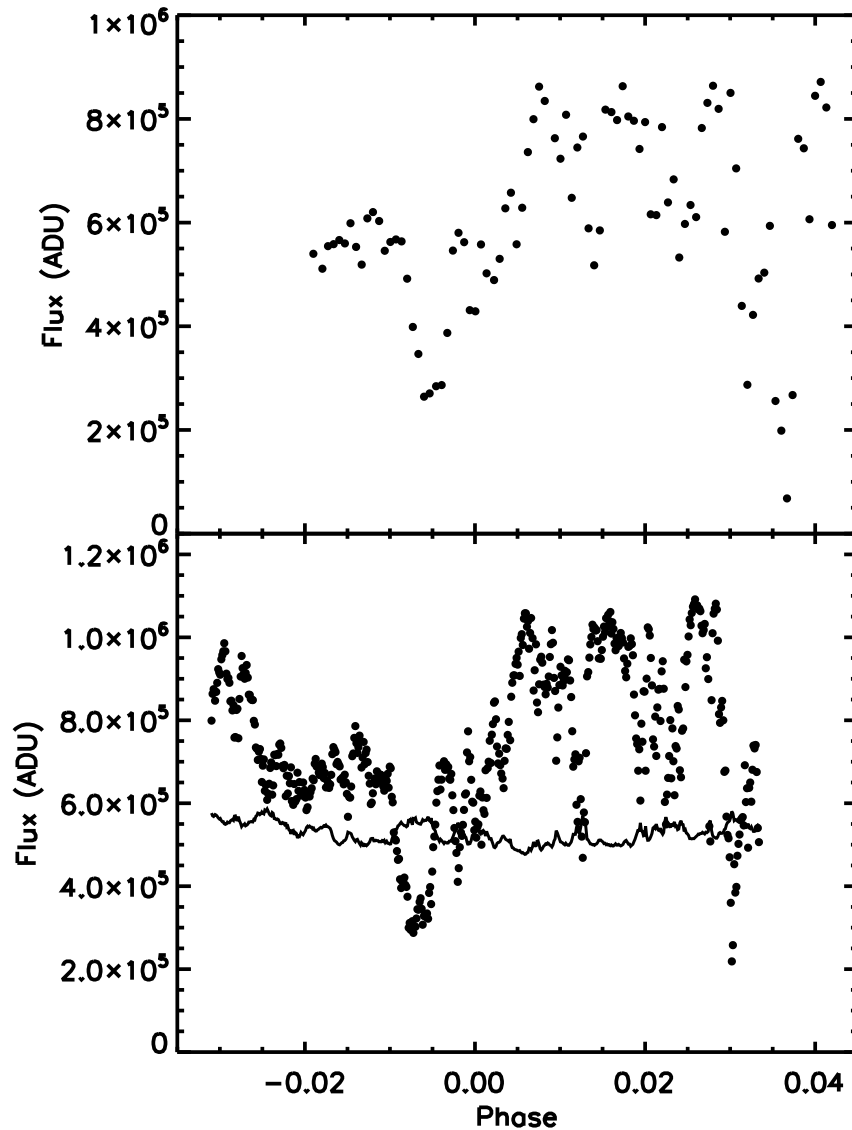


**Figure 5.1** — Raw lightcurves for the INT r-band (top panel) and the NOT  $K_s$ -band observations (bottom panel). In the bottom panel we have also overplotted the flux in the aperture due to the sky-background

ering a wavelength range from the g-band in the optical to the  $K_c$ -band in the near-infrared. In section 5.2 we present our observations, followed by the data reduction in section 5.3 and transit fitting in section 5.4. Subsequently we discuss the influence of stellar variability in section 5.5 and present and discuss the transmission spectrum of GJ1214b in section 5.6. Finally we give the conclusions in section 5.7.

## 5.2 Observations

### 5.2.1 WFC observations

A transit of GJ1214b was observed in Sloan r-band ( $\lambda_c=627$  nm) on May 26, 2010 between 2:57 UT and 5:15 UT with the Wide Field Camera (WFC) on the 2.5 meter Isaac Newton Telescope (INT). An exposure time of 60 seconds was used resulting in 89 frames with an average cycle time of 93 seconds. Only the central detector of the WFC (CCD4) was used for the analysis, with a pixel scale of  $0.33''/\text{pixel}$ , this CCD has a field of view of  $675''$  by  $1350''$ , sufficient to observe a number of reference stars of similar brightness simultaneously with the target.

The moon was almost full and the conditions were strongly non-photometric, with the transparency dropping to below 20% during several frames (see top panel of Fig. 5.1).

On July 29, 2010, a transit of GJ1214 was observed in I-band ( $\lambda_c=822$  nm) with the same instrument. The observations started at 21:23 UT and lasted for just over 3 hours. An exposure time of 50 seconds was used, resulting in a total of 142 frames with an average cycle time of 81 seconds. In this case the night was photometric.

Since GJ1214b is about 5.5 times brighter in I-band than in r-band, we significantly defocused the telescope in the I-band in order to keep the peak count-levels in the linear regime of the detector. This has the added benefit that the light is spread over more pixels, reducing the impact of flat-fielding errors.

### 5.2.2 GROND griz-band observations

On the night of July 3, 2010, we obtained simultaneous observations of GJ1214b in the g ( $\lambda_c=459$  nm), r ( $\lambda_c=622$  nm), i ( $\lambda_c=764$  nm), and z-band ( $\lambda_c=899$  nm) with the GROND instrument (Greiner et al. 2008) on the 2.2 meter MPI/ESO telescope at La Silla in Chile. The field of view in each of the wavelength channels is  $5.4'$  by  $5.4'$ , which is sufficient to observe both GJ1214 and a set of reference stars simultaneously. The observations started at 00:16 UT and lasted until 04:06 UT. During this time we obtained 280 frames in each of the four optical bands. The exposure time was varied from 20 to 30 seconds to avoid saturation of the CCDs. The average cycle time was 50 seconds.

### 5.2.3 NOTCam $K_s$ -band observations

We obtained a  $K_s$  band transit observations with the NOTCam instrument on the Nordic Optical Telescope (NOT) simultaneously with our INT r-band observations on May 26, 2010. The observations were carried out in service mode, and the wide field imaging optics and a  $K_s$ -band filter ( $\lambda_c=2.15 \mu\text{m}$ ) were used. The pixelscale of this setup is  $0.234''/\text{pixel}$ , resulting in a field of view of the detector of 4 by 4 arcminutes. This field of view is sufficient to allow simultaneous observations of one reference star of similar brightness to GJ1214 as well as a reference star that is  $4\times$  fainter than GJ1214. The field of view of the detector was rotated to make sure that bad regions on the detector were avoided for all three stars. Since the NOT is located on the same mountain as the INT, these observations suffer from the same non-photometric conditions, with the transparency dropping to 25% for parts of the lightcurve (see Fig. 5.1). This strongly

affects the observations, since the sky background dominates over the object flux for the larger apertures, especially during times of low transparency.

Since GJ1214 is bright at near-infrared wavelengths, we defocused the telescope in order to allow for the relatively long integration time and reducing the sensitivity to flat-fielding errors, although this also increases the impact of the sky background.

The exposure time was set to 4 seconds, to allow for relatively efficient observations, with the large overheads induced by the NOTCam system. The average cycle time was 16 seconds, allowing us to capture 518 frames in 2 hours and 25 minutes of observations.

In order to increase the stability of the system for the observations, and to decrease the telescope overheads, we observed in staring mode, with guiding, keeping the centroid of the star constant to within 4 pixels during the observations. Since this observation strategy does not allow us to subtract the background from the images, we obtained a set of dithered observations after our transit observation, from which we constructed a background map.

#### 5.2.4 LIRIS $K_c$ -band observations

The  $K_c$ -band ( $\lambda_c=2.27\mu\text{m}$ ) observations were obtained with the Long-slit Intermediate Resolution Infrared Spectrograph (LIRIS; Acosta-Pulido et al. 2002) on the William Herschel Telescope (WHT) on the night of August 17, 2010. The pixel-scale of the LIRIS detector is  $0.25''/\text{pixel}$ , resulting in a field of view of the detector of 4.2 by 4.2 arcminutes. The same reference stars as for the NOTCam observations were used.

A similar observing strategy as that of the NOTCam observations was followed, defocusing the telescope and performing the observations in staring mode. An exposure time of 10 seconds was used, resulting in an average cycle time of 12.5 seconds. We obtained 1010 frames during the 3 hours and 26 minutes of observations, of which 300 were taken during the transit. From these we discarded the first 40 frames, 28 of which were taken with the stars on a different position on the detector, and the others because they were taken with a different defocus of the telescope. The frames were obtained in sequences of 100, from which the first 3 frames clearly suffered from the reset anomaly. These frames were also excluded from further analysis (27 frames in total). As for the NOTCam observations, we observed a field offset from GJ1214 in order to construct a background map.

### 5.3 Data reduction

#### 5.3.1 Optical data

A standard data reduction was performed for the WFC-INT data: after bias subtraction the images were flatfielded with a twilight flat. In addition a fringemap was used to correct the WFC I-band data for strong fringing.

Subsequently aperture photometry was performed on GJ1214 and a set of reference stars (24 for the r-band and 14 for the I-band), using apertures of 10 and 19 pixels for the r- and I-band respectively. The background was measured in annuli centered on the stars, using an

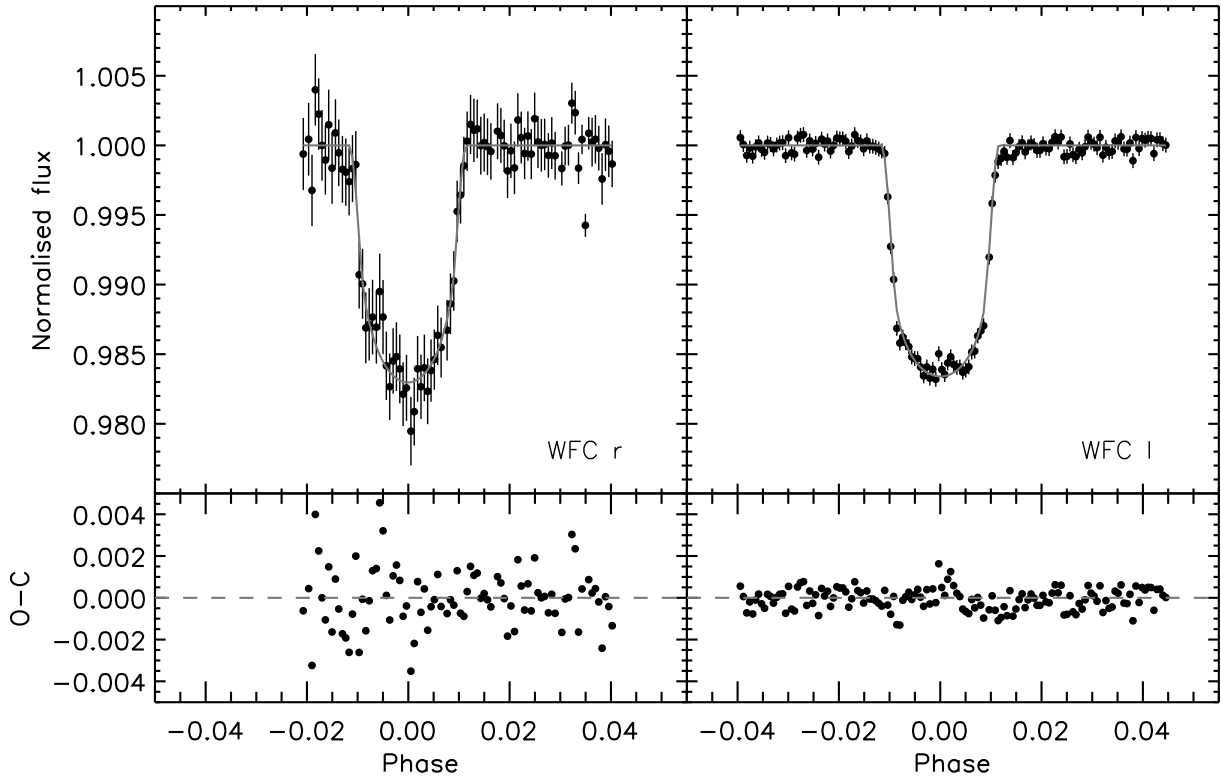


**Figure 5.2** — Light curves for our WFC r- and I-band observations. The best fit transit models are overplotted.

inner radius of 25 and an outer radius of 50 pixels for the WFC r-band and 35 and 70 pixels for the I-band.

Since the weather conditions during the INT r-band observations were strongly non-photometric, extinction gradients could be present in the photometry of the stars across the detector. Rather than directly combining lightcurves of all stars to obtain a reference lightcurve, we fitted the normalised photometry of the reference stars in each frame with linear function in the  $(x,y)$ -position and background flux. We then calculated the value of the best fit function for GJ1214, to remove the extinction effects of the atmosphere. Subsequently we fitted an airmass curve to the corrected lightcurve of GJ1214 to adjust for second order colour effects. The resultant lightcurve is shown in the left panel of Fig. 5.2. The out-of-transit noise-level is  $1.6 \cdot 10^{-3}$  per data point, which is 1.3 times larger than expected from Poisson and read-noise statistics.

Since the WFC I-band data were taken under photometric conditions, we simply combined the photometry of all the reference stars for the reference lightcurve. Subsequently we corrected for the airmass as for the r-band data. The resultant lightcurve is shown in the right panel of Fig. 5.2. The out-of-transit noise-level is  $4.5 \cdot 10^{-4}$ , while the expected noise level from Poisson and read-noise statistics is  $3 \cdot 10^{-4}$ . However, this estimate does not take scintillation noise into account, which is difficult to quantify, and could easily dominate the noise at this level.

The GROND data, taken in the g-, r-, i- and z-bands simultaneously, were reduced in a similar way as the INT data. An aperture of 18 pixels was used for the aperture photometry, while the background was determined in an annulus around the star with an inner radius of 20 pixels and an outer radius of 30 pixels for all bands.



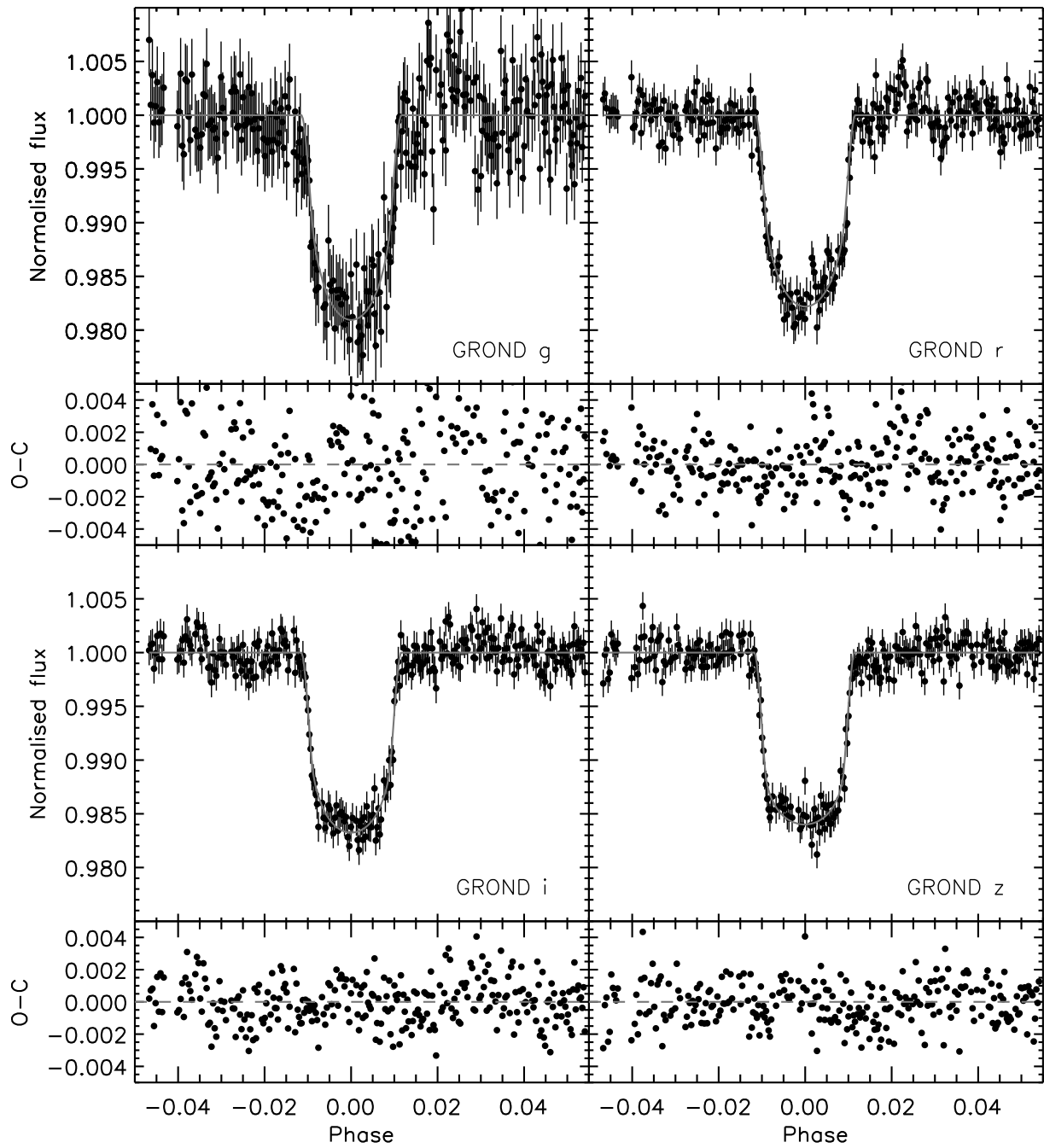


**Figure 5.3** — The lightcurves for our GROND observations with the best fit models overplotted.

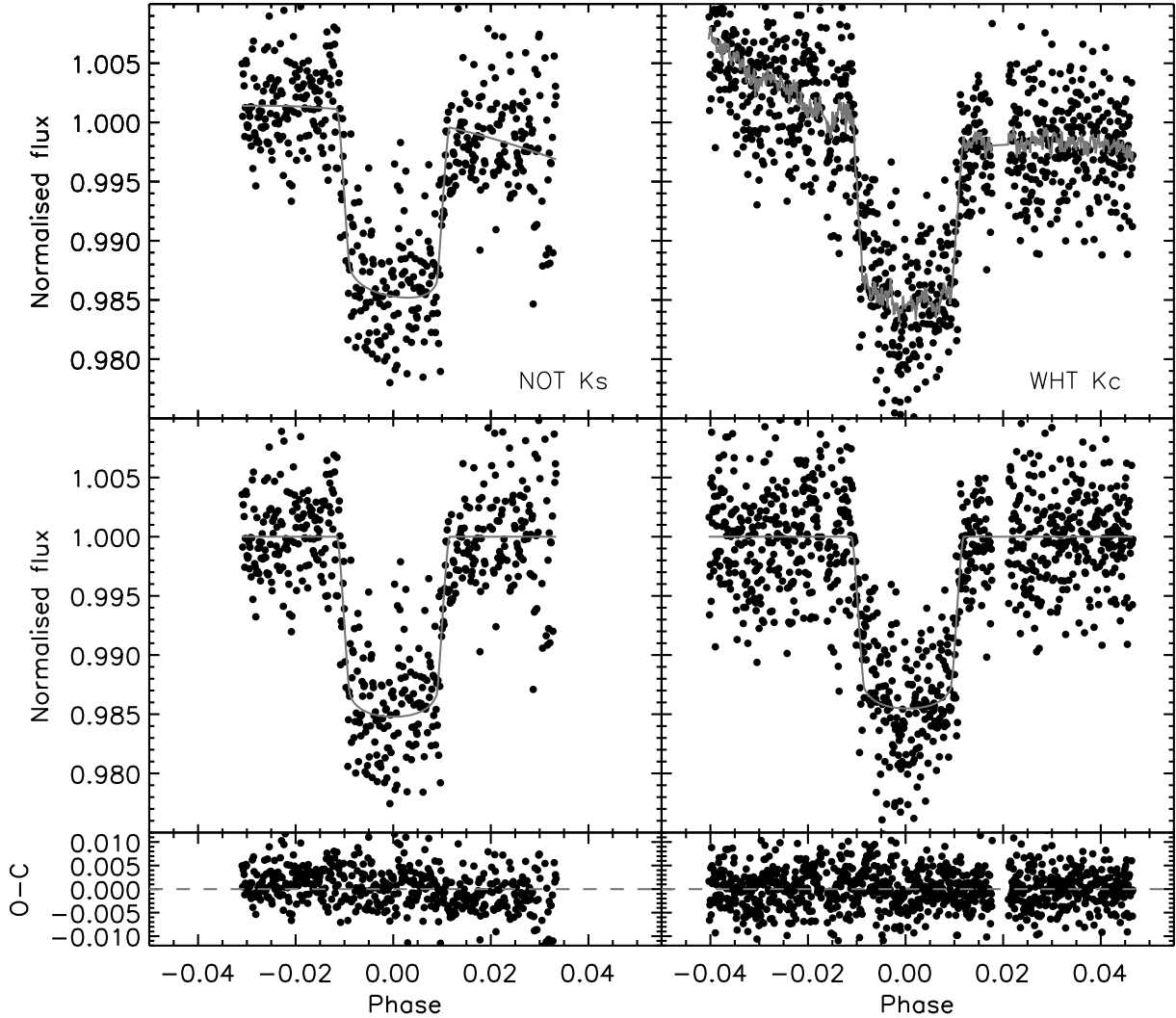


**Figure 5.4** — Light curves for our NOTCam  $K_s$ -band and LIRIS  $K_c$ -band observations. Top panels: Raw, normalised lightcurves with best fit model for the transit and systematic effects overplotted. Middle panels: Lightcurves corrected for systematic effects, with the best fit transit model overplotted. Bottom panel: residuals after subtracting the best fit models.

Subsequently, a linear base-line was fitted to the lightcurves of each band resulting in an out-of-transit RMS of the lightcurves of  $3.3 \cdot 10^{-3}$ ,  $1.6 \cdot 10^{-3}$ ,  $1.4 \cdot 10^{-3}$  and  $1.3 \cdot 10^{-3}$ , for the g-, r-, i- and z-bands respectively. These noise-levels are significantly higher than expected from Poisson and read-noise statistics, possibly due to the fact that these in-focus observations are much more sensitive to flatfielding inaccuracies.

### 5.3.2 Near-infrared data

As a first step in the NOTCam  $K_s$ -band data reduction a non-linearity correction was made to all frames on a pixel-by-pixel basis, using a non-linearity measurement from the NOTCam cal-

ibration archive<sup>1</sup>. The science frames were subsequently flatfielded using a twilight flat. Those frames obtained for sky-subtraction purposes were flat-fielded, and combined after removing the outliers for each pixel, which removes any stars present in the individual images. The result was subsequently subtracted from the science images, removing most of the structure in the background.

In the next step, aperture photometry was performed on GJ1214 and the reference stars, using an aperture of 10 pixels for the NOTCam dataset. The residual background was determined by averaging the background signal in an annulus centered on the stars with an inner radius of 30, and an outer radius of 50 pixels. Individual pixels in the annulus were clipped at  $5\text{-}\sigma$  from the mean to prevent outliers from affecting the background measurements.

The WHT-LIRIS  $K_c$ -band data were reduced in a similar way, but we constructed our own non-linearity curve from a sequence of dome-flats at different exposure times. After the sky-subtraction, aperture photometry was performed with a 25 pixel radius, using an annulus from 30 to 50 pixels to determine the residual background, clipping the outliers in the same way as for the NOTCam data.

The NOTCam  $K_s$ - and LIRIS  $K_c$ -band lightcurves normalised by those from the reference stars are shown in the top-panels of Fig. 5.4. Further corrections for systematic effects are done simultaneously with the transit fitting and are discussed in Sect. 5.4.2.

## 5.4 Transit fitting

### 5.4.1 Optical transits

Since our goal is to measure the effective radius of the planet as a function of wavelength and not to determine the other transit parameters, we fit the transit at each band independently, keeping the impact parameter and semi-major axis fixed to the values used by Bean et al. (2010). This has the added benefit that we can compare our results directly to previous literature values. To model the transit curve we use the formalism of Mandel & Agol (2002) with non-linear limb-darkening coefficients as calculated by Claret (2000) for the INT I-band observations and by Claret (2004) for the observations at the other wavelengths. We performed a Markov-Chain Monte Carlo (MCMC) analysis to find the planet-to-star radius ratio and the time of mid-transit, creating 5 chains with a length of 200,000 points for each band. From each of the chains the first 20,000 points were trimmed to ensure that the initial conditions did not influence the results. After checking that the chains were well mixed using the Gelman & Rubin (1992) test, we merged them. The best fit models are overplotted on the lightcurves in Figs. 5.2 and 5.3.

To assess the impact of red-noise on uncertainties of the fitted parameters, we used the residual permutation method, which uses the data itself to assess the uncertainties on the measured parameters due to correlated noise. The best fit model is added to the residuals from the MCMC fit, after the residuals were shifted by  $N$  points. The points are wrapped around when performing the shift. The new lightcurve is then refitted. For the fitting we used the IDL MPFIT package<sup>2</sup> (Markwardt 2009). To assess the uncertainties on the parameters we use the range between 16% and 84% of the distribution of the parameters for the  $\pm 1\text{-}\sigma$  uncertainty interval.

---

<sup>1</sup><http://www.not.iac.es/instruments/notcam/calibration.html>

<sup>2</sup><http://purl.com/net/mpfit>

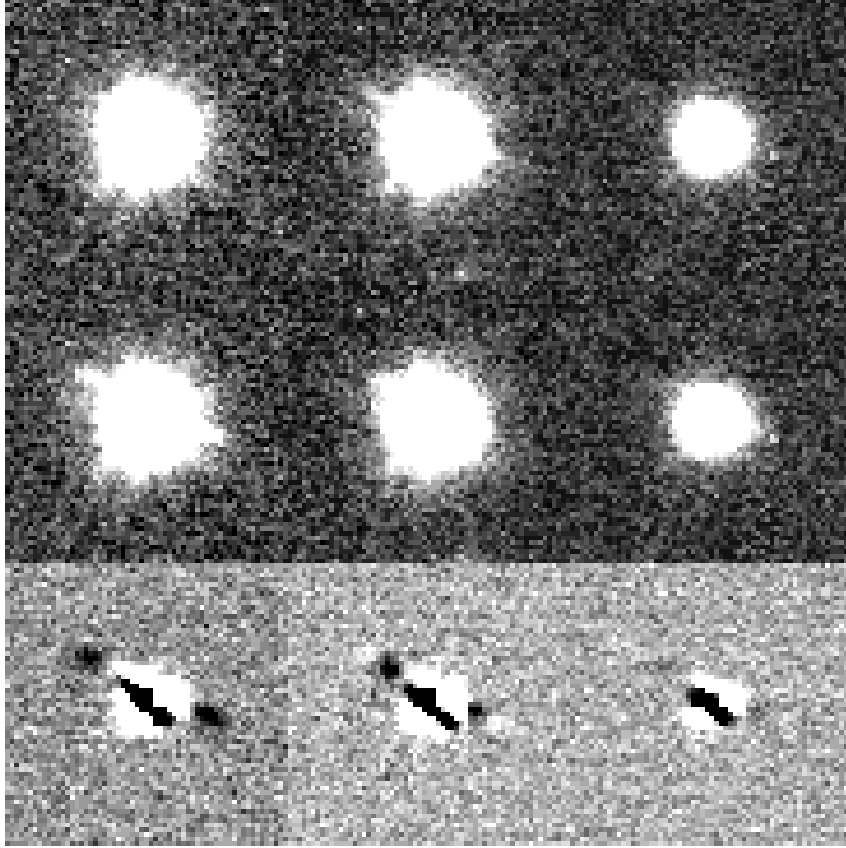


**Figure 5.5** — Images of the PSFs for our LIRIS  $K_c$ -band observations taken at two different times. The left column is for GJ1214, while the middle and right columns are for the two reference stars. The top panels show the average PSF in a sequence of 31 frames just before an anomalous feature is visible in the lightcurve, while the middle row shows the average PSF during the anomalous feature. The difference between the PSFs is shown in the bottom row.

In the INT r- and I-band observations, the uncertainty estimates from the residual permutation method are lower than those obtained from the MCMC analysis, this is probably due to the low number of frames that were obtained. In this case we have adopted the uncertainties from the MCMC analysis rather than those from the residual permutation analysis.

The fitted radius ratios for all bands (see also Table 5.2), are  $0.1143 \pm 0.0018$  and  $0.1162 \pm 0.0005$ , for our INT r and I-band measurements, and  $0.1198^{+0.0026}_{-0.0013}$ ,  $0.1168 \pm 0.0010$ ,  $0.1162 \pm 0.0013$  and  $0.1165 \pm 0.0013$  for our GROND g-, r-, i- and z-band observations respectively. The times of mid-transit are given in Table 5.1.

### 5.4.2 Near-infrared transits

Firstly, outliers were removed from the  $K_s$ -band lightcurve by excluding all points more than 1.2% away from a median smoothed lightcurve. In this way 25 points were removed. A clear residual trend in the out-of-transit baseline is visible in the lightcurve (Fig. 5.4), but we find no significant correlations with the position on the detector or airmass, which we often see in other near-infrared measurements (e.g. Chapters 2 and 3). We therefore fitted the lightcurve

with a second order polynomial simultaneously with the transit parameters. As for the optical lightcurves, we only fitted for the time of mid-transit and the planet-to-star size ratio, keeping the impact parameter and semi-major axis fixed to the values used by Bean et al. (2010). The fits were again performed using an MCMC analysis, as for the optical data, using 5 chains of 200,000 steps, trimming away the first 20,000 points and checking that they were well mixed (Gelman & Rubin 1992). Non-linear limb-darkening parameters from Claret (2000) were used. The best fit model is overplotted in the top-left panel of Fig. 5.4. The lightcurve with the corrected baseline is shown in the left middle panel, and the residuals in the bottom left panel of the same figure.

Just as for the optical data, the impact of correlated noise is investigated using the residual permutation method. The estimates for the uncertainties given by the residual permutation method are almost identical to those we obtain from our MCMC analysis, which indicates that, apart from the trend in the baseline, the systematic effects are small compared to the random noise. We measure a radius ratio in the  $K_s$ -band of  $0.1189 \pm 0.0015$ .

The LIRIS  $K_c$ -band lightcurves were fitted in a similar way to the NOTCam  $K_s$ -band data. First, 13 outlier points were removed from the lightcurve. In addition to the systematic trends seen in the baseline, which again do not correlate with airmass or with position on the detector, we found a correlation with the fraction of the total flux of the star contained in the brightest 11 pixels, which we take to be a proxy for the seeing (note that due to the strong defocus we cannot measure the seeing directly). We therefore fitted the relevant transit parameters simultaneously with a second order polynomial and this seeing proxy. We used a MCMC analysis similar to that used for the  $K_s$ -band lightcurve. In Fig. 5.4 the best fit model is overplotted in the top right panel, and the lightcurve corrected for systematic effects is shown in the middle right panel. The residuals from the best fit model are shown in the bottom right panel of the same figure.

The estimates for the uncertainties given by the residual permutation method are  $\sim 50\%$  higher than those that were obtained from the MCMC analysis, and there is also an asymmetry between the upper and lower uncertainties.

As can be seen in the bottom right panel of Fig. 5.4, a significant feature is visible in the corrected  $K_c$ -band lightcurve between phase  $-0.012$  and phase  $-0.006$ . Although this feature could be due to starspots, at the same moment a sudden increase in the difference in background occurs between the target and the reference star. At the moment of this 'bump' we also see a change in the shape of the PSF at lower intensities across the field of view of the detector (especially around the diffraction spikes caused by the support of the secondary mirror, see Fig. 5.5). It seems that instrument-related effects influence the measurements at this point. To check the influence of this feature on the fit to the lightcurve, we excluded it and refitted the time-series. While for the lightcurve as a whole we find a radius ratio of  $0.1162^{+0.0016}_{-0.0021}$ , we find a radius-ratio of  $0.1187 \pm 0.0018$  ( $\sim 1.5\sigma$  deeper) when this feature is excluded from the fit. Since we do not want to bias our results, we use the radius-ratio obtained from fitting the entire  $K_c$ -band lightcurve for the rest of the paper. The extra uncertainty is accounted for by increasing the error on the radius ratio by 50%.

## 5.5 Stellar variability

Charbonneau et al. (2009) found that the star GJ1214 is variable at the level of 1% in the MEarth

**Table 5.1** — Parameters used for the transit fitting of GJ1214 and the measured times of mid-transit. References: (1) Bean et al. (2010); (2) Charbonneau et al. (2009); (3) this work

Parameter		Value	Reference
$a/R_*$		14.9749	(1)
$b=a/R_*\cos(i)$		0.27729	(1)
P	(days)	1.580408346	(1)
$T_{star}$	(K)	3030	(2)
$T_C$ -2,400,000 (HJD)	(INT r)	$55342.66081\pm 0.00029$	(3)
...	(NOT $K_s$ )	$55342.66057\pm 0.00023$	(3)
...	(GROND g)	$55380.59049\pm 0.00040$	(3)
...	(GROND r)	$55380.59045\pm 0.00019$	(3)
...	(GROND i)	$55380.59044\pm 0.00022$	(3)
...	(GROND z)	$55380.59013\pm 0.00017$	(3)
...	(INT I)	$55407.45754\pm 0.00007$	(3)
...	(WHT $K_c$ )	$55426.42274\pm 0.00032$	(3)

**Table 5.2** — Radius ratios as determined from our observations in different filters (column 4), the correction that is applied to the radius ratios due to stellar variability (column 5), as well as the correction for a background of starspots that cover 10% of the stellar surface (column 6) (the difference in i-band is set to 0). The instruments, filters and central wavelengths are indicated in columns 1 through 3.

Instrument	Band	$\lambda_c$	$\left(\frac{R_p}{R_*}\right)_{measured}$	$\Delta\left(\frac{R_p}{R_*}\right)_{corr}$	$\Delta\left(\frac{R_p}{R_*}\right)_{10\%spots}$
		( $\mu\text{m}$ )			
GROND	g	0.46	$0.1198^{+0.0026}_{-0.0013}$	-	-0.0007
GROND	r	0.62	$0.1168\pm 0.0010$	-	-0.0005
WFC	r	0.63	$0.1143\pm 0.0018$	0.0011	-0.0006
GROND	i	0.76	$0.1162\pm 0.0013$	-	0.0000
WFC	I	0.82	$0.1162\pm 0.0005$	-	+0.0005
GROND	z	0.90	$0.1165\pm 0.0013$	-	+0.0009
NOTCam	$K_s$	2.15	$0.1189\pm 0.0015$	0.0003	+0.0023
LIRIS	$K_c$	2.27	$0.1162\pm 0.0030$	-	+0.0021

bandpass, with an apparent period of  $\sim 80$  days, attributed to the rotation-modulated variations in the star-spot levels. Recently Berta et al. (2011) presented a stellar variability analysis covering several years of data, finding a period of  $52.3 \pm 5.3$  days. This star-spot induced variability can have a major impact on transit photometry taken at different epochs and/or at different wavelengths (e.g. Carter et al. 2011; Sing et al. 2011b). Since our data are taken over the course of 3.5 months, and our aim is to measure differences in the transit-depth as a function of wavelength, both the temporal and spectral effects from starspots are present and need to be taken into account.

If a star-spot is present on the stellar surface during transit, firstly the planet could transit the spot. Because the star-spots have a lower surface brightness than the unspotted stellar surface, a spot that is occulted by the planet would make the transit less deep and bias the planet-to-star radius ratio to lower values. In the case the planet does not cross the star spot, the transit appears deeper, since the average surface brightness along the path of the planet is higher than that of the spotted surface, leading to a decrease of the effective radius of the star. Unocculted spots will therefore bias the planet-to-star size ratio to higher values. In addition, since the star spots have a lower effective temperature than the stellar surface, and are therefore relatively red, these effects will be stronger in the blue part of the optical spectrum than in the near-infrared. An expression for the bias due to unocculted starspots can be found in Sing et al. (2011b).

### 5.5.1 Correcting for the stellar variability

Changes in the spot fraction can be monitored by measuring the stellar brightness as a function of time, which can subsequently be used to link the observations taken at different epochs. Note that this does not take into account the base-level of spots, which is unknown but can still significantly influence the measured planet-to-star radius ratio as a function of wavelength. This is discussed in Sect. 5.6.4.

To link our INT I-band observations to our INT r-band observations, we obtained a set of r-band out-of-transit frames on July 29, 2010, in order to measure the change in stellar brightness between the two nights. These r-band frames were reduced in the same way as the transit observations, and aperture photometry was performed on the same set of stars as for the observations on May 26. We find that between May 26 and July 29 the star has decreased its brightness by  $\Delta F=2\%$ . We therefore correct our INT r-band and NOTCam  $K_s$ -band points to match the stellar brightness of the INT I-band observations. We use the expression for the effects of starspots on the planet-to-star radius ratio from Sing et al. (2011b), where we use the NextGen models (Hauschildt et al. 1999) for flux of both the star and the spots. We assume a spot temperature of  $T_{spot}=2800$  K, which is 200 K cooler than the effective temperature of the star. We find a correction  $\Delta R_p/R_* = 0.0011$  in the r-band and  $\Delta R_p/R_* = 0.0003$  in the  $K_s$ -band.

We linked the stellar brightness during the night of the GROND observations to that during the INT r-band observations using the data from Berta et al. (2011). Subsequently, this was linked to our INT I-band observations using the offset found above. These two steps cancel each other out within the uncertainties and therefore no correction was performed on the GROND measurements. We also did not correct the  $K_c$ -band observation, since we have no flux measurements of the stellar brightness in the r-band on that night. However, the correction is expected to be small ( $\Delta R_p/R_* \lesssim 0.0003$ ), and will therefore not significantly influence the measured transmission spectrum. The corrections for the radius ratios are given in Table 5.2.

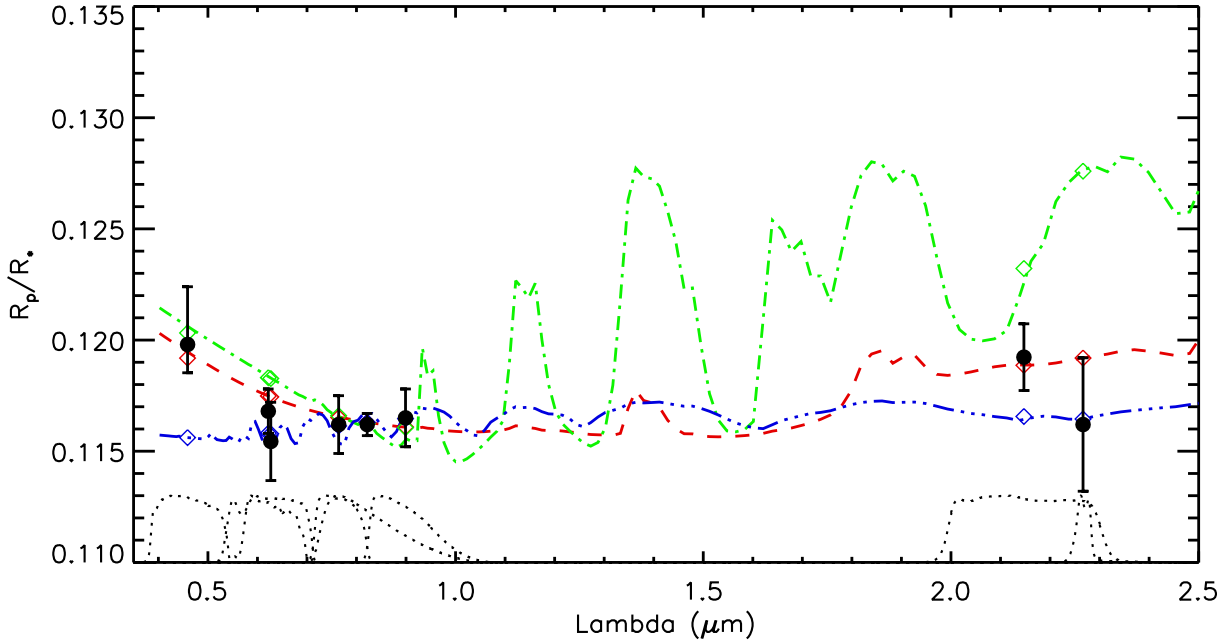


**Figure 5.6** — Transmission spectrum of GJ1214b from our data. Overplotted are models for the atmosphere of GJ1214b. The dashed-dotted line is a hydrogen rich atmosphere with a solar metallicity, the dashed curve is for an atmosphere that is hydrogen rich with a sub-solar metallicity and a cloud layer at 0.5 bar, the dashed-triple dotted line is for an atmosphere that is dominated by water. The dotted curves at the bottom of the plot show the various transmission curves of the filters used for our measurements.

## 5.6 Discussion

### 5.6.1 The transmission spectrum of GJ1214b

Using the measured planet-to-star radius ratios in all of our bands, corrected for stellar variability, we can construct a transmission spectrum for GJ1214b, which is shown in Fig. 5.6. All data points are consistent with a constant planet-to-star size ratio within  $1\sigma$ , except for the g-band point at  $0.46\mu\text{m}$ , which deviates by  $\sim 2\sigma$ .

### 5.6.2 Atmospheric models

To investigate what constraints our observations can place on the atmosphere of GJ1214b, we compare our results with theoretical models of the planet’s atmosphere. The models include Rayleigh scattering as well as molecular absorption features and collision-induced absorption from  $\text{H}_2\text{-H}_2$  (Borysow 2002). For the transmission spectrum we calculated the light passing through layers of atmosphere between  $1 \cdot 10^{-6}$  and 5 bar. At higher pressures we consider the atmosphere to be fully opaque. At each point we assume that the atmosphere can be described by an average profile in hydrostatic equilibrium. For the temperature-pressure profile we use one that is similar to that used by Miller-Ricci & Fortney (2010). Our models include absorption by water, for which the opacity data from the HITEMP database (Rothman et al. 2010) were used. In addition we also include methane, for which the data from HITRAN 2008 (Rothman et al. 2009) were used. Water and methane are expected to be the main absorbing gases in



the atmosphere. A line-by-line code was used to calculate the opacities for the different gases, assuming a homogeneous mixing of all the different species present in the atmosphere.

We have chosen to generate three models to make a qualitative study of the atmosphere of GJ1214b, and we have overplotted these models on the observed transmission spectrum shown in Fig. 5.6. The models were matched to the mean of the measured radius ratios between  $0.7 \mu\text{m}$  and  $1 \mu\text{m}$ . The first model, the dash-dotted line in Fig. 5.6, is for a (geometrically) thick atmosphere with a solar composition and no cloud layers. The concentrations of water and methane are  $3 \cdot 10^{-4}$ . The dominant hydrogen gives rise to a high atmospheric scale height, as can be seen by the strong molecular features in the near infrared. Fig. 5.6 indicates that a solar metallicity atmosphere gives features that are too strong compared to our measurements, resulting in a  $\chi^2$  of 26.7. The second model, the dashed line in the figure, is for an atmosphere with a sub-solar metallicity, and includes a grey cloud layer at a pressure of 0.5 bar. The concentrations of water and methane are  $5.6 \cdot 10^{-6}$  and  $5 \cdot 10^{-7}$  respectively. This model is consistent with our measurements ( $\chi^2=3.2$ ). The third model, the dashed-triple dotted line in the figure is for a water dominated atmosphere. This model has its molecular features significantly suppressed due to the decreased scale height. This model is also consistent with all our observations, but with a higher  $\chi^2$  of 15.1 compared to that of the second model. This is mainly due to the g-band measurement. The latter two models are chosen such that they can reproduce the relatively flat transmission profile seen in the red part of the optical spectrum.

The data can be well fitted with a model with a sub-solar metallicity and a cloud layer. The major disagreement between our data and the model for a water-dominated atmosphere comes from the GROND g-band measurements, which could be due to Rayleigh scattering, and to a lesser extent from the NOTCam  $K_s$ -band observations. It is therefore important to obtain further observations to confirm these measurements.

### 5.6.3 Comparison with previous measurements

During the past year there have been many transit measurements of GJ1214b at different wavelengths. Bean et al. (2010) measured the transit-depth in 11 wavelength bins from 790 nm to 1000 nm. Our radius ratios obtained in the same wavelength range are consistent with their measurements. Bean et al. (2010) cannot explain their observations with a thick, hydrogen-rich atmosphere, and therefore favour models for a water-dominated atmosphere of GJ1214b. However, they cannot rule out clouds as an explanation for their relatively featureless transmission spectrum. This is also seen when comparing their data with our models, the  $\chi^2$  for the water model is 9.1, while that for the model with a sub-solar composition and a cloud layer is 7.8.

Croll et al. (2011) have presented measurements of the transit-depths in the J- and  $K_s$ -bands, as well as in a band centered on a methane feature at  $1.69 \mu\text{m}$ . Their measurements in the J- and  $K_s$ -band provide evidence for an increase in the planetary radius at  $2.15 \mu\text{m}$  compared to that at  $1.15 \mu\text{m}$ . This increase is consistent with the presence of a thick, hydrogen-rich atmosphere. The additional measurement of the transit-depth at  $1.69 \mu\text{m}$ , which probes a methane feature in the H-band, is lower than that observed in the J-band. This point however has a large uncertainty, and is therefore still consistent with an atmosphere with a low mean-molecular weight, but only if the methane abundance is low. Comparison of these data with our models shows a significant increase in the  $\chi^2$  between the sub-solar metallicity model and the water model of  $\Delta\chi^2=20.1$ , as advocated by Croll et al. (2011). The large depth in the  $K_s$ -band for the sub-solar metallicity

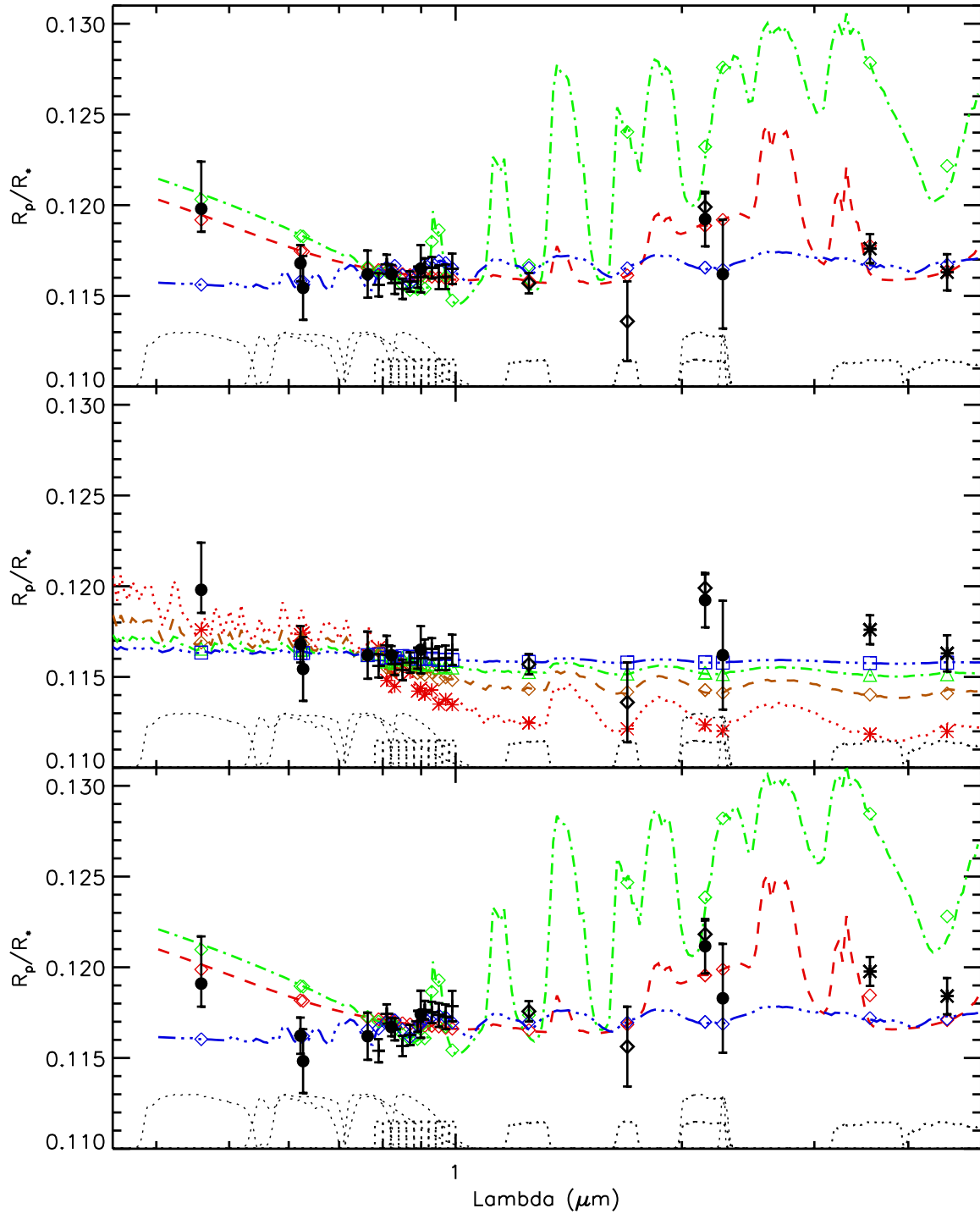


**Figure 5.7** — Top panel: Transmission spectrum of GJ1214b. Overplotted are the atmospheric models for GJ1214, using the same linestyles as in Fig. 5.6 for the atmospheric models. Our data are plotted as filled circles, the VLT data from Bean et al. (2010) as crosses, the *Spitzer* data from Désert et al. (2011) as stars, and the data from Croll et al. (2011) as diamonds. Middle panel: The same data points as in the top-panel but now with different models overplotted showing the change in radius ratio due to different amounts for the base levels of stellar spots in the GROND i-band. The dotted, dashed, dash-dotted and the dashed-triple dotted lines are for 10%, 5%, 2.5% and 1% contribution from stellar spots in the i-band. Bottom panel: The observed transmission spectrum, but now corrected for a spot-dimming in i-band due to spots of 5% (The dashed curve in the middle panel), which corresponds to a spot coverage of 10% of the stellar surface. The i-band radius ratio was kept at the same level as in the other panels.

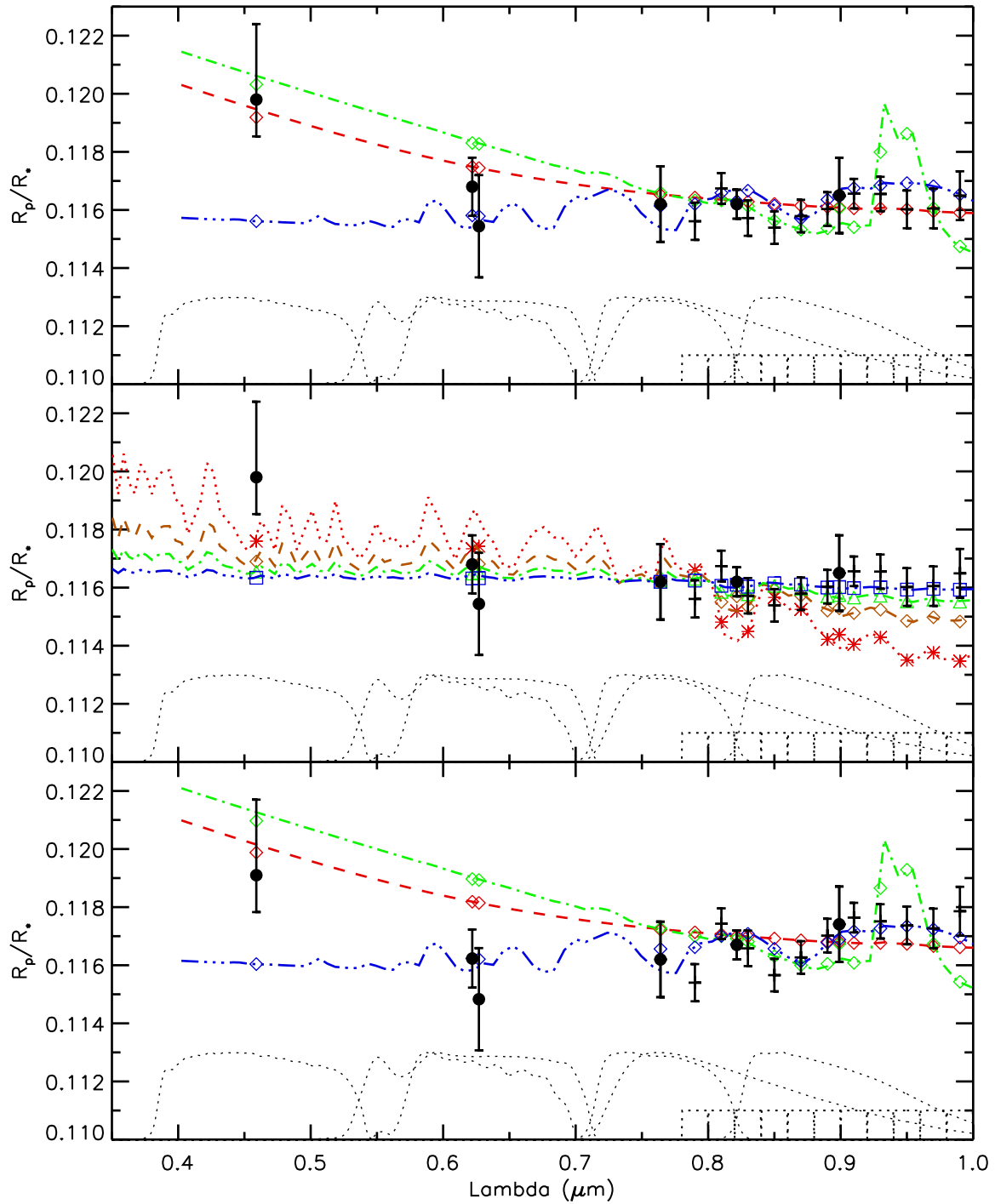


**Figure 5.8** — Same as Fig. 5.7 but now only showing the optical part of the transmission spectrum.

model is due to H<sub>2</sub>-H<sub>2</sub> CIA and not due to methane.

In contrast, using the IRAC camera on the *Spitzer* Space Telescope, Désert et al. (2011) find radius ratios in the IRAC bands at 3.6 and 4.5  $\mu\text{m}$  that are consistent with the observations of Bean et al. (2010), showing a flat transmission spectrum extending into the mid-infrared. The observations by Désert et al. (2011) therefore reject a cloud-free methane rich atmosphere because it would require a significantly larger radius at 3.6  $\mu\text{m}$  than is observed. Within the  $1\sigma$  errorbars, the observations of Désert et al. (2011) are consistent with both the sub-solar metallicity model with a large scale-height and with the model for a water-dominated atmosphere.

In addition to our own g-band measurement, observations by Carter et al. (2011) in the r- and z-band show evidence for an increase in the radius-ratio of the planet when going from the z-band to the r-band at the  $1\sigma$  level. However, they also caution that stellar spots are important when comparing observations at different dates and wavelengths. The measured increase of the planet-to-star radius ratio is  $0.00184 \pm 0.00166$ , which is consistent with Rayleigh scattering, where the expected difference is  $\sim 0.0015$ . It is, however, difficult to directly compare these measurements with our measurements, since Carter et al. (2011) used a different impact parameter and semi-major axis.

In the top panel of Figs. 5.7 and 5.8 we show all the currently available measurements of the transmission spectrum of GJ1214b that were obtained using the same impact parameter and scaled semi-major axis. We caution, however, that when making a direct comparison between literature values and our observations one has to be careful, since these were taken at different epochs, and therefore at different levels of stellar variability.

Ignoring these subtle effects, the available data favour the model for a hydrogen-rich, low metallicity atmosphere with a cloud layer at 0.5 bar ( $\chi^2=14.3$ ) over a water dominated atmosphere ( $\chi^2=48.7$ ). This is mainly due to our g-band measurements and the measurements in the K<sub>s</sub>-band presented in this paper and in Croll et al. (2011). The *Spitzer* measurements from Désert et al. (2011) are consistent with both models.

#### 5.6.4 The impact of unocculted starspots

As discussed in Section 5.5, unocculted spots can also produce a wavelength dependent signal in the transmission spectrum, by altering the effective radius of the star. Since only the variation in the starspots is traced by the variability measurements, and not the total level of spots, we have no constraints on the base level of spots present on the stellar surface. There is a priori no reason to assume that the only spots present on the stellar surface are those responsible for the variability. This would result in flat regions in the lightcurve when no spots are visible on the stellar hemisphere pointed toward Earth, which is not seen in the lightcurve by Berta et al. (2011).

From this variability curve we know that GJ1214 varies in brightness at the  $\sim 1\%$  level in the MEarth bandpass. This corresponds to a variation in the spot-fraction of  $\sim 2.5\%$ , assuming a spot temperature of 2800K. We might expect that this variability is the result of a distribution of many small spots on the stellar surface. This is supported by the fact that for 2 out of the 16 transits observed by Carter et al. (2011) the planet crosses over a small star spot. Since these spots are possibly distributed in a random pattern in longitude on the stellar surface, we argue that the fraction of the star that is covered in spots is significantly higher than the 2.5% necessary to explain the variability.

To investigate at what level the observed transmission spectrum can be influenced by a base level of unocculted spots, we calculated the wavelength dependent bias in the radius ratio for several assumed base levels, which is overplotted on the observed transmission spectrum in the middle panels of Figs. 5.7 and 5.8. This bias was calculated in the same way as the corrections for stellar variability in Sect. 5.5.1. However, instead of the observed stellar variability, we calculated the bias for different amounts of stellar dimming in the GROND i-band. As can be seen it is very unlikely that star spots are responsible for the higher g-band and  $K_s$ -band values. To explain the g-band measurement, a large part of the stellar surface ( $>20\%$ ) has to be covered in starspots, which would lead to a much lower radius ratio in the near and mid-infrared than observed.

However, this argument can also be turned around. Although the observed transmission spectrum cannot be explained by a baseline of unocculted starspots, if there is a significant baseline present, the shape of the planet's transmission spectrum can also be altered in such a way that the observed transmission spectrum appears relatively flat. We therefore also investigate how the starspots can change the shape of the transmission spectrum. To demonstrate this impact, we applied a correction for the spot base level, assuming that the star is dimmed by 5% in the i-band, which corresponds to a spot covering fraction of 10% of the stellar surface. In the bottom panels of Figs. 5.7 and 5.8 we show this corrected transmission spectrum, where, to make comparison with the earlier results easier, we have shifted the values such that the i-band radius ratio is unaltered. The effect of this correction is to push the near and mid-infrared points to larger radius ratios with respect to the optical measurements. The increased radius ratio in the infrared is then more consistent with a geometrically thick atmosphere, although we require a strongly reduced methane content in order to explain both our  $K_c$ -band and IRAC points. At the red part of the optical spectrum the correction introduces a tilt towards smaller radii for shorter wavelengths, which is opposite to the tilt expected from Rayleigh scattering in the atmosphere of the planet, which causes an increase in the radius ratio.

From this example it is clear that not only stellar variability needs to be taken into account when comparing the transmission spectrum at different wavelengths and times, but that it is also extremely important to investigate the impact of the base level of star spots on the observed transmission spectrum.

## 5.7 Conclusions

We have presented observations of 8 transits of GJ1214b, in the g-, r-, i-, I- and z-bands in the optical, and  $K_s$ - and  $K_c$ -bands in the near-infrared, allowing us to determine the planet-to-star radius ratio of this system at these wavelengths. All measurements show within errors a similar size ratio, except for the g-band, for which this ratio is larger at the  $\sim 2\sigma$  level. If real, this could be attributed to Rayleigh scattering within the planet's atmosphere, and subsequently points to a large scale height and therefore a hydrogen/helium dominated atmosphere. However, this requires more observations to confirm.

When combining our observations with all the currently available literature values, the data again favour a model with an extended atmosphere, a low methane content and a cloud-layer at 0.5 bar, above that for a water dominated atmosphere.

In addition, it is very important to take into account the base-level of stellar spots, which can

significantly alter the shape of the transmission spectrum, by increasing the radius ratios measured at optical wavelengths compared to those at near- and mid-infrared wavelengths. When this effect is removed, the relative increases in the planet-to-star size ratios in the near- and mid-infrared make those measurements more consistent with an atmosphere with a large scale-height compared to an atmosphere which is dominated by water vapour.

## **Acknowledgements**

We are grateful to the staff of the NOT telescope for their assistance with these observations. We like to thank Marco Nardini for assistance with the GROND observations. Based on observations made with the Nordic Optical Telescope, operated on the island of La Palma jointly by Denmark, Finland, Iceland, Norway, and Sweden, in the Spanish Observatorio del Roque de los Muchachos of the Instituto de Astrofísica de Canarias. The Isaac Newton Telescope is operated on the island of La Palma by the Isaac Newton Group in the Spanish Observatorio del Roque de los Muchachos of the Instituto de Astrofísica de Canarias. Part of the funding for GROND (both hardware as well as personnel) was generously granted from the Leibniz-Prize to Prof. G. Hasinger (DFG grant HA 1850/28-1).

## Bibliography

- Acosta-Pulido, J., Ballesteros, E., Barreto, M., et al. 2002, The Newsletter of the Isaac Newton Group of Telescopes, 6, 22
- Bean, J. L., Kempton, E., & Homeier, D. 2010, *Nature*, 468, 669
- Berta, Z. K., Charbonneau, D., Bean, J., et al. 2011, *ApJ*, 736, 12
- Borysow, A. 2002, *A&A*, 390, 779
- Carter, J. A., Winn, J. N., Holman, M. J., et al. 2011, *ApJ*, 730, 82
- Charbonneau, D., Berta, Z. K., Irwin, J., et al. 2009, *Nature*, 462, 891
- Charbonneau, D., Brown, T. M., Noyes, R. W., & Gilliland, R. L. 2002, *ApJ*, 568, 377
- Claret, A. 2000, *A&A*, 363, 1081
- Claret, A. 2004, *A&A*, 428, 1001
- Colon, K. D., Ford, E. B., Redfield, S., et al. 2010, ArXiv:1008.4800 [astro-ph.EP]
- Croll, B., Albert, L., Jayawardhana, R., et al. 2011, ArXiv:1104.0011 [astro-ph.EP]
- Désert, J.-M., Bean, J., Miller-Ricci Kempton, E., et al. 2011, *ApJ*, 731, L40+
- Gelman, A. & Rubin, D. B. 1992, *Statistical Science*, 7, 457–472
- Greiner, J., Bornemann, W., Clemens, C., et al. 2008, *PASP*, 120, 405
- Hauschildt, P. H., Allard, F., Ferguson, J., Baron, E., & Alexander, D. R. 1999, *ApJ*, 525, 871
- Mandel, K. & Agol, E. 2002, *ApJ*, 580, L171
- Markwardt, C. B. 2009, in *Astronomical Society of the Pacific Conference Series*, Vol. 411, *Astronomical Data Analysis Software and Systems XVIII*, ed. D. A. Bohlender, D. Durand, & P. Dowler, 251
- Miller-Ricci, E. & Fortney, J. J. 2010, *ApJ*, 716, L74
- Pont, F., Knutson, H., Gilliland, R. L., Moutou, C., & Charbonneau, D. 2008, *MNRAS*, 385, 109
- Redfield, S., Endl, M., Cochran, W. D., & Koesterke, L. 2008, *ApJ*, 673, L87
- Rogers, L. A. & Seager, S. 2010, *ApJ*, 716, 1208
- Rothman, L. S., Gordon, I. E., Barbe, A., et al. 2009, *J. Quant. Spec. Radiat. Transf.*, 110, 533
- Rothman, L. S., Gordon, I. E., Barber, R. J., et al. 2010, *J. Quant. Spec. Radiat. Transf.*, 111, 2139
- Sing, D. K., Désert, J., Fortney, J. J., et al. 2011a, *A&A*, 527, A73+
- Sing, D. K., Pont, F., Aigrain, S., et al. 2011b, ArXiv:1103.0026 [astro-ph.EP]
- Snellen, I. A. G., Albrecht, S., de Mooij, E. J. W., & Le Poole, R. S. 2008, *A&A*, 487, 357
- Snellen, I. A. G., de Kok, R. J., de Mooij, E. J. W., & Albrecht, S. 2010, *Nature*, 465, 1049
- Swain, M. R., Vasisht, G., & Tinetti, G. 2008, *Nature*, 452, 329
- Tinetti, G., Vidal-Madjar, A., Liang, M., et al. 2007, *Nature*, 448, 169
- Vidal-Madjar, A., Désert, J., Lecavelier des Etangs, A., et al. 2004, *ApJ*, 604, L69
- Vidal-Madjar, A., Lecavelier des Etangs, A., Désert, J., et al. 2003, *Nature*, 422, 143





---

## Chapter 6

---

# An ensemble study of the day-side spectra of hot Jupiters

During the past few years, many measurements of thermal emission from hot Jupiters have become available, ranging from the optical to the mid-infrared wavebands. So far these observations have almost exclusively been interpreted on a planet-to-planet basis for making inferences about their atmospheres, in particular about the temperature structure.

The aim of this chapter is to use all known hot Jupiter secondary eclipse measurements, and perform a statistical study of their emission properties as a function of their environment, such as the level of the incident stellar radiation and stellar activity. These environmental parameters have been proposed to drive the temperature structure in hot Jupiter atmospheres.

We have collected all the currently available secondary eclipse measurements of exoplanets from the literature, and converted these data into brightness temperatures. We compared these brightness temperatures with the expected equilibrium temperatures of the planets, and searched for correlation of their surface brightness with stellar irradiation and activity. We construct mean spectra for the entire sample, as well as for the strongly ( $\log(F_{\text{inc}}) > 9.2$ ) and weakly ( $\log(F_{\text{inc}}) < 9.2$ ) irradiated hot Jupiters, and for those orbiting active ( $\log(R_{HK}) > -4.9$ ) and quiet stars ( $\log(R_{HK}) < -4.9$ ).

Our main results are as follows:

- 1) We confirm that the mean day-side spectrum of a hot Jupiter significantly deviates from that of a blackbody: at optical and near-infrared wavelengths the brightness temperatures are higher and at 3.5 and 4.5  $\mu\text{m}$  they are lower than expected from their equilibrium temperatures.
- 2) The mean variations in brightness temperature as a function of wavelength are significantly different for planets orbiting active stars than for those orbiting quiet stars. These differences in brightness temperature variations are much smaller between samples of planets at low and high levels of irradiation.
- 3) From comparing their overall spectral energy distribution with their theoretical equilibrium temperatures, planets around quiet stars have, on average, a higher reradiation efficiency and lower albedo than planets orbiting active stars. These differences are again smaller for high and low irradiated planets. However, the determination of the planet effective temperatures are hampered by the limited availability of eclipse measurements in the near-infrared, where hot Jupiters peak in their spectral energy distribution.
- 4) Qualitatively, the mean emission spectrum of planets orbiting quiet stars appears to be consistent with models with an atmospheric inversion layer, while the average spectrum of planets orbiting active stars is consistent with atmospheric models without such a thermal inversion.

## 6.1 Introduction

Since the first successful detections of secondary eclipses of exoplanets (Charbonneau et al. 2005; Deming et al. 2005), the number of such measurements has increased rapidly. Currently there are about thirty planets for which the eclipse has been detected at one or more wavelengths. So far, most of these measurements have been made using the Spitzer Space Telescope in the mid-infrared. However, ground-based measurements in the near-infrared and at optical wavelengths have also become possible (e.g. Chapters 2 to 4).

Most of the atmospheric studies have been performed on a planet-to-planet basis. From these studies a picture has emerged that some planets show an inversion layer (e.g. HD209458b Knutson et al. 2008), and some planets do not (e.g. HD189733b Knutson et al. 2009c). An inversion layer is a region in the atmosphere at low pressures where the temperature increases with increasing altitude, rather than decreases. This requires a large amount of the incident stellar radiation to be absorbed in such a region, and therefore a very efficient absorber is required high up in the atmosphere.

To explain the presence of such a high altitude absorber in the atmosphere of some planets but not in others, Fortney et al. (2008) suggest that at low temperatures the absorber could condense, causing it to be removed from the gas phase, while at higher temperatures the absorber would remain in the gas phase. This scheme couples the presence of an inversion layer to the level of incident stellar radiation at the planet, since that is closely linked to the atmospheric temperature at higher altitude. As a possible absorber Burrows et al. (2008) suggest TiO and VO which in the gas-phase absorb very efficiently at optical wavelengths.

Recently, Knutson et al. (2010) investigated the stellar activity of exoplanet host-stars, and found that planets with an inversion layer are more likely to orbit stars that are less active than planets without an inversion layer. They suggest a scheme in which the higher UV-radiation emitted by active stars could influence photochemistry in hot Jupiter atmospheres, destroying the compound responsible for the inversion layer. Candidates for such a compound could for instance be sulphur based (e.g. HS and S<sub>2</sub> Zahnle et al. 2009).

In contrast, Madhusudhan & Seager (2010) investigated the atmospheric properties of four hot Jupiters for which an inversion layer was inferred with a large grid of atmospheric models that spanned wide ranges in chemical composition and temperature-pressure profiles. From this they find that in a few of these planets there is a degeneracy between the temperature structure of the planet's atmosphere and the chemical composition, making the inference of an inversion layer for some planets not robust.

All the studies mentioned previously are based on fitting models to individual planets. Recently Cowan & Agol (2011) studied the albedos and reradiation efficiencies for a large sample of hot Jupiters, to determine their average albedo and reradiation efficiency. They find that the hot Jupiters have typically a low albedo, but can span a wide range of reradiation efficiencies.

In this chapter, we want to extend their work, investigating the atmospheric properties of all hot Jupiters studied so far, searching for relations between the wavelength-dependent emission properties and the physical environment of the planet, such as level of stellar radiation and the stellar activity, which have both been suggested to drive the temperature structures in hot Jupiter atmospheres. In Sect. 6.2 we introduce the literature sample used for this study, in Sect. 6.3 we investigate the correlations between the brightness temperature and both the incident radiation and stellar activity. In Sect. 6.4 we present the average spectrum of a hot Jupiter, and in Sect. 6.5,

we present a grid of atmospheric models for a qualitative comparison. Finally we will discuss the results in Sect. 6.6, and the conclusions are given in Sect. 6.7.

The reader should note that we use the following common definitions in this paper: the *brightness temperature*,  $T_b$ , is a measure of the planet's surface brightness expressed as a black-body temperature. The *equilibrium temperature*,  $T_{\text{eq}}$ , is the expected temperature of a planet, calculated by balancing the incoming energy from the star with the outgoing radiation. For the calculation of the equilibrium temperature we assume that all the incident stellar radiation is absorbed and that all the absorbed energy is reradiated from the planet's day-side, which is considered to have a homogeneous temperature. The *effective temperature*,  $T_{\text{eff}}$ , is the temperature of a blackbody that emits the same total amount of radiation as the planet, and is a measure of its luminosity.

## 6.2 Data

### 6.2.1 Secondary eclipse measurements

Up until May 1, 2011, secondary eclipse measurements for twenty-nine different exoplanets have been reported in the literature or on arxiv.org. Twenty-seven of these planets are highly irradiated hot Jupiters in short ( $<10$  day) orbits around their host star. For our sample we selected all these short period hot Jupiters, and opted to only use those wavelength bands where there are detections available for at least three planets. Our data collection therefore consists of five distinct bandpasses, the  $K_s$ -band (into which we also group the narrowband observations from Gillon et al. (2009)) and the four bandpasses of the IRAC instrument on the Spitzer Space Telescope. In addition to these five single band bandpasses, we grouped together all the measurements at optical wavelengths, combining all the observations conducted at wavelengths shortward of  $1\mu\text{m}$ . However, note that one has to be cautious in using these data, since the observations, especially in the bluer bands (e.g. from Kepler), can be strongly affected by starlight reflected from the planet's atmosphere. It is, however, interesting to include observations of hot Jupiter atmospheres in the Wien limit of their emission spectrum.

The full list of eclipse measurements used for our study is given in Table 6.1, where we list the planets, their eclipse depths in different bands and the references for the data. For several planets multiple values within a certain bandpass are listed. In these cases, we use the weighted mean and uncertainty of the eclipse depths for the rest of our analysis. Note that these values are often obtained from a different analysis of the same dataset, and are therefore not independent.

For HD189733b Swain et al. (2009) presented secondary eclipse spectroscopy with the NICMOS on the Hubble Space Telescope in the near-infrared. We converted these measurements to a  $K_s$ -band eclipse depth by integrating the eclipse depth over the  $K_s$ -band weighted with the filter transmission curve and a Kurucz model spectrum for HD189733<sup>1</sup>. In this way we derive a  $K_s$ -band depth of 0.039%.

<sup>1</sup><http://kurucz.harvard.edu/stars/HD189733/>

**Table 6.1** — All the secondary eclipse measurements found in the literature in the optical, K<sub>s</sub>-band (2.15 $\mu$ m), and in the 3.6 to 8.0 $\mu$ m *Spitzer* IRAC bands. The references are given at the bottom of the table. Note that the optical observations, as well as the K-band observations have been made with a range of central wavelengths, listed below the table.

Planet	Eclipse depths (%)						References
	Optical	K <sub>s</sub> -band	IRAC 3.6 $\mu$ m	IRAC 4.5 $\mu$ m	IRAC 5.8 $\mu$ m	IRAC 8.0 $\mu$ m	
CoRoT-1b	0.016 $\pm$ 0.006 <sup>c</sup> 0.013 $\pm$ 0.003 <sup>d</sup>	0.278 $\pm$ 0.043 <sup>g</sup> 0.336 $\pm$ 0.042	0.415 $\pm$ 0.042	0.482 $\pm$ 0.042	—	—	(1, 3, 5, 5, <sup>-,-</sup> ) (2, 4, <sup>-,-,-,-</sup> )
CoRoT-2b	0.006 $\pm$ 0.002 <sup>c</sup> 0.010 $\pm$ 0.002 <sup>d</sup>	<0.1600 —	0.355 $\pm$ 0.020	0.510 $\pm$ 0.041	—	0.410 $\pm$ 0.110 0.446 $\pm$ 0.100	(6, 8, 12, 11, <sup>-,-,11</sup> ) (7, <sup>-,-,-,12,-,12</sup> )
HAT-P-1b	—	—	—	—	—	0.510 $\pm$ 0.059	( <sup>-,-,-,-,-,12</sup> )
HAT-P-7b	0.013 $\pm$ 0.001 <sup>b</sup> 0.009 $\pm$ 0.001 <sup>b</sup>	0.109 $\pm$ 0.025 —	0.080 $\pm$ 0.008 0.098 $\pm$ 0.017	0.135 $\pm$ 0.022 0.159 $\pm$ 0.022	0.203 $\pm$ 0.031 0.245 $\pm$ 0.031	0.238 $\pm$ 0.040 0.225 $\pm$ 0.052	( <sup>-,-,13,14,14,14,14</sup> ) (15, <sup>-,-,17,17,17,17</sup> )
HD149026b	—	—	—	—	—	—	(16, <sup>-,-,-,-,-,-</sup> )
HD189733b	—	0.039 $\pm$ 0.006	0.256 $\pm$ 0.014	0.214 $\pm$ 0.020	0.310 $\pm$ 0.034	0.391 $\pm$ 0.022	( <sup>-,-,-,-,-,18</sup> ) ( <sup>-,-,-,-,-,19</sup> )
HD209458b	<0.0007 <sup>a</sup>	—	0.094 $\pm$ 0.009	0.213 $\pm$ 0.015	0.301 $\pm$ 0.043	0.338 $\pm$ 0.005 0.344 $\pm$ 0.004	( <sup>-,-,-,-,-,22</sup> ) ( <sup>-,-,-,-,-,23</sup> )
Kepler-5b	0.002 $\pm$ 0.001 <sup>b</sup>	—	0.103 $\pm$ 0.017	0.107 $\pm$ 0.015	—	—	(26, <sup>-,-,26,26,-,-</sup> )
Kepler-6b	0.002 $\pm$ 0.001 <sup>b</sup>	—	0.069 $\pm$ 0.027	0.151 $\pm$ 0.019	—	—	(27, <sup>-,-,27,27,-,-</sup> )
Kepler-7b	0.005 $\pm$ 0.001 <sup>b</sup>	—	—	—	—	—	(28, <sup>-,-,-,-,-,-</sup> )

Table 6.1 — Continued.

Planet	Eclipse depths (%)						References
	Optical	Ks-band	IRAC 3.6 $\mu$ m	IRAC 4.5 $\mu$ m	IRAC 5.8 $\mu$ m	IRAC 8.0 $\mu$ m	
OGLE-TR-56b	0.036 $\pm$ 0.009 <sup>e</sup>	—	—	—	—	—	(30,-,-,-,-,-)
OGLE-TR-113b	—	0.170 $\pm$ 0.050	—	—	—	—	(-,29,-,-,-,-)
TrES-1b	—	—	0.085 $\pm$ 0.013	0.066 $\pm$ 0.013	—	0.225 $\pm$ 0.036	(-,31,32,-,32)
TrES-2b	<0.0002 <sup>b</sup>	0.062 <sup>+0.013</sup> <sub>-0.011</sub>	0.127 $\pm$ 0.021	0.230 $\pm$ 0.024	0.199 <sup>+0.054</sup> <sub>-0.021</sub>	0.359 <sup>+0.060</sup> <sub>-0.021</sub>	(33,34,35,35,35,35)
TrES-3b	—	0.174 $\pm$ 0.040	0.346 $\pm$ 0.035	0.372 $\pm$ 0.054	0.449 $\pm$ 0.097	0.475 $\pm$ 0.046	(-,37,38,38,38,38)
—	—	0.133 $\pm$ 0.018	—	—	—	—	(-,36,-,-,-,-)
TrES-4b	—	—	0.137 $\pm$ 0.011	0.148 $\pm$ 0.016	0.261 $\pm$ 0.059	0.318 $\pm$ 0.044	(-,39,39,39,39,39)
WASP-1b	—	—	0.184 $\pm$ 0.016	0.217 $\pm$ 0.017	0.274 $\pm$ 0.058	0.474 $\pm$ 0.046	(-,40,40,40,40,40)
—	—	—	0.117 $\pm$ 0.016	—	—	—	(-,40,-,-,-,-)
WASP-2b	—	—	0.083 $\pm$ 0.035	0.169 $\pm$ 0.017	0.192 $\pm$ 0.077	0.285 $\pm$ 0.059	(-,47,47,47,47,47)
WASP-4b	—	0.185 $\pm$ 0.014	0.319 $\pm$ 0.031	0.343 $\pm$ 0.027	—	—	(-,50,51,51,-,-)
WASP-12b	0.082 $\pm$ 0.015 <sup>e</sup>	0.310 $\pm$ 0.012	0.379 $\pm$ 0.013	0.382 $\pm$ 0.019	0.629 $\pm$ 0.052	0.636 $\pm$ 0.067	(41,42,43,43,43,43)
WASP-17b	—	—	—	0.229 $\pm$ 0.013	—	0.237 $\pm$ 0.039	(-,,-,44,-,44)
WASP-18b	—	—	0.310 $\pm$ 0.020	0.380 $\pm$ 0.030	0.410 $\pm$ 0.020	0.430 $\pm$ 0.030	(-,45,45,45,45,45)
WASP-19b	—	0.366 $\pm$ 0.072	—	—	—	—	(-,46,-,-,-,-)
WASP-33b	0.109 $\pm$ 0.030 <sup>f</sup>	0.244 <sup>+0.027</sup> <sub>-0.020</sub>	—	—	—	—	(48,49,-,-,-,-)

Table 6.1 — Continued.

Planet	Eclipse depths (%)				References		
	Optical	Ks-band	IRAC 3.6 $\mu$ m	IRAC 4.5 $\mu$ m		IRAC 5.8 $\mu$ m	IRAC 8.0 $\mu$ m
XO-1b	—	—	0.086 $\pm$ 0.007	0.122 $\pm$ 0.009	0.261 $\pm$ 0.031	0.210 $\pm$ 0.029	(-, -, 52, 52, 52, 52)
XO-2b	—	—	0.081 $\pm$ 0.017	0.098 $\pm$ 0.020	0.167 $\pm$ 0.036	0.133 $\pm$ 0.049	(-, -, 53, 53, 53, 53)
XO-3b	—	—	0.101 $\pm$ 0.004	0.143 $\pm$ 0.006	0.134 $\pm$ 0.049	0.150 $\pm$ 0.036	(-, -, 54, 54, 54, 54)

**Notes:** (a) MOST bandpass, (b) Kepler bandpass, (c) CoRoT white bandpass, (d) CoRoT red bandpass, (e) z-band

(f) SII filter, (g) NB2090 bandpass.

- References:** (1) Alonso et al. (2009a), (2) Snellen et al. (2009), (3) Gillon et al. (2009), (4) Rogers et al. (2009), (5) Deming et al. (2011), (6) Alonso et al. (2009b), (7) Snellen et al. (2010), (8) Alonso et al. (2010), (9) Gillon et al. (2010), (10) Deming et al. (2011), (11) Chapter 3, (12) Todorov et al. (2010), (13) Borucki et al. (2009), (14) Welsh et al. (2010) (15) Christiansen et al. (2010), (16) Knutson et al. (2009b), (17) Harrington et al. (2007), (18) Swain et al. (2009) (19) Charbonneau et al. (2008), (20) Knutson et al. (2007), (21) Agol et al. (2010), (22) Rowe et al. (2008) (23) Knutson et al. (2008), (24) Desert et al. (2011) (25) Desert et al. (2011), (26) Kipping & Bakos (2011a) (27) Snellen & Covino (2007), (28) Sing & López-Morales (2009), (29) Knutson et al. (2010) (30) Charbonneau et al. (2005) (31) Kipping & Bakos (2010), (32) Croll et al. (2010a), (33) O’Donovan et al. (2010) (34) Croll et al. (2010b), (35) Chapter 2, (36) Fressin et al. (2010) (37) Knutson et al. (2009a) (38) Wheatley et al. (2010), (39) López-Morales et al. (2010), (40) Croll et al. (2011), (41) Campo et al. (2011) (42) Anderson et al. (2011) (43) Nymeyer et al. (2010), (44) Gibson et al. (2010), (45) Wheatley et al. (2010) (46) Smith et al. (2011), (47) Chapter 4, (48) Caceres et al. (2011) (49) Beerer et al. (2011), (50) Machalek et al. (2008) (51) Machalek et al. (2009), (52) Machalek et al. (2010)

**Table 6.2** — The planet and stellar parameters used in our analysis. Column 1 gives the name of the planet, column 2 the planet to star radius ratio,  $R_p/R_*$ , column 3 gives the scaled semi major axis,  $a/R_*$ , and column 4 contains the stellar radius,  $R_*$ , column 5 contains the effective temperature of the host-star,  $T_{eff,*}$ , column 6 contains the stellar activity measurement,  $R_{HK}$ , from Knutson et al. (2010), column 7 contains the level of incident stellar radiation,  $F_{inc}$ , and in column 8 the references are given. In case of multiple references they are ordered as columns 2 to 5.

Planet	$R_p/R_*$	$a/R_*$	$R_*$ ( $R_{sun}$ )	$T_{eff,*}$ (K)	$\log(R_{HK})$	$F_{inc}$ (erg/sec/cm <sup>2</sup> )	References
CoRoT-1b	$0.1388 \pm 0.0021$	$4.920 \pm 0.080$	$1.110 \pm 0.050$	$5950 \pm 150$	-5.312	$2.94 \pm 0.30 \cdot 10^9$	(1)
CoRoT-2b	$0.1667 \pm 0.0006$	$6.700 \pm 0.030$	$0.902 \pm 0.018$	$5625 \pm 120$	-4.331	$1.26 \pm 0.11 \cdot 10^9$	(2)
HAT-P-1b	$0.1125 \pm 0.0036$	$10.695 \pm 0.286$	$1.112 \pm 0.032$	$5975 \pm 50$	-4.984	$6.32 \pm 0.24 \cdot 10^8$	(3)
HAT-P-7b	$0.0820 \pm 0.0001$	$4.350 \pm 0.380$	$1.840 \pm 0.230$	$6350 \pm 80$	-5.018	$4.87 \pm 0.27 \cdot 10^9$	(4,5,5,5)
HD149026b	$0.0486 \pm 0.0079$	$7.143 \pm 0.612$	$1.290 \pm 0.120$	$6147 \pm 50$	-5.030	$1.59 \pm 0.06 \cdot 10^9$	(3)
HD189733b	$0.1573 \pm 0.0052$	$8.985 \pm 0.250$	$0.752 \pm 0.025$	$5050 \pm 50$	-4.501	$4.57 \pm 0.19 \cdot 10^8$	(3)
HD209458b	$0.1221 \pm 0.0015$	$8.784 \pm 0.032$	$1.162 \pm 0.014$	$6117 \pm 50$	-4.970	$1.03 \pm 0.04 \cdot 10^9$	(3)
Kepler-5b	$0.0789 \pm 0.0002$	$6.340 \pm 0.090$	$1.709 \pm 0.029$	$6297 \pm 60$	-5.037	$2.22 \pm 0.10 \cdot 10^9$	(6)
Kepler-6b	$0.0949 \pm 0.0006$	$7.210 \pm 0.180$	$1.325 \pm 0.042$	$5647 \pm 88$	-5.005	$1.11 \pm 0.07 \cdot 10^9$	(7)
Kepler-7b	$0.0808 \pm 0.0005$	$7.290 \pm 0.200$	$1.791 \pm 0.067$	$5933 \pm 88$	-5.099	$1.32 \pm 0.08 \cdot 10^9$	(8)
OGLE-TR-56b	$0.0979 \pm 0.0139$	$4.082 \pm 0.433$	$1.260 \pm 0.140$	$6119 \pm 62$	—	$4.77 \pm 0.23 \cdot 10^9$	(3)
OGLE-TR-113b	$0.1464 \pm 0.0066$	$6.281 \pm 0.170$	$0.780 \pm 0.030$	$4804 \pm 106$	—	$7.66 \pm 0.68 \cdot 10^8$	(3)
TrES-1b	$0.1381 \pm 0.0044$	$10.373 \pm 0.194$	$0.818 \pm 0.021$	$5226 \pm 50$	-4.738	$3.93 \pm 0.16 \cdot 10^8$	(3)
TrES-2b	$0.1294 \pm 0.0042$	$7.800 \pm 0.213$	$1.002 \pm 0.031$	$5795 \pm 73$	-4.949	$1.05 \pm 0.06 \cdot 10^9$	(3)
TrES-3b	$0.1640 \pm 0.0036$	$6.002 \pm 0.061$	$0.818 \pm 0.014$	$5650 \pm 75$	-4.549	$1.60 \pm 0.09 \cdot 10^9$	(3)

Table 6.2 — Continued.

Planet	$R_p/R_*$	$a/R_*$	$R_*$ ( $R_{sun}$ )	$T_{eff,*}$ (K)	$\log(R_{HK})$	$F_{inc}$ (erg/sec/cm <sup>2</sup> )	References
TrES-4b	$0.0969 \pm 0.0080$	$5.549 \pm 0.256$	$1.920 \pm 0.111$	$6200 \pm 75$	-5.104	$2.72 \pm 0.14 \cdot 10^9$	(3)
WASP-1b	$0.1048 \pm 0.0064$	$5.757 \pm 0.295$	$1.455 \pm 0.079$	$6110 \pm 50$	-5.114	$2.38 \pm 0.09 \cdot 10^9$	(3)
WASP-2b	$0.1329 \pm 0.0042$	$8.078 \pm 0.117$	$0.807 \pm 0.022$	$5150 \pm 80$	-5.054	$6.11 \pm 0.39 \cdot 10^8$	(3)
WASP-4b	$0.1541 \pm 0.0041$	$5.479 \pm 0.033$	$0.905 \pm 0.024$	$5500 \pm 100$	-4.865	$1.73 \pm 0.13 \cdot 10^9$	(3)
WASP-12b	$0.1119 \pm 0.0020$	$3.097 \pm 0.082$	$1.599 \pm 0.071$	$6300 \pm 150$	-5.500	$9.31 \pm 0.91 \cdot 10^9$	(9)
WASP-17b	$0.1302 \pm 0.0010$	$7.060 \pm 0.250^a$	$1.572 \pm 0.056$	$6650 \pm 80$	-5.331	$2.22 \pm 0.12 \cdot 10^9$	(10)
WASP-18b	$0.0974 \pm 0.0046$	$3.578 \pm 0.108$	$1.222 \pm 0.043$	$6400 \pm 100$	-5.430	$7.43 \pm 0.49 \cdot 10^9$	(3)
WASP-19b	$0.1435 \pm 0.0007$	$3.567 \pm 0.077^a$	$0.990 \pm 0.020$	$5500 \pm 100$	-4.660	$4.08 \pm 0.31 \cdot 10^9$	(11,11,11,12)
WASP-33b	$0.1066 \pm 0.0009$	$3.788 \pm 0.081$	$1.444 \pm 0.034$	$7430 \pm 100$	—	$1.20 \pm 0.07 \cdot 10^{10}$	(13)
XO-1b	$0.1316 \pm 0.0045$	$11.287 \pm 0.242$	$0.942 \pm 0.024$	$5750 \pm 50$	-4.958	$4.87 \pm 0.19 \cdot 10^8$	(3)
XO-2b	$0.1051 \pm 0.0064$	$8.084 \pm 0.307$	$0.970 \pm 0.041$	$5340 \pm 50$	-4.988	$7.06 \pm 0.29 \cdot 10^8$	(3)
XO-3b	$0.0910 \pm 0.0035$	$6.911 \pm 0.220$	$1.409 \pm 0.056$	$6429 \pm 75$	—	$2.03 \pm 0.10 \cdot 10^9$	(3)

<sup>a</sup> Derived from parameters in the reference.

**References:**

- (1) Barge et al. (2008), (2) Alonso et al. (2008), (3) Southworth (2010) and references therein, (4) Borucki et al. (2009), (5) Pál et al. (2008), (6) Kipping & Bakos (2011b), (7) Kipping & Bakos (2011b), (8) Kipping & Bakos (2011b) (9) Chan et al. (2011) (10) Anderson et al. (2011), (11) Hellier et al. (2011), (12) Hebb et al. (2010) (13) Collier Cameron et al. (2010)



### 6.2.2 System parameters

In addition to the eclipse measurements, we also collected the parameters of the planets and their host stars required to convert the eclipse depths into brightness temperatures, and also to calculate the level of incident radiation on the planets (see next subsection). In addition we used the stellar activity measurements,  $\log(R_{\text{HK}})$ , from Knutson et al. (2010), to search for correlations with the stellar activity. The parameters, and the reference from which they were taken, are listed in Table 6.2.

In addition, we used the NextGen models (Hauschildt et al. 1999) to convert the stellar parameters into stellar spectra, which were interpolated to the effective temperature and surface gravity of the host star. For all stars we assumed solar metallicities.

### 6.2.3 Conversion to physical units

The stellar fluxes were determined by integrating the stellar spectra over the different bandpasses. Since the secondary eclipse measurements used in this paper have been obtained using broad-band filters, the fluxes of the star (and the planet) need to be integrated over the bandpass of the filters. The K-band observations have often been taken with different instruments with slightly different throughputs. We used the  $K_s$ -band filtercurve for the LIRIS instrument for all  $K_s$ -band measurements, while for the NB2090 observations, we adopted the data from the HAWK-I instrument. For the *Spitzer* IRAC-channels, the bandpasses were obtained from the IPAC website<sup>2</sup>. The Kepler filtercurve was obtained from the Kepler-website, while the MOST and CoRoT filter curves were extracted from the papers describing the respective instruments (Walker et al. (2003) for MOST and Auvergne et al. (2009) for CoRoT). For the SII filtercurve we used the data from the ING filter database (filter #88) and the z-band curve was obtained through the SDSS website. In addition, the level of incident stellar radiation at the planet's surface was calculated using the effective temperature of the star and the scaled semi-major axis ( $a/R_*$ ) as  $F_{\text{inc}} = \sigma T_{\text{eff},*}^4 (R_*/a)^2$ , which is given in Table 6.2. From the level of incident radiation the equilibrium temperature is calculated, assuming a homogeneous day-side temperature with no redistribution of the absorbed stellar flux to the night side,  $T_{\text{eq}} = (0.5 \cdot F_{\text{inc}} / \sigma)^{1/4}$ . These equilibrium temperatures are given in Table 6.3.

Subsequently the brightness temperature, which is simply a measure of the planet's surface brightness expressed in a blackbody temperature, was calculated for each planet in each of the bandpasses. The eclipse depths were converted to a flux by dividing them with the transit depths ( $= (R_p/R_*)^2$ ) and multiplying the result with the stellar flux integrated over the bandpass. The planetary flux was then compared to a grid of blackbody fluxes in the bandpass for different temperatures. The resulting brightness temperatures for the planets are given in Table 6.3.

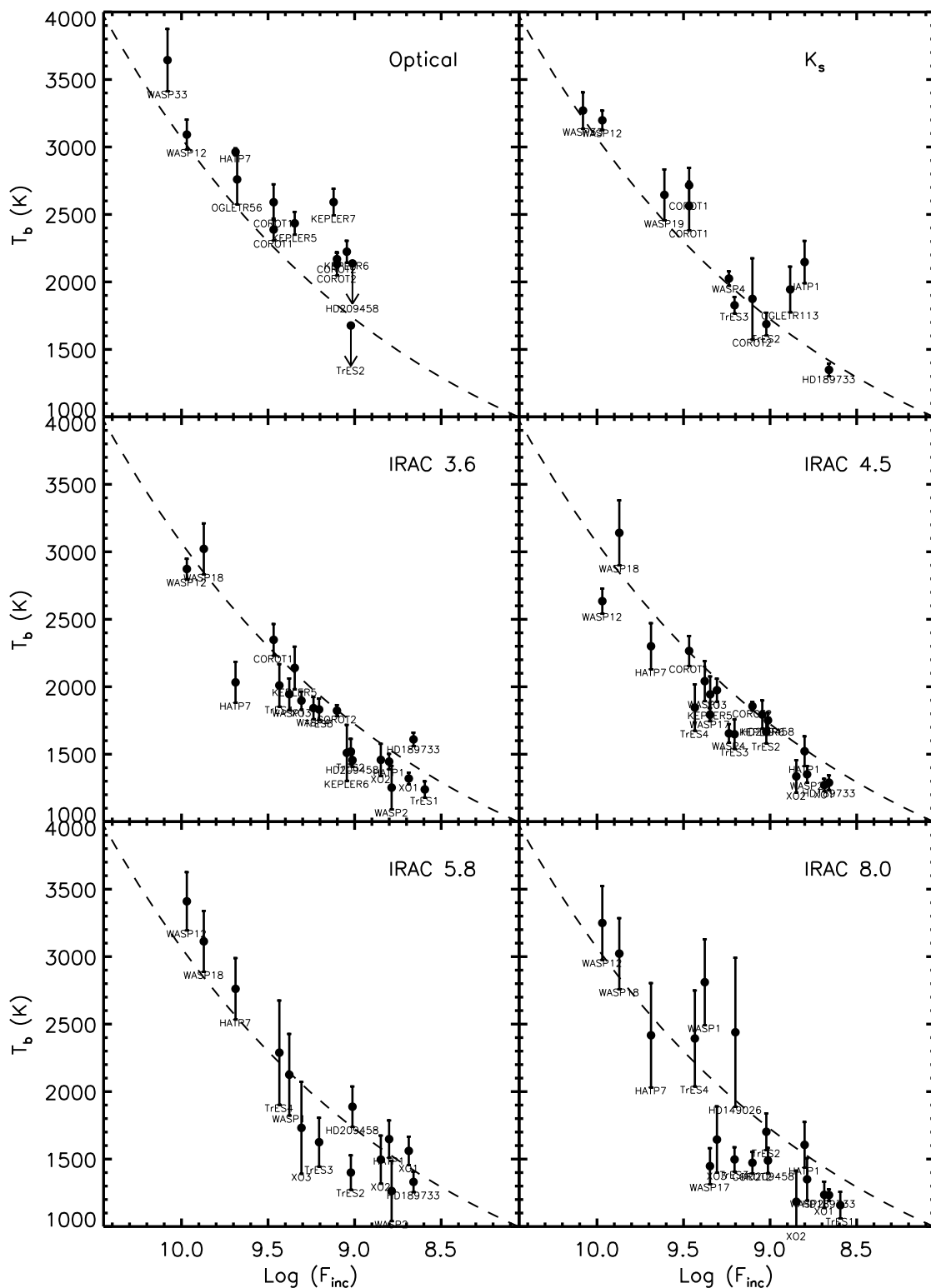


**Figure 6.1** — Planet brightness temperatures as a function of the incident radiation for the optical,  $K_s$ -band (top left and right panels), the IRAC 3.6  $\mu\text{m}$  and 4.5  $\mu\text{m}$  bands (middle left and right panels) and the IRAC 5.8  $\mu\text{m}$  and 8.0  $\mu\text{m}$  bands (bottom left and right panels). The dashed line is the equilibrium temperature as derived from the level of the incident radiation.

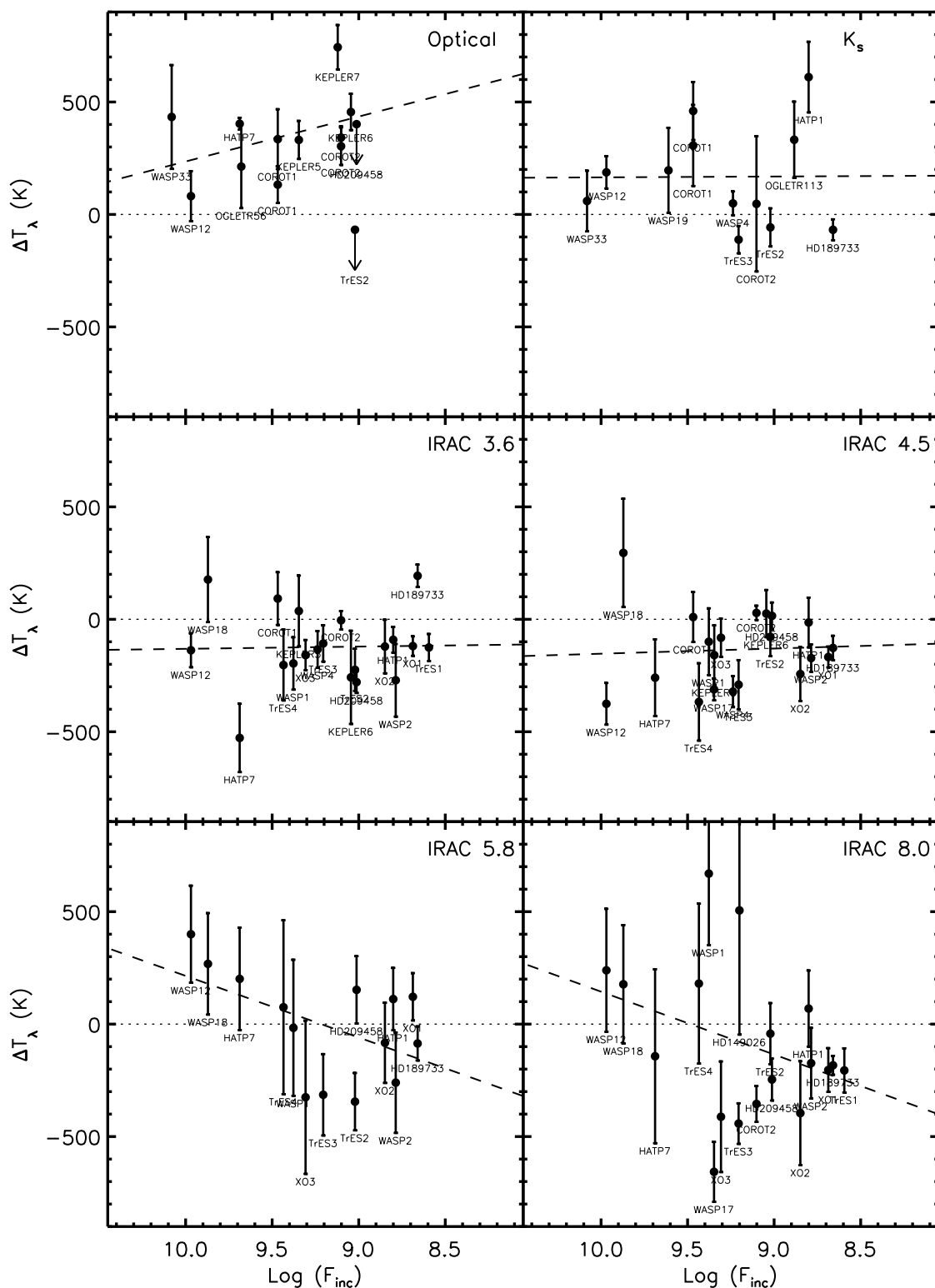


**Figure 6.2** — The difference between the brightness temperatures and the equilibrium temperature,  $\Delta T_\lambda$ , as a function of the incident radiation. The panels are in the same order as for Fig. 6.1. The dashed line shows the best linear fit to  $\Delta T_\lambda$  as a function of  $\log(F_{\text{inc}})$ .

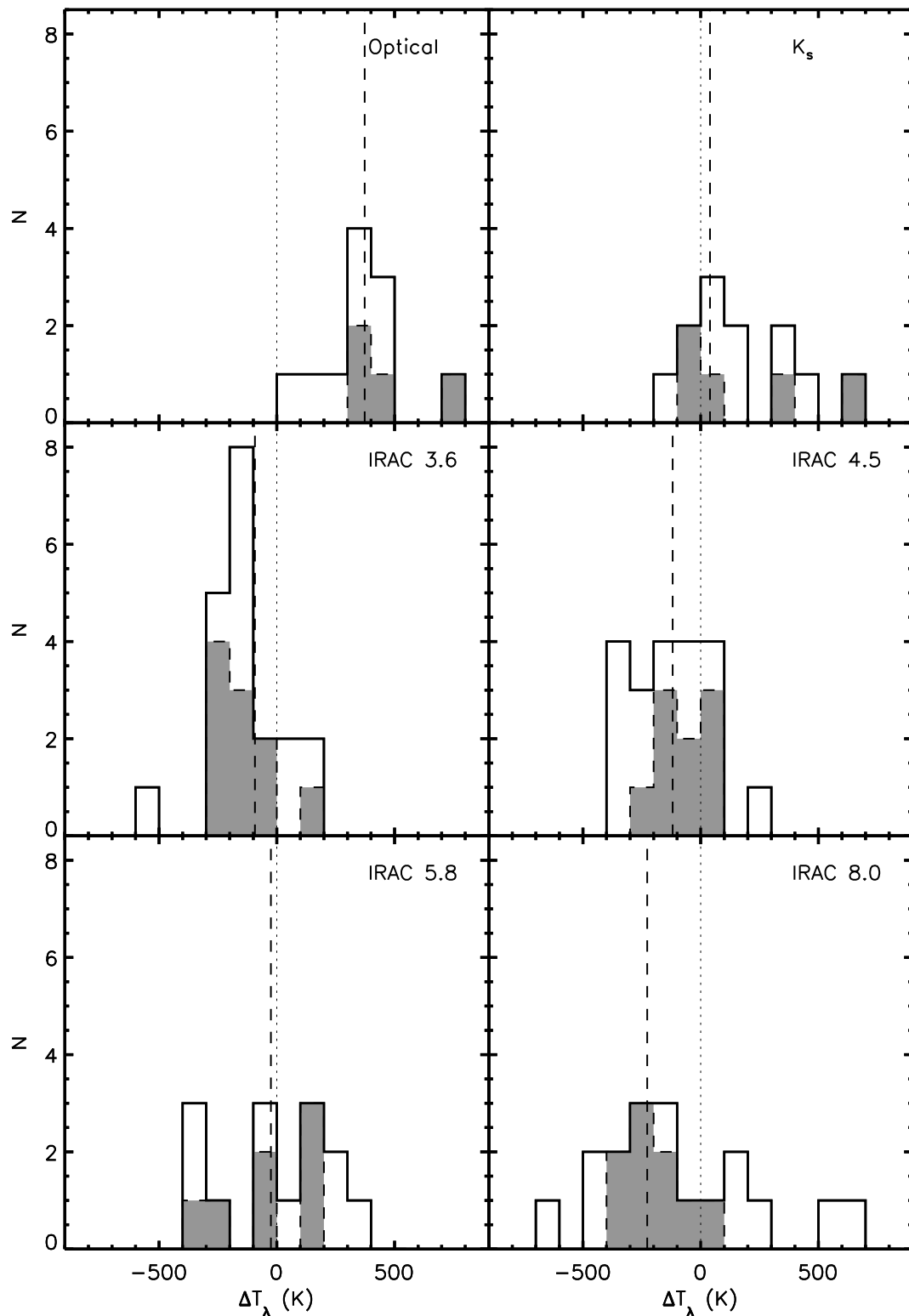


**Figure 6.3** — Histograms of  $\Delta T_\lambda$ , for the six bands used in this paper. The shaded areas are for the planets that receive less than  $1.6 \cdot 10^9$  erg/sec/cm<sup>2</sup> (the 'cool' sample), while the unshaded histogram is for the entire sample. The vertical dashed line shows the mean of the sample in each waveband.

Table 6.3 — The derived brightness temperatures for the planets in the different bands.

Planet	Optical	Ks-band	$T_b$ (K)				$T_{eq}$ (K)
			IRAC 3.6 $\mu$ m	IRAC 4.5 $\mu$ m	IRAC 5.8 $\mu$ m	IRAC 8.0 $\mu$ m	
CoRoT-1b	2590 $\pm$ 113 <sup>c</sup> 2388 $\pm$ 73 <sup>d</sup>	2562 $\pm$ 136 <sup>g</sup> 2715 $\pm$ 126	2347 $\pm$ 115	2265 $\pm$ 110	—	—	2255
CoRoT-2b	2130 $\pm$ 72 <sup>c</sup> 2169 $\pm$ 46 <sup>d</sup>	1874 $\pm$ 255	1822 $\pm$ 40	1855 $\pm$ 31	—	1472 $\pm$ 79	1827
HAT-P-1b	—	2147 $\pm$ 148	1445 $\pm$ 55	1522 $\pm$ 107	1647 $\pm$ 136	1605 $\pm$ 167	1536
HAT-P-7b	2963 $\pm$ 25 <sup>b</sup>	—	2032 $\pm$ 148	2300 $\pm$ 168	2761 $\pm$ 226	2417 $\pm$ 383	2560
HD149026b	—	—	—	—	—	2439 $\pm$ 545	1934
HD189733b	—	1348 $\pm$ 44	1609 $\pm$ 49	1289 $\pm$ 52	1330 $\pm$ 74	1233 $\pm$ 41	1416
HD209458b	<2136 <sup>a</sup>	—	1456 $\pm$ 47	1750 $\pm$ 58	1887 $\pm$ 148	1489 $\pm$ 92	1735
Kepler-5b	2434 $\pm$ 74 <sup>b</sup>	—	2139 $\pm$ 154	1943 $\pm$ 130	—	—	2102
Kepler-6b	2224 $\pm$ 70 <sup>b</sup>	—	1510 $\pm$ 191	1793 $\pm$ 103	—	—	1768
Kepler-7b	2591 $\pm$ 87 <sup>b</sup>	—	—	—	—	—	1847
OGLE-TR-113b	—	1943 $\pm$ 156	—	—	—	—	1611
OGLE-TR-56b	2759 $\pm$ 160 <sup>e</sup>	—	—	—	—	—	2546
TrES-1b	—	—	1239 $\pm$ 57	970 $\pm$ 55	—	1158 $\pm$ 96	1364
TrES-2b	<1676 <sup>b</sup>	1687 $\pm$ 86	1520 $\pm$ 90	1666 $\pm$ 88	1400 <sup>+174</sup> <sub>-80</sub>	1702 <sup>+181</sup> <sub>-90</sub>	1744
TrES-3b	—	1827 $\pm$ 58	1831 $\pm$ 79	1648 $\pm$ 107	1625 $\pm$ 176	1497 $\pm$ 89	1939
TrES-4b	—	—	2009 $\pm$ 153	1845 $\pm$ 167	2288 $\pm$ 379	2393 $\pm$ 352	2213
WASP-2b	—	—	1252 $\pm$ 145	1351 $\pm$ 59	1263 $\pm$ 210	1349 $\pm$ 154	1523
WASP-1b	—	—	1945 $\pm$ 114	2041 $\pm$ 146	2124 $\pm$ 297	2810 $\pm$ 316	2141

Table 6.3 — Continued.

Planet	$T_b$ (K)							$T_{eq}$ (K)
	Optical	Ks-band	IRAC 3.6 $\mu$ m	IRAC 4.5 $\mu$ m	IRAC 5.8 $\mu$ m	IRAC 8.0 $\mu$ m		
WASP-4b	—	2025 $\pm$ 53	1841 $\pm$ 80	1654 $\pm$ 68	—	—	—	1975
WASP-12b	3091 $\pm$ 104 <sup>e</sup>	3197 $\pm$ 69	2872 $\pm$ 75	2634 $\pm$ 92	3410 $\pm$ 215	3249 $\pm$ 272	3010	3010
WASP-17b	—	—	—	1792 $\pm$ 48	—	1447 $\pm$ 131	2104	2104
WASP-18b	—	—	3021 $\pm$ 187	3140 $\pm$ 239	3113 $\pm$ 224	3022 $\pm$ 262	2845	2845
WASP-19b	—	2644 $\pm$ 182	—	—	—	—	2448	2448
WASP-33b	3643 $\pm$ 212 <sup>f</sup>	3269 <sup>+152</sup> <sub>-117</sub>	—	—	—	—	3210	3210
XO-1b	—	—	1320 $\pm$ 42	1271 $\pm$ 45	1560 $\pm$ 103	1235 $\pm$ 95	1439	1439
XO-2b	—	—	1458 $\pm$ 113	1335 $\pm$ 115	1496 $\pm$ 173	1183 $\pm$ 221	1579	1579
XO-3b	—	—	1897 $\pm$ 66	1974 $\pm$ 84	1731 $\pm$ 328	1644 $\pm$ 241	2056	2056

**Notes:** (a) MOST bandpass, (b) Kepler bandpass, (c) CoRoT white bandpass, (d) CoRoT red bandpass, (e) z-band (f) SII filter, (g) NB2090 bandpass.

## 6.3 Correlations with brightness temperature

### 6.3.1 Relation with incident radiation

In Fig. 6.1 the brightness temperatures in the different bands are shown as functions of incident radiation. The general trends are as expected: a lower level of incident radiation results in a lower brightness temperature. However, in some bands the brightness temperatures of most planets appear higher than the equilibrium temperature (e.g. in the optical and  $K_s$ -band). They are typically lower in other bands (e.g. the IRAC  $3.6\mu\text{m}$  and  $4.5\mu\text{m}$ ). To investigate this further, the differences between the observed brightness temperature and the expected equilibrium temperature for the different wavelengths,  $\Delta T_\lambda \equiv T_b(\lambda) - T_{\text{eq}}$ , are shown in Fig. 6.2. In addition, histograms of  $\Delta T_\lambda$  for the different wavelength bands are shown in Fig. 6.3. The offsets in the different wavebands are clearly visible in these diagrams. It shows that a typical spectrum of a hot Jupiter clearly deviates from that of a blackbody (see Sect. 6.5). We note again that the optical observations are a combination of observations spanning a large range of wavelengths.

In Table 6.5 the scatter of  $\Delta T_\lambda$  for each of the bandpasses is given. This scatter is in most cases comparable to the typical uncertainties in the values for the individual planets, which indicates that on average the uncertainties assigned to the eclipse measurements are not significantly underestimated.

In several wavelength bands there are trends visible of  $\Delta T_\lambda$  as a function of stellar irradiation, which could be due to changing atmospheric properties. To investigate the trends, we performed a linear fit between  $\Delta T_\lambda$  and  $\log(F_{\text{inc}})$  in each of the bandpasses. To avoid biasing the results to the few planets with small errorbars, we assumed uniform uncertainties for all planets equal to the average of their uncertainties in  $T_b$ . To assess the robustness of the trend, and the uncertainties, we performed a simple bootstrap analysis, where the linear fit was performed repeatedly, on a sample with the same number of objects randomly drawn from the observed  $\Delta T_\lambda$ , where a planet could appear multiple times in the sample. The 16% and 84% region of the distribution of the fitted slopes was used for the  $1-\sigma$  confidence interval. The results of the analysis are shown in Table 6.4. In most bands no significant correlations are found. Only for the IRAC  $5.8$  &  $8.0\mu\text{m}$  bands are the relations marginally significant at a  $> 2\sigma$  level.

### 6.3.2 Relation with stellar activity

Knutson et al. (2010) find a relation between stellar activity and the presence or absence of an inversion layer, which they infer from comparing the observed slope between the IRAC  $3.6\mu\text{m}$  and  $4.5\mu\text{m}$  and the slope of a blackbody fitted to these two observations. A planet is considered to have an inversion layer when the difference in the slope is larger than  $-0.05\%$ . In Fig. 6.4 this diagnostic for an inversion layer is shown as a function of both the incident stellar radiation (top panel) and as a function of the stellar activity (from Knutson et al. 2010) (bottom panel). No preference is found for planets that are considered to have an inversion layer to be located at a certain level of incident radiation. However, as already found by Knutson et al. (2010), the planets without an inversion layer all orbit active stars. Note that CoRoT-2b, which according to the diagnostic has an inversion layer and orbits an active star, has an observed emission spectrum that is difficult to fit both with models with an inversion layer and without (Deming

<sup>2</sup><http://irsa.ipac.caltech.edu/data/SPITZER/docs/irac/calibrationfiles/spectralresponse/>

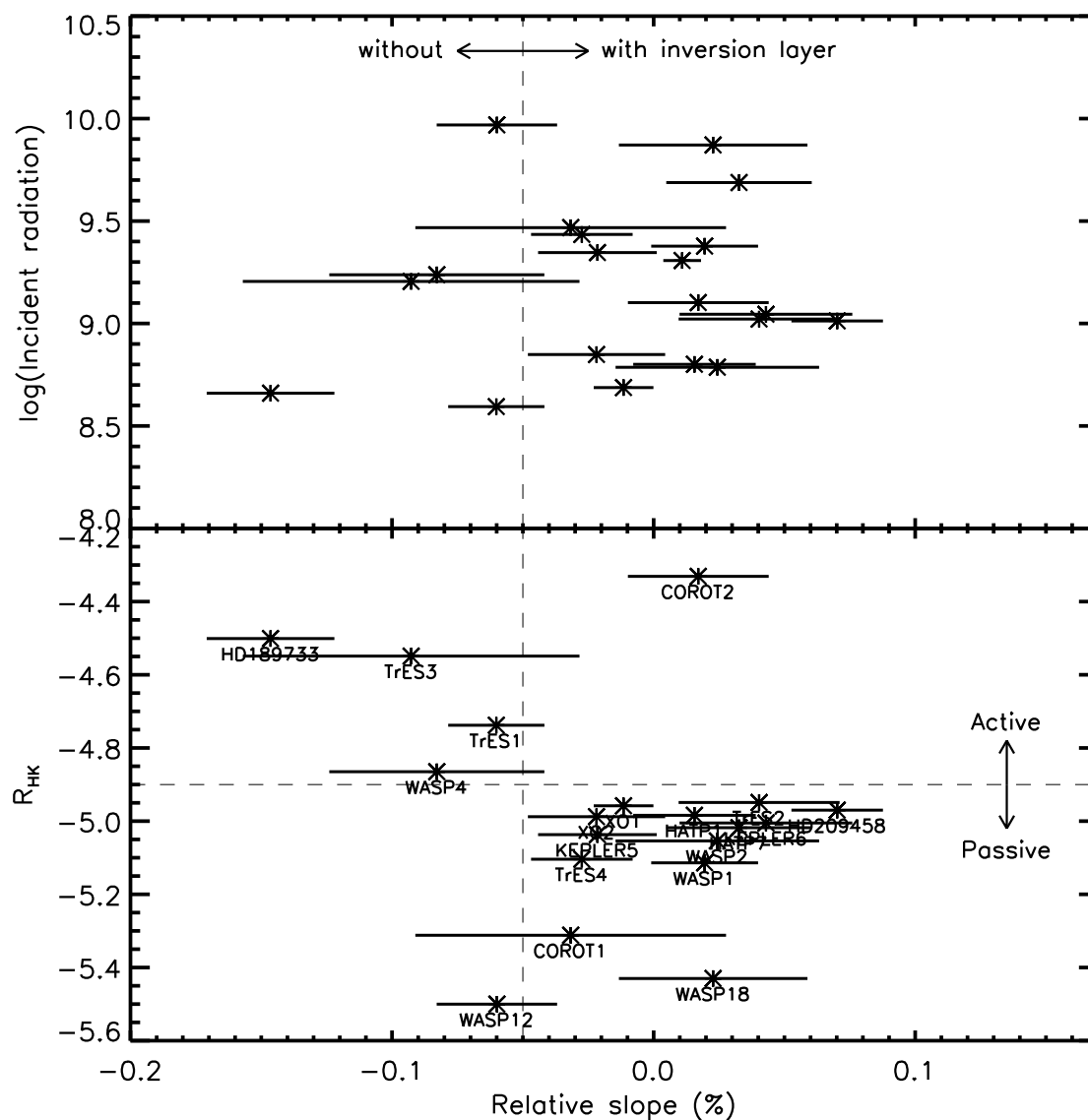


**Figure 6.4** — The slope between the IRAC  $3.6\mu\text{m}$  and  $4.5\mu\text{m}$  eclipse depths relative to that for a black-body, as a function of stellar activity (bottom panel) and incident radiation (top panel). Knutson et al. (2010) take this difference in slope to be a proxy for the presence of an inversion layer, planets with slopes  $> -0.05\%$  are assumed to have an inversion layer, and planets with a smaller slope do not. Stars with  $\log(R_{\text{HK}}) > -4.9$  are considered to be active while stars with  $\log(R_{\text{HK}}) < -4.9$  are considered to be non-active.



**Table 6.4** — Slopes for the linear fits of  $\Delta T(\lambda) \equiv T_b(\lambda) - T_{eq}$  as a function of  $\log(F_{inc})$  and as a function of  $\log(R_{HK})$ .

Band	$\lambda_c$ ( $\mu\text{m}$ )	$dT/d\log(F_{inc})$ (K)	$dT/d\log(R_{HK})$ (K)
Optical	0.6	$-200 \pm 157$	$109 \pm 133$
$K_s$	2.1	$5 \pm 157$	$-344 \pm 117$
IRAC 1	3.6	$-8 \pm 122$	$42 \pm 155$
IRAC 2	4.5	$-37 \pm 151$	$0 \pm 165$
IRAC 3	5.8	$268 \pm 104$	$-543 \pm 145$
IRAC 4	8.0	$285 \pm 98$	$-435 \pm 231$

**Table 6.5** — Intrinsic scatter in  $\Delta T_\lambda$  for the current measurements of hot-Jupiters. The first column gives the bandpass, the second column gives the intrinsic scatter for the entire sample. Columns 3 and 4 give the intrinsic scatter for the subsamples at high ( $\log(F_{inc}) > 9.2$ , 'hot') and low ( $\log(F_{inc}) < 9.2$ , 'cool') levels of irradiation, and columns 5 and 6 give the intrinsic scatter for planets around active ( $\log(R_{HK}) > -4.9$ ) and quiet stars ( $\log(R_{HK}) < -4.9$ ).

Bandpass	$\sigma_{\Delta T_\lambda}$ (K)				
	Average	Hot	Cool	Active	Quiet
Optical	199	409	199	199	199
$K_s$	224	671	554	616	72
IRAC 3.6 $\mu\text{m}$	166	193	145	138	175
IRAC 4.5 $\mu\text{m}$	173	201	137	170	178
IRAC 5.8 $\mu\text{m}$	237	280	195	161	220
IRAC 8.0 $\mu\text{m}$	342	452	142	123	361

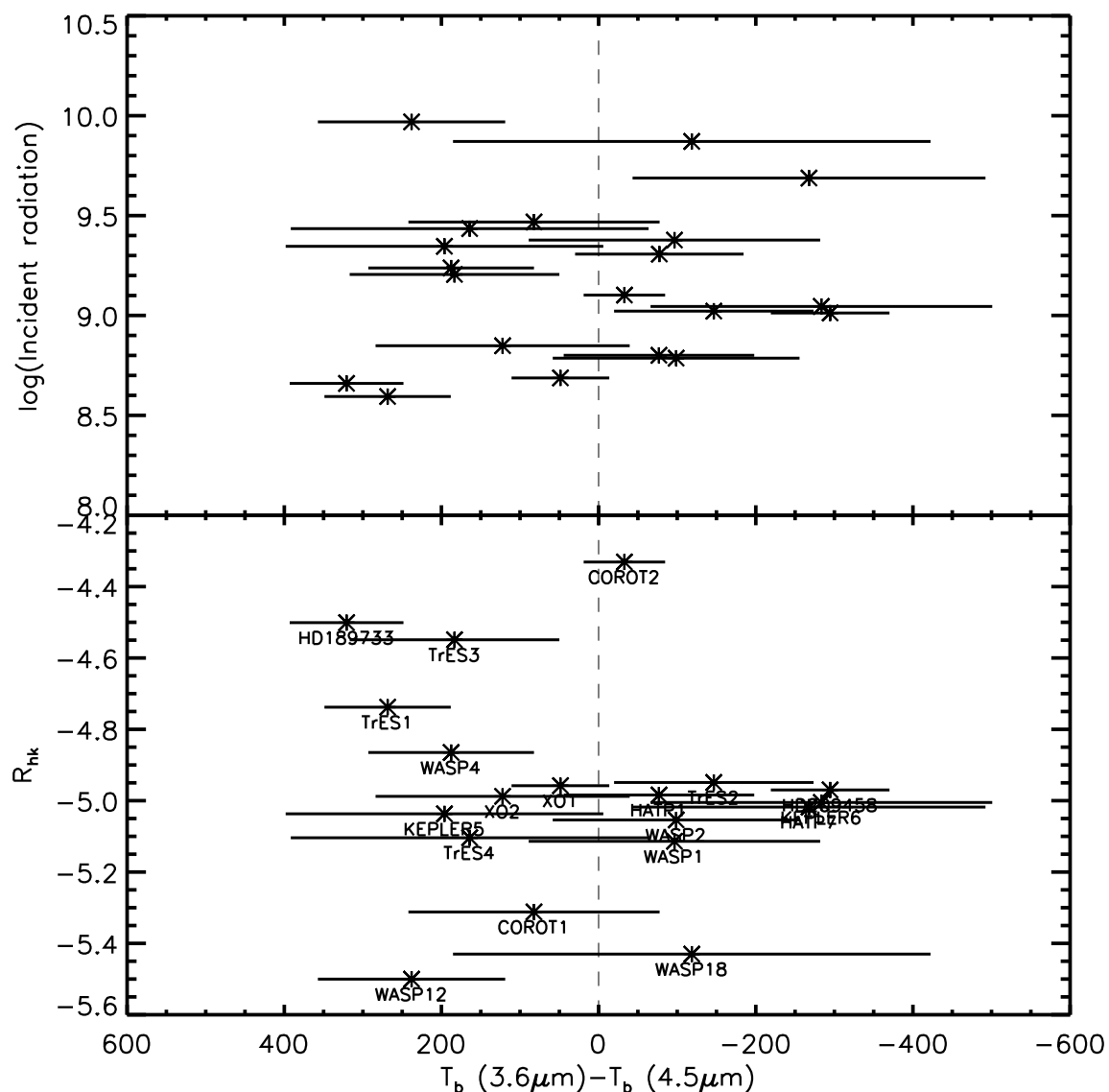


**Figure 6.5** — The difference in brightness temperature between the IRAC  $3.6\mu\text{m}$  and  $4.5\mu\text{m}$  bands as a function of stellar activity (bottom panel) and incident radiation (top panel).

et al. 2011). The optical eclipse depth measurement by Snellen et al. (2010) implies a non inverted atmosphere, such that the optical flux arises deeper in the planet's atmosphere, where the temperature is higher.

However, the diagnostic used by Knutson et al. (2010) is based on the eclipse depth, and therefore, in addition to the planet's emission spectrum, also depends on the flux from the star and the planet-to-star radius ratio. A more physical measurement of the planet's emission spectrum is the difference in brightness temperature between the two bands. We show the relation between this difference in brightness temperature and both incident radiation and stellar activity in the top and bottom panels of Fig. 6.5 respectively. The separation in the difference in brightness temperature as a function of stellar activity has become less obvious, however, we still see

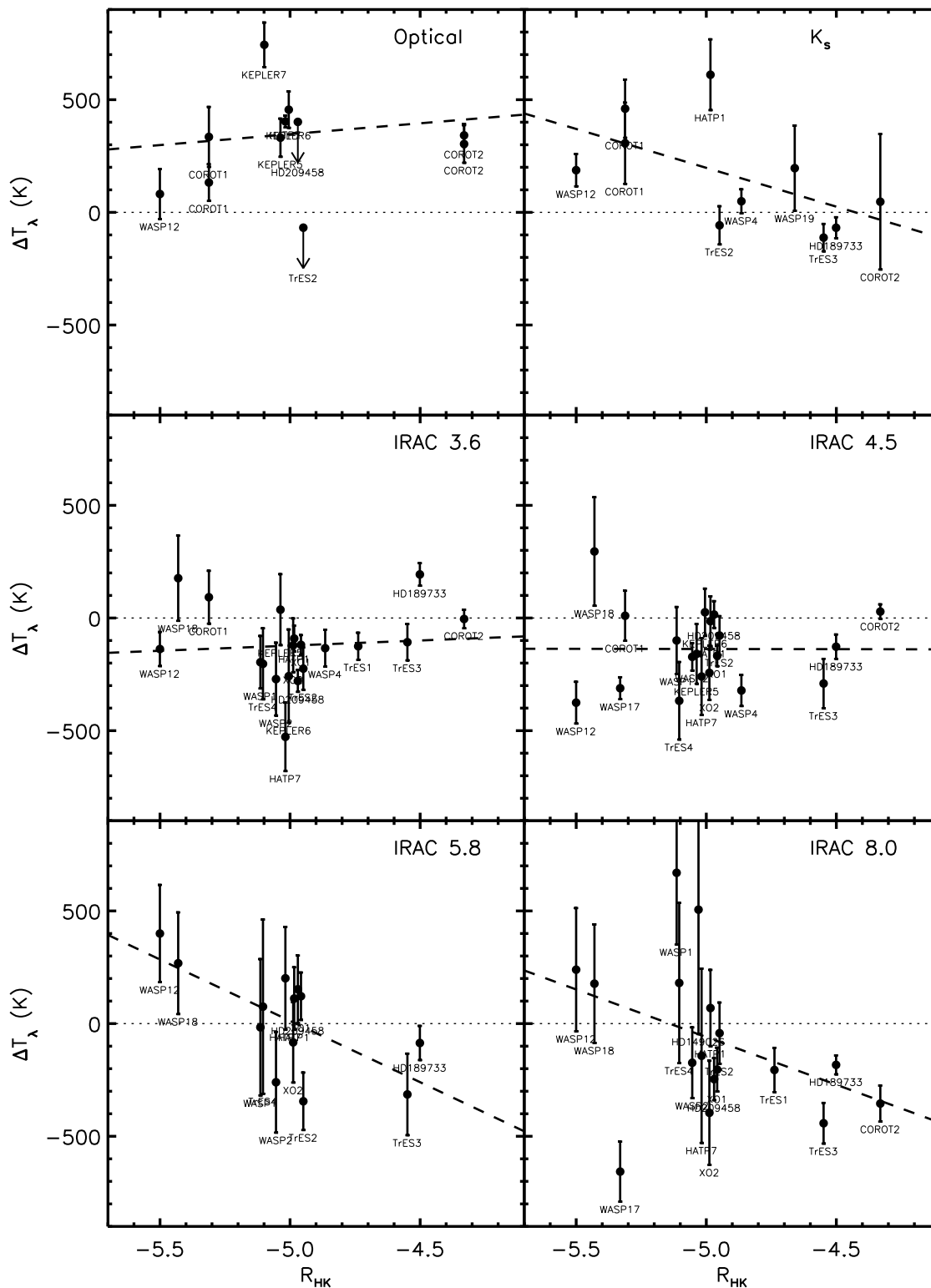


**Figure 6.6** —  $\Delta T_\lambda$  as a function of the stellar variability measurement,  $\log(R_{HK})$ , from Knutson et al. (2010) for the six bands used in this paper. The dashed line shows the best linear fit to  $\Delta T_\lambda$  as a function of  $\log(R_{HK})$ .

that planets with an inversion layer, as inferred by Madhusudhan & Seager (2010) (HD209458b and HAT-P-7b) have a higher brightness temperature in the IRAC 4.5 $\mu\text{m}$  band than in the IRAC 3.6 $\mu\text{m}$  band, while for planets without an inversion layer (HD189733b, TrES-1b, TrES-3b and WASP-4b) the difference in brightness temperature is opposite.

In Fig. 6.6 we show the relation between the stellar activity ( $\log(R_{HK})$  from Knutson et al. 2010)) and  $\Delta T_\lambda$ . We investigated possible relations between  $\Delta T_\lambda$  and stellar activity in the same way as for the incident radiation. The results for this analysis are also given in Table 6.4. The IRAC 5.8 $\mu\text{m}$  and 8.0 $\mu\text{m}$  show a clear trend toward a lower  $\Delta T_\lambda$  for a higher level of stellar activity. Also the  $K_s$ -band shows a significant trend with stellar activity,

## 6.4 The average emission spectrum of a hot Jupiter

A different way of studying the ensemble of day-side spectra of hot Jupiters is by constructing an average emission spectrum, based on the  $\Delta T_\lambda$  in each wave band, both for the sample as a whole, as well as for subsamples of planets with high and low incident radiation and those orbiting quiet and active stars. To create the emission spectra, the mean,  $\langle \Delta T_\lambda \rangle$ , was determined for each of the bands. The resultant spectrum for the whole sample is shown in Fig. 6.7. The uncertainty on the  $\langle \Delta T_\lambda \rangle$  in each of the wavelength bands was determined from the scatter in  $\Delta T_\lambda$  in that band divided by square-root of the number of points. By taking the mean without using different weights for each of the planets based on the measurement uncertainty, we prevent individual planets from dominating the average spectrum.

Although in most bands the trends between  $\Delta T_\lambda$  and the incident radiation, as found in Sect. 6.3, are weak, we also separated the observations in a 'hot' subsample, containing planets with an incident radiation of more than  $1.6 \cdot 10^9 \text{ erg cm}^{-2} \text{ sec}^{-1}$ , and a 'cool' subsample, which consists of planets with an incident radiation lower than  $1.6 \cdot 10^9 \text{ erg cm}^{-2} \text{ sec}^{-1}$ . This value was chosen since it is at about the median for the entire sample. The mean of  $\Delta T_\lambda$  and the associated uncertainties were determined in the same way as for the average spectrum for the whole sample. The resultant spectra are also shown in Fig. 6.7. As can be clearly seen, the  $K_s$ -band measurements for both subsamples are hotter than the equilibrium temperature, while the IRAC measurements at 3.6, 4.5 and 8.0 $\mu\text{m}$  are at lower brightness temperatures for both subsamples. At 5.8 $\mu\text{m}$  the brightness temperature is at, or slightly below, that expected for the equilibrium temperature. For the 'cool' subsample of planets, the variation in the brightness temperatures in the four IRAC channels is smaller than for the hot subsample of planets.

We also divided the sample into planets orbiting active stars and quiet stars. All stars with  $\log(R_{HK}) > -4.9$  are considered to be active, while all stars with  $\log(R_{HK}) < -4.9$  are considered to be quiet. The resultant spectra for both the subsamples are shown in Fig. 6.8. The differences between the two subsamples are evident. For planets around the active stars  $\langle \Delta T_\lambda \rangle < 0$  in all bands, except at optical wavelengths, while the planets in the quiet subsample show a strongly modulated spectrum, with the  $\langle \Delta T_\lambda \rangle < 0$  in the IRAC 3.6 $\mu\text{m}$  and 4.5 $\mu\text{m}$  bands, but  $\langle \Delta T_\lambda \rangle > 0$  in all other bandpasses.

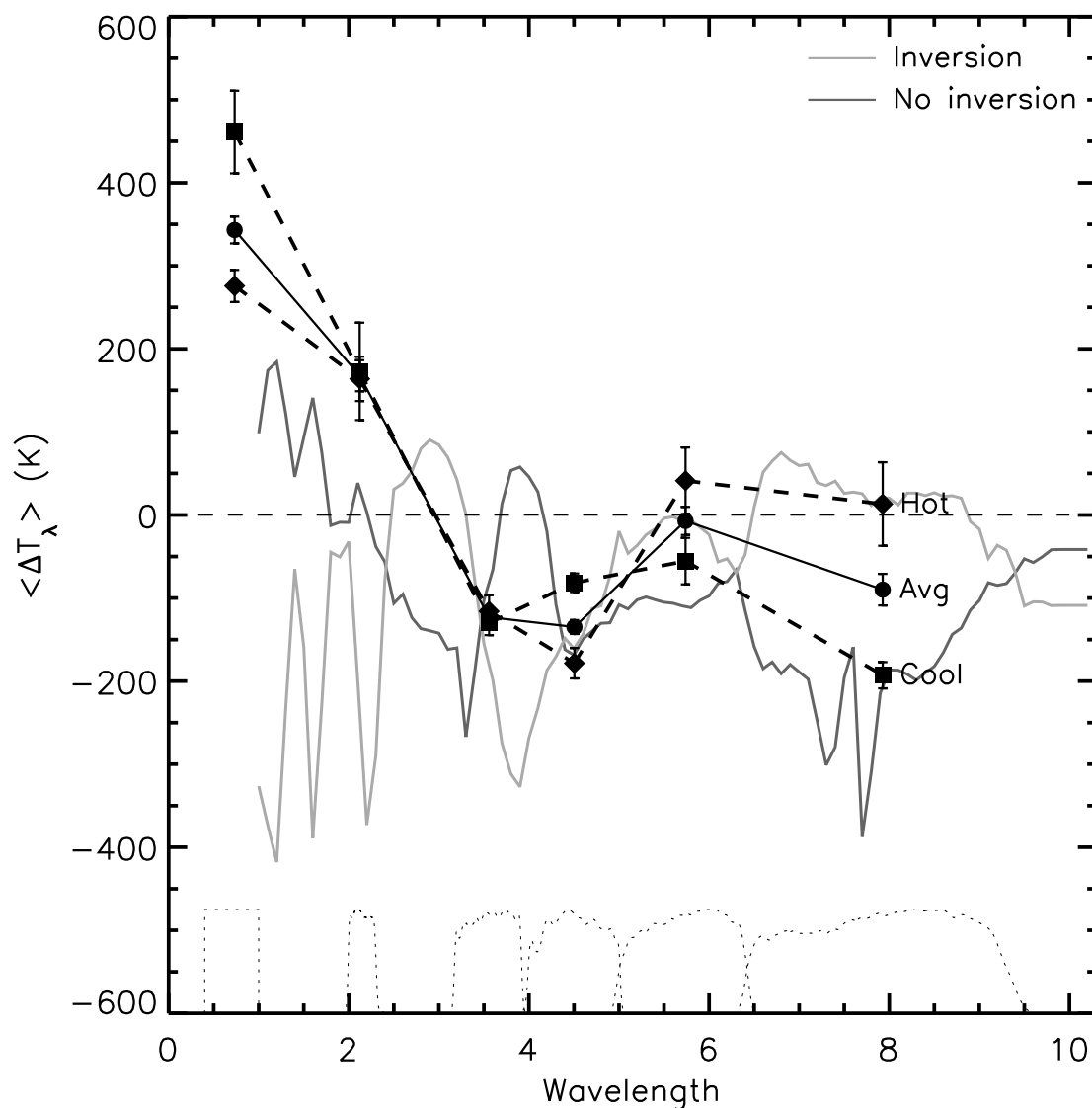


**Figure 6.7** — The average emission spectrum of the hot Jupiter in our sample in terms of  $\langle \Delta T_\lambda \rangle$ . The filled circles (connected by the solid black line) are the averages for the entire sample, while the filled diamonds and squares (connected by dashed lines) are for the planets with  $F_{\text{inc}} > 1.6 \cdot 10^9 \text{ erg cm}^{-2} \text{ sec}^{-1}$  and  $F_{\text{inc}} < 1.6 \cdot 10^9 \text{ erg sec}^{-1} \text{ cm}^2$  respectively (the 'hot' and 'cool' bins). Note that for clarity we have slightly offsetted the points in each of the bands in wavelength. Overplotted are two atmospheric models, one with an inversion layer (solid light grey line) and one without a thermal inversion (solid dark grey line) that provide the best fit to the 'cool' and the 'hot' samples respectively. The dashed lines in the bottom of the figure show the different filter-curves.

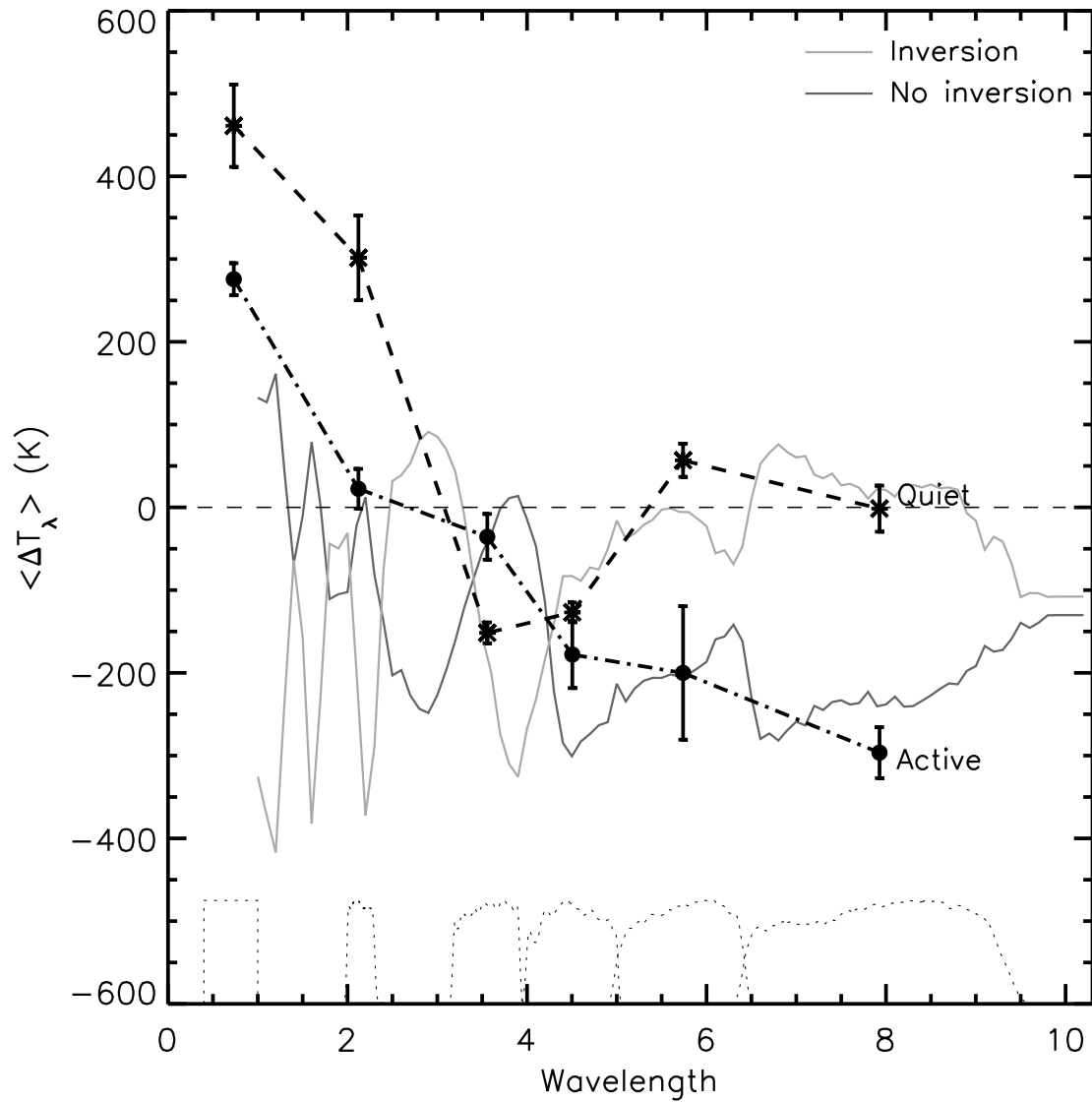


**Figure 6.8** — Same as Fig. 6.7, but now for subsamples of planets orbiting quiet stars with  $\log(R_{HK}) < -4.9$  (stars connected with dashed line) and active stars with  $\log(R_{HK}) > -4.9$  (filled circles connected by a dashed-dotted line). Overplotted are two atmospheric models, one with an inversion layer (light grey line) and one without a thermal inversion (dark grey line) that provide the best fit to the planets around quiet and active stars respectively. The dashed lines in the bottom of the figure show the different filter-curves.

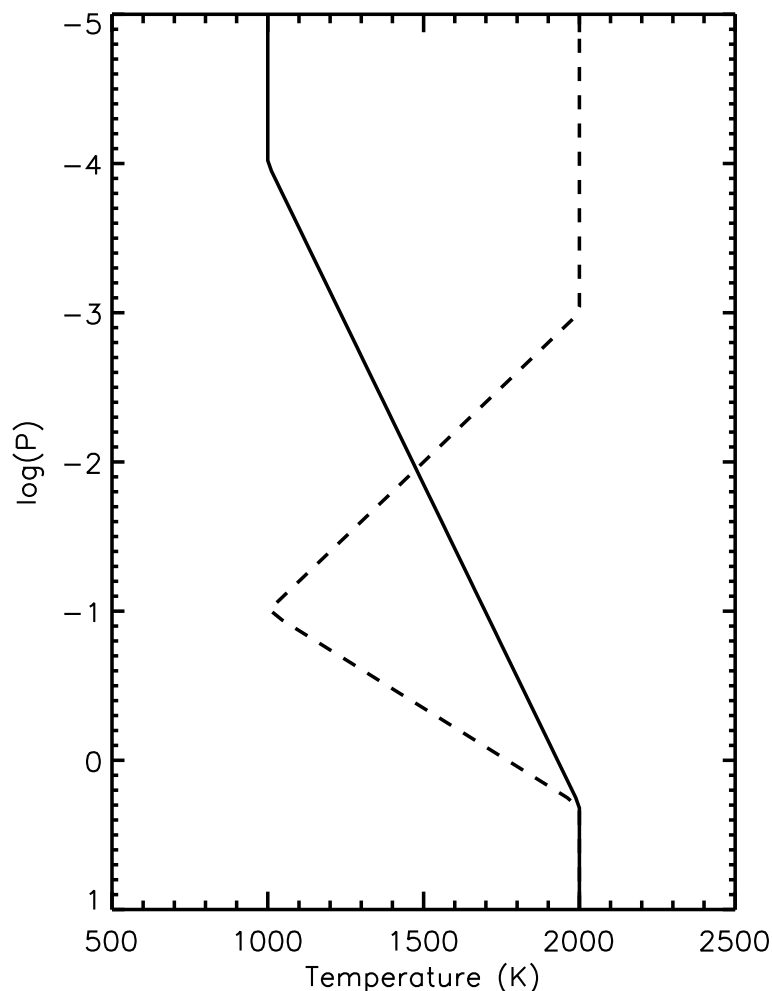


**Figure 6.9** — Example of two different temperature-pressure profiles used for the atmospheric models. A description of the parameters that were varied (also indicated in this figure), are given in Sect. 6.5. The solid line is for a non-inverted model, while the dashed line is for a model with an inversion layer.

## 6.5 Atmosphere models

It is clear from the average spectra for the different subsamples, as shown in Figs. 6.7 and 6.8, that the observations are inconsistent with a simple blackbody model, which has a single brightness temperature across all the bands. We therefore generated a set of atmospheric models to compare with, using the code developed by De Kok. This code has also been used to generate the models in Chapter 3. Since our opacity database at optical wavelengths is still incomplete, and since the optical measurements can be strongly influenced by reflected light anyway, we opted to only generate models between 1 and  $10\mu\text{m}$ . To efficiently calculate the spectra, the correlated-k method (Lacis & Oinas 1991) was used, in which the absorption properties of the gases are calculated for a large range of temperatures and pressures before generating the individual spectra. The spectra themselves are  $0.1\mu\text{m}$  at longer wavelengths. The opacity data for  $\text{H}_2\text{O}$ ,  $\text{CO}$  and  $\text{CO}_2$  are taken from the HITEMP database (Rothman et al. 2010), while the

opacities of CH<sub>4</sub> come from the HITRAN database (Rothman et al. 2009).

The atmospheric models are not generated using a self-consistent method, which balances the incoming flux and the outgoing radiation. Instead we assumed a set of temperature-pressure profiles, both with and without an inversion layer to calculate the emission spectrum as shown in Fig. 6.9. For the non-inverted models, the T-P profile was chosen such that the difference between the temperature at the base of the atmosphere (taken to be 2 bar) and the top of the troposphere (at a pressure of 10<sup>-4</sup> bars) is 1000 K. Below 2 bar and above 10<sup>-4</sup> bar the temperature was assumed to be constant. For the inverted models the difference in temperature between the base of the atmosphere (again at 2 bar) and the bottom of the inversion layer was taken to be 1000 K, while in the inversion layer the temperature increased again with 1000 K until a pressure of 10<sup>-3</sup> bar, above which the temperature was again assumed constant. For both the models with and without an inversion layer we use a wide range of volume mixing ratios (VMR) for CO, CH<sub>4</sub>, H<sub>2</sub>O and CO<sub>2</sub>, with steps of  $\Delta\log(\text{VMR})=0.5$ . For CO and H<sub>2</sub>O we used six different VMRs starting at  $\log(\text{VMR})=-5.5$ , while for H<sub>2</sub>O and CO<sub>2</sub> we used ten different VMRS, starting at  $\log(\text{VMR})=-8.5$ .

To compare these sets of models to the data, we integrate the fluxes over the different pass-bands, and convert these fluxes into brightness temperatures. We also calculate the effective temperatures of the models by integrating the fluxes over the entire wavelength range of the models, and comparing the resultant flux to the fluxes of a grid of blackbodies as a function of temperature, which was subsequently subtracted from the brightness temperatures. However, since the effective temperature is a measure of the total energy radiated by the planet, it can not be compared directly to the equilibrium temperature, which is a measure of the level of incident stellar radiation. Since the average spectra were determined using  $T_{\text{eq}}$ , we therefore determined the average offset between  $\langle \Delta T_{\lambda} \rangle$  of the (sub)samples and those of the model using only the four IRAC bands. This offset was then taken into account in the fitting, which was done using a  $\chi^2$  analysis. For almost all the subsamples, we found that the reduced  $\chi^2$  for the best-fit model was much larger than unity. On closer inspection of the models, it appears that this is due to the fact that most of the subsamples show a higher brightness temperature in the K<sub>s</sub>-band when compared to the brightness temperatures in the *Spitzer* IRAC channels, something that is not seen in the models. Since we only use two temperature-pressure profiles, it is likely that using different temperature-pressure profiles could help solve this problem.

Since all models seem to provide a bad match to the data in the K<sub>s</sub>-band, we also refitted the spectra of the different (sub)samples using just the four IRAC channels. Although the reduced  $\chi^2$  is still larger than unity for two of the five subsamples, the reduced  $\chi^2$  are now much improved. Qualitatively, the best fitting models for the ‘hot’ and ‘quiet’ subsamples are models with an inversion layer, while the ‘cool’ and ‘active’ subsamples are better described by models without an inversion layer.

Examples of models with and without an inversion layer are shown in Figs. 6.7 and 6.8. The models shown in Fig. 6.7 provide the best fit to the ‘cool’ and ‘hot’ samples, while the models shown in Fig. 6.8 provide the best fit to the active and quiet samples.



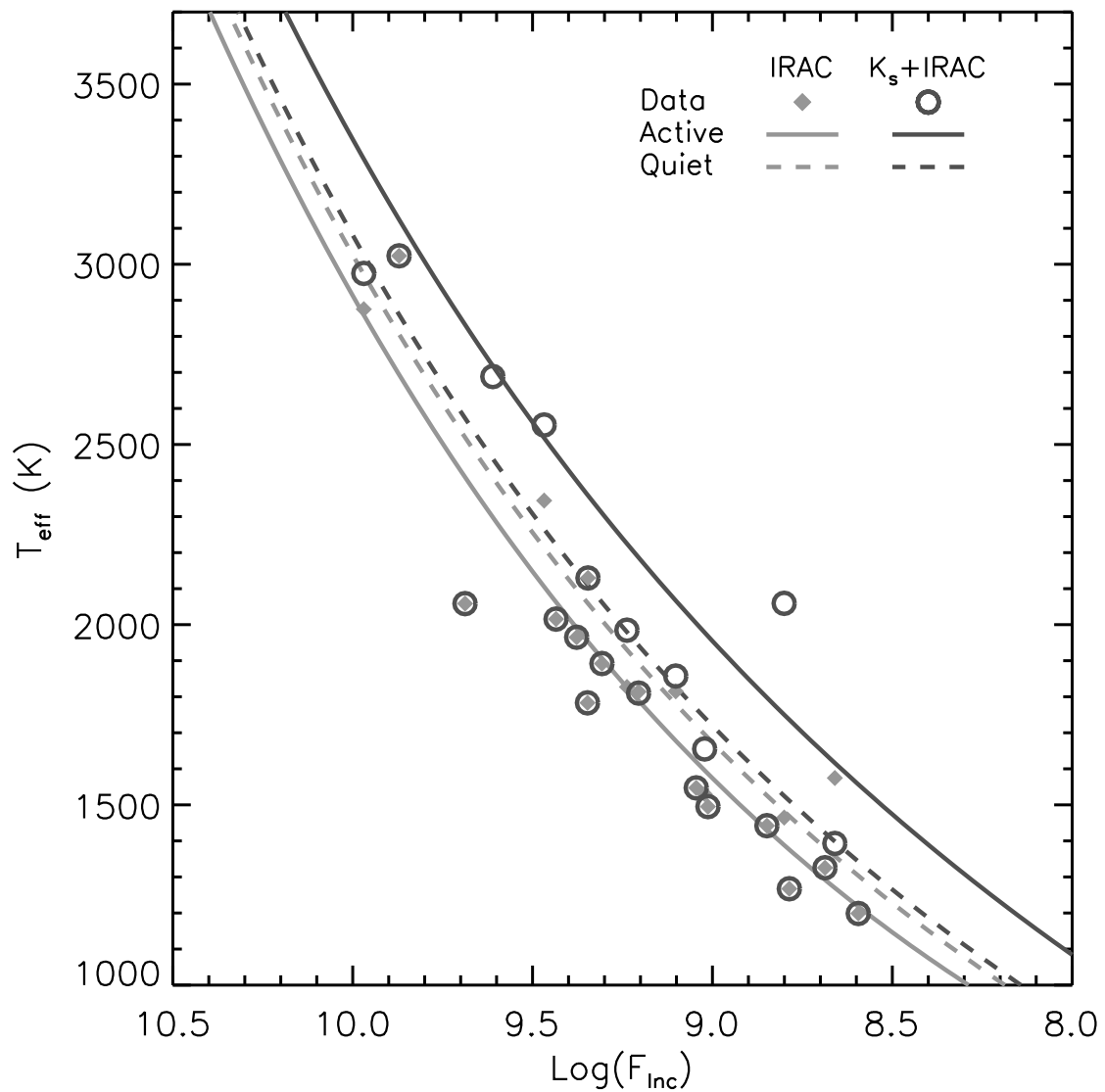


**Figure 6.10** — The effective temperatures for the planets in our sample, calculated using the linear interpolation technique from Cowan & Agol (2011), as a function of the incident radiation. The open circles and filled diamonds are for the  $T_{\text{eff}}$  determined with and without observations in the  $K_s$ -bands respectively. The dark and light grey lines show the effective temperature as a function of incident radiation determined from the average spectra when the  $K_s$ -band is included and excluded respectively. The solid lines show the effective temperature for the quiet stars, while the dashed lines show the effective temperature for the active stars.

## 6.6 Discussion

### 6.6.1 The effective temperatures of hot Jupiters

In addition to brightness temperatures, we also constructed a “bolometric” emission spectrum for all the objects in our sample which we converted into an effective temperature. The effective temperature is determined by the energy budget on the planet’s day-side, which is governed by the incident radiation, the Bond albedo, and the fraction of the energy transported from the planet’s day-side to its night-side. We used the linear interpolation method from Cowan & Agol (2011) to determine the planet’s effective temperature. For each planet a fine grid of brightness temperatures as a function of wavelength was created by linearly interpolating the measured brightness temperatures across the different wavelengths. A constant brightness temperature for wavelengths located outside the range of observations for the planet was used, set to the value of the longest/shortest wavelength point. This grid of brightness temperatures was then converted into fluxes, which were subsequently integrated over wavelength and compared to the fluxes of a blackbody spectrum at different temperatures across the wavelength range. For each planet we determined the effective temperature for different combinations of bandpasses to investigate the impact of using different combinations of bandpasses. Missing bandpasses were interpolated across, if there are observations at longer and shorter wavelengths. We excluded all the planets for which only one bandpass is available. In Fig. 6.10 we plot the effective temperatures determined from the planets brightness temperatures using all the infrared bandpasses (K<sub>s</sub>, IRAC 3.6 $\mu$ m, 4.5 $\mu$ m, 5.8 $\mu$ m and 8.0 $\mu$ m). In addition, we also show the effective temperatures for the planets determined from the four IRAC channels only. The temperatures for some of the planets are seen to vary by a large amount depending on which bands are included. We also show lines for the expected effective temperatures as a function of incident radiation for the average spectra of planets around quiet and active stars, as determined in Sect. 6.4. These effective temperatures were calculated by adding the equilibrium temperature for a given level of incident radiation back to the observed  $\Delta T_\lambda$ , which were subsequently converted to an effective temperature using the method described above. These effective temperatures are overplotted in Fig. 6.10 where the dark and light grey solid lines show the effective temperatures for the planets around the quiet stars when the K<sub>s</sub>-band is included and excluded respectively, while the dark and light grey dashed lines show the same for the planets around active stars with and without all the infrared bands. The much higher brightness temperature in the K<sub>s</sub>-band compared to that in the IRAC 3.6 $\mu$ m band for the quiet stars significantly increases the derived effective temperature when it is included in its determination. The much smaller difference in brightness temperature between these bands for planets around active stars reduces the impact of including or excluding the K<sub>s</sub>-bands.

The large impact on the effective temperature from the K<sub>s</sub>-band is due to the fact that it is located just redward of the peak of the emission spectrum for most hot Jupiters (for the coolest planet in the sample, TrES-1b, the blackbody peak is at  $\sim 2.1\mu$ m, while for the hottest planet in the sample, WASP-33b, the peak is located at 0.9 $\mu$ m), where the bulk of the energy is emitted. Since we use a constant brightness temperature (equal to the brightness temperature at the shortest wavelength used in the fit) for all shorter wavelengths, it gives a very high weight to the brightness temperature in the K<sub>s</sub>-band when it is included. This clearly demonstrates the need for more observations at near-infrared wavelengths, both in the K<sub>s</sub>-band as well as in the

i-, z-, J- and H-bands, in order to constrain the energy budgets of hot Jupiter atmospheres.

Since most planets only have measurements in one or more of the IRAC bands, and since the average  $\Delta T_\lambda$  in the  $K_s$ -band for most subsamples are larger than the  $\Delta T_\lambda$  in the IRAC  $3.6\mu\text{m}$  band, this can have a strong implication for the determination of the albedo and reradiation efficiency of exoplanet atmospheres. However, if we use all five infrared bands to determine the effective temperatures for different subsamples of hot Jupiters, we can estimate the combination of the reradiation efficiency,  $f$ , and the albedo,  $A$ , which are related to the effective temperature and the incident radiation by  $f(1-A)=\sigma T_{\text{eff}}^4/F_{\text{inc}}$ . To calculate these quantities, we use an equilibrium temperature of 1930 K, the median of the sample. For the planets around active stars we derive  $f(1-A)\sim 0.5$  ( $T_{\text{eff}}-T_{\text{eq}}\sim 0$  K), which is consistent with a zero albedo, a homogeneous temperature on the planet's day-side and no redistribution to the planet's night-side. For planets orbiting quiet stars, we find  $f(1-A)\sim 0.8$  ( $T_{\text{eff}}-T_{\text{eq}}\sim 250$  K), which would require all the incident stellar radiation to be absorbed on the day-side, and immediately reradiated again. For the subsamples divided into the two bins of incident stellar radiation as well as for the average of the whole sample we find an intermediate  $f(1-A)\sim 0.65$  ( $T_{\text{eff}}-T_{\text{eq}}\sim 125$  K).

If we use only the IRAC bands for the determination of the effective temperatures and subsequently also the reradiation efficiencies for the different subsamples, we find that  $f(1-A)$  is around 0.45 ( $T_{\text{eff}}-T_{\text{eq}}\sim -45$  K) for the planets around active stars, while in all other cases  $f(1-A)\sim 0.35$  to 0.38 ( $T_{\text{eff}}-T_{\text{eq}}\sim -150$  to  $-120$  K). This offers a contrasting view to the results found above, since the lower value of  $f(1-A)$  allows for a lower  $f$ , which would mean that more energy is advected to the night-side, or that they have a higher albedo, causing a lower fraction of the incident stellar radiation to be absorbed. This again demonstrates that it is vital to get more observations in the near-infrared to probe the planets' spectral energy distributions at and around their maximum, in order to put better constraints on their albedos and reradiation efficiencies.

We can compare these results to Cowan & Agol (2011), who find that on average the planets have a Bond-albedo consistent with zero, but that the planets span a wide range of reradiation efficiencies. However, as we have demonstrated above, the linear-interpolation technique can be very sensitive to the inclusion of bands near the peak of the spectral energy distribution, depending on the detailed shape of the planet's spectrum, and one must therefore be cautious when applying it to real data.

## 6.6.2 Stellar activity and the presence of an inversion layer

From the average spectra in terms of  $\Delta T_\lambda$  of the four sub-samples, we find that the largest difference is seen when comparing the spectrum for the planets around active stars with that for planets around quiet stars. This result is similar to that by Knutson et al. (2010), who found that planets around active stars show a different behaviour in the slope between the IRAC  $3.6\mu\text{m}$  and  $4.5\mu\text{m}$  channels from planets around quiet stars. For the planets around active stars we find a steady decline in the brightness temperature across all bands, which is best fit with a model without an inversion layer, while for the planets around quiet stars we see a strong modulation in the spectrum, with the emission in the IRAC  $3.6\mu\text{m}$  and  $4.5\mu\text{m}$  bands arising from a cooler layer in the planet's atmosphere than the emission in the IRAC  $5.8\mu\text{m}$  and  $8.0\mu\text{m}$  bands, which can be best fit with a model with an inversion layer. Knutson et al. (2010) suggest that the stellar activity for the active stars could be responsible for the destruction of the compound

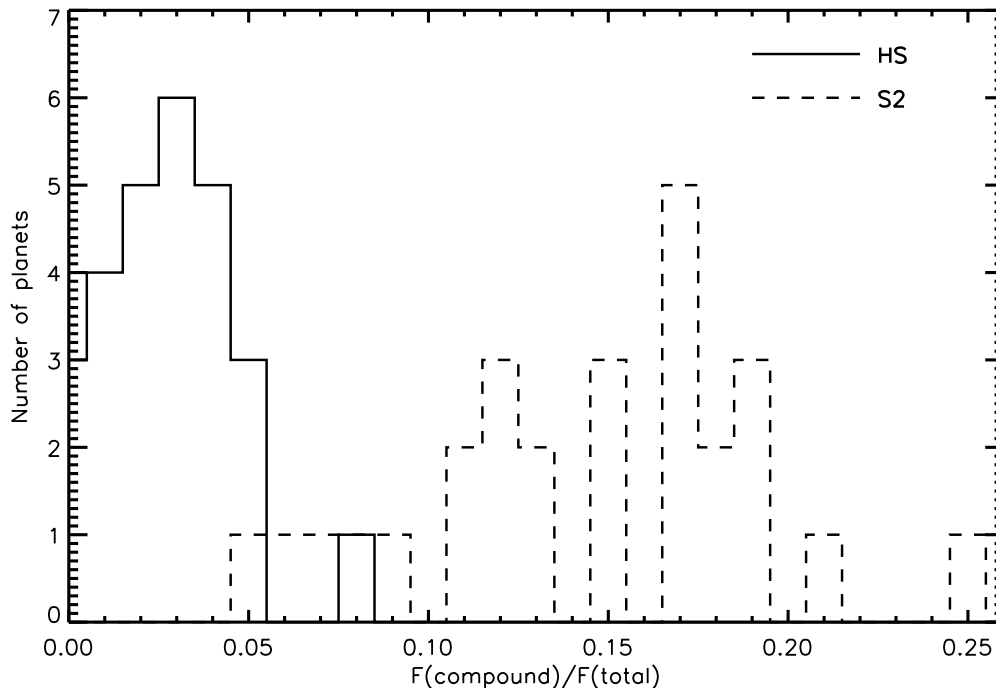


**Figure 6.11** — Histograms of the fraction of the incident stellar flux that can be absorbed by HS (dashed line) and  $S_2$  (solid line).

responsible for the inversion layer due to an increase in the UV-flux. A possible compound could be sulphur based compounds such as  $S_2$  and HS studied by Zahnle et al. (2009), which could be quite abundant in planetary atmospheres. While  $S_2$  absorbs efficiently in the near-UV, between  $0.24\mu\text{m}$  and  $0.34\mu\text{m}$  (Zahnle et al. 2009), HS has a significant opacity at slightly redder wavelengths, between  $\sim 0.3\mu\text{m}$  and  $0.46\mu\text{m}$ .

To investigate what fraction of the incident stellar radiation can be absorbed by the different compounds, we made a simple model. We assume that all the incident stellar radiation within the wavelength ranges given above is absorbed by the compound, and compare that to the total incident radiation. We ignore possible absorption by the compounds at wavelengths shortward of  $2400\text{ \AA}$ , since the integrated stellar flux at those wavelengths is less than 1% of the bolometric flux for most stars.

Since the host-stars of the currently known hot Jupiters span effective temperatures from  $\sim 4800\text{ K}$  to  $\sim 7500\text{ K}$ , the fraction of the total stellar flux that can be absorbed by the different compounds can vary greatly. In Fig. 6.11 we show the distribution of the fraction of the total flux that can be absorbed by the different compounds,  $F_{\text{compound}}/F_{\text{tot}}$ , for  $S_2$  and HS. It is clear that  $S_2$ , with large opacities in a narrow range in the blue part of the optical spectrum is unable to absorb a significant fraction of the incident radiation with the largest fraction, for WASP-33b, of less than 10%. HS on the other hand, appears to be a better candidate, with the ability to absorb up to  $\sim 25\%$  of the incoming radiation. In contrast the large opacity range offered by TiO and VO, which also coincides with the peak of the stellar SED, allows about 50% of the incident stellar radiation to be absorbed in the inversion layer. This should give rise to a stronger inversion layer.

## 6.7 Conclusion

The emission properties of a large sample of hot Jupiters are investigated using data from the literature. The properties are studied as a function of the planet's environment, in particular with respect to the level of incident radiation and the stellar activity. In addition, the average emission spectrum of a hot Jupiter is determined, both for the entire sample, as well as for subsamples based on the incident radiation, and on the stellar activity. Our main conclusion are as follows:

1. We confirm that the mean day-side spectrum of a hot Jupiter significantly deviates from that of a blackbody: at optical and near-infrared wavelengths the brightness temperatures are higher, whereas they are lower at 3.5 and 4.5  $\mu\text{m}$  than expected from their equilibrium temperatures.
2. The mean variations in brightness temperature as a function of wavelength are significantly different for planets orbiting active stars than for those orbiting quiet stars. These differences in brightness temperature variations are much smaller between samples of planets at low and high levels of irradiation.
3. From comparison of their overall spectral energy distribution with their theoretical equilibrium temperatures, planets around quiet stars have, on average, a higher reradiation efficiency and lower albedo than planets orbiting active stars. These differences are again much smaller for high and lower irradiated planets. However, the determination of the planet effective temperatures are hampered by the limited availability of eclipse measurements in the near-infrared, where hot Jupiters peak in their spectral energy distribution.
4. Qualitatively, the mean emission spectrum of planets orbiting quiet stars appears to be consistent with models with an atmospheric inversion layer, while the average spectrum of planets orbiting active stars is consistent with atmospheric models without such thermal inversion.

## Bibliography

- Agol, E., Cowan, N. B., Knutson, H. A., et al. 2010, *ApJ*, 721, 1861
- Alonso, R., Alapini, A., Aigrain, S., et al. 2009a, *A&A*, 506, 353
- Alonso, R., Auvergne, M., Baglin, A., et al. 2008, *A&A*, 482, L21
- Alonso, R., Deeg, H. J., Kabath, P., & Rabus, M. 2010, *AJ*, 139, 1481
- Alonso, R., Guillot, T., Mazeh, T., et al. 2009b, *A&A*, 501, L23
- Anderson, D. R., Smith, A. M. S., Lanotte, A. A., et al. 2011, ArXiv:1101.5620 [astro-ph.EP]
- Auvergne, M., Bodin, P., Boisnard, L., et al. 2009, *A&A*, 506, 411
- Barge, P., Baglin, A., Auvergne, M., et al. 2008, *A&A*, 482, L17
- Beerer, I. M., Knutson, H. A., Burrows, A., et al. 2011, *ApJ*, 727, 23
- Borucki, W. J., Koch, D., Jenkins, J., et al. 2009, *Science*, 325, 709
- Burrows, A., Budaj, J., & Hubeny, I. 2008, *ApJ*, 678, 1436
- Caceres, C., Ivanov, V. D., Minniti, D., et al. 2011, ArXiv:1104.0041 [astro-ph.EP]
- Campo, C. J., Harrington, J., Hardy, R. A., et al. 2011, *ApJ*, 727, 125
- Chan, T., Ingemyr, M., Winn, J. N., et al. 2011, ArXiv:1103.3078 [astro-ph.EP]
- Charbonneau, D., Allen, L. E., Megeath, S. T., et al. 2005, *ApJ*, 626, 523
- Charbonneau, D., Knutson, H. A., Barman, T., et al. 2008, *ApJ*, 686, 1341
- Christiansen, J. L., Ballard, S., Charbonneau, D., et al. 2010, *ApJ*, 710, 97
- Collier Cameron, A., Bruce, V. A., Miller, G. R. M., Triaud, A. H. M. J., & Queloz, D. 2010, *MNRAS*, 403, 151
- Cowan, N. B. & Agol, E. 2011, *ApJ*, 729, 54
- Croll, B., Albert, L., Lafrenière, D., Jayawardhana, R., & Fortney, J. J. 2010a, *ApJ*, 717, 1084
- Croll, B., Jayawardhana, R., Fortney, J. J., Lafrenière, D., & Albert, L. 2010b, *ApJ*, 718, 920
- Croll, B., Lafrenière, D., Albert, L., et al. 2011, *AJ*, 141, 30
- Deming, D., Knutson, H., Agol, E., et al. 2011, *ApJ*, 726, 95
- Deming, D., Seager, S., Richardson, L. J., & Harrington, J. 2005, *Nature*, 434, 740
- Desert, J., Charbonneau, D., Fortney, J. J., et al. 2011, ArXiv:1102.0555 [astro-ph.EP]
- Fortney, J. J., Lodders, K., Marley, M. S., & Freedman, R. S. 2008, *ApJ*, 678, 1419
- Fressin, F., Knutson, H. A., Charbonneau, D., et al. 2010, *ApJ*, 711, 374
- Gibson, N. P., Aigrain, S., Pollacco, D. L., et al. 2010, *MNRAS*, 404, L114
- Gillon, M., Demory, B., Triaud, A. H. M. J., et al. 2009, *A&A*, 506, 359
- Gillon, M., Lanotte, A. A., Barman, T., et al. 2010, *A&A*, 511, A3+
- Harrington, J., Luszcz, S., Seager, S., Deming, D., & Richardson, L. J. 2007, *Nature*, 447, 691
- Hauschildt, P. H., Allard, F., Ferguson, J., Baron, E., & Alexander, D. R. 1999, *ApJ*, 525, 871
- Hebb, L., Collier-Cameron, A., Triaud, A. H. M. J., et al. 2010, *ApJ*, 708, 224
- Hellier, C., Anderson, D. R., Collier-Cameron, A., et al. 2011, *ApJ*, 730, L31+
- Kipping, D. & Bakos, G. 2011a, *ApJ*, 730, 50
- Kipping, D. & Bakos, G. 2011b, *ApJ*, 730, 50
- Kipping, D. M. & Bakos, G. Á. 2010, ArXiv:1006.5680 [astro-ph.EP]
- Knutson, H. A., Charbonneau, D., Allen, L. E., Burrows, A., & Megeath, S. T. 2008, *ApJ*, 673, 526
- Knutson, H. A., Charbonneau, D., Allen, L. E., et al. 2007, *Nature*, 447, 183
- Knutson, H. A., Charbonneau, D., Burrows, A., O'Donovan, F. T., & Mandushev, G. 2009a, *ApJ*, 691, 866

- Knutson, H. A., Charbonneau, D., Cowan, N. B., et al. 2009b, *ApJ*, 703, 769
- Knutson, H. A., Charbonneau, D., Cowan, N. B., et al. 2009c, *ApJ*, 690, 822
- Knutson, H. A., Howard, A. W., & Isaacson, H. 2010, *ApJ*, 720, 1569
- Lacis, A. A. & Oinas, V. 1991, *J. Geophys. Res.*, 96, 9027
- López-Morales, M., Coughlin, J. L., Sing, D. K., et al. 2010, *ApJ*, 716, L36
- Machalek, P., Greene, T., McCullough, P. R., et al. 2010, *ApJ*, 711, 111
- Machalek, P., McCullough, P. R., Burke, C. J., et al. 2008, *ApJ*, 684, 1427
- Machalek, P., McCullough, P. R., Burrows, A., et al. 2009, *ApJ*, 701, 514
- Madhusudhan, N. & Seager, S. 2010, *ApJ*, 725, 261
- Nymeyer, S., Harrington, J., Hardy, R. A., et al. 2010, ArXiv:1005.1017 [astro-ph.EP]
- O'Donovan, F. T., Charbonneau, D., Harrington, J., et al. 2010, *ApJ*, 710, 1551
- Pál, A., Bakos, G. Á., Torres, G., et al. 2008, *ApJ*, 680, 1450
- Rogers, J. C., Apai, D., López-Morales, M., Sing, D. K., & Burrows, A. 2009, *ApJ*, 707, 1707
- Rothman, L. S., Gordon, I. E., Barbe, A., et al. 2009, *J. Quant. Spec. Radiat. Transf.*, 110, 533
- Rothman, L. S., Gordon, I. E., Barber, R. J., et al. 2010, *J. Quant. Spec. Radiat. Transf.*, 111, 2139
- Rowe, J. F., Matthews, J. M., Seager, S., et al. 2008, *ApJ*, 689, 1345
- Sing, D. K. & López-Morales, M. 2009, *A&A*, 493, L31
- Smith, A. M. S., Anderson, D. R., Skillen, I., Collier Cameron, A., & Smalley, B. 2011, ArXiv:1101.2432v2 [astro-ph.EP]
- Snellen, I. A. G. & Covino, E. 2007, *MNRAS*, 375, 307
- Snellen, I. A. G., de Mooij, E. J. W., & Albrecht, S. 2009, *Nature*, 459, 543
- Snellen, I. A. G., de Mooij, E. J. W., & Burrows, A. 2010, *A&A*, 513, A76+
- Southworth, J. 2010, *MNRAS*, 408, 1689
- Swain, M. R., Vasisht, G., Tinetti, G., et al. 2009, *ApJ*, 690, L114
- Todorov, K., Deming, D., Harrington, J., et al. 2010, *ApJ*, 708, 498
- Walker, G., Matthews, J., Kuschnig, R., et al. 2003, *PASP*, 115, 1023
- Welsh, W. F., Orosz, J. A., Seager, S., et al. 2010, *ApJ*, 713, L145
- Wheatley, P. J., Collier Cameron, A., Harrington, J., et al. 2010, ArXiv:1004.0836 [astro-ph.EP]
- Zahnle, K., Marley, M. S., Freedman, R. S., Lodders, K., & Fortney, J. J. 2009, *ApJ*, 701, L20





# Nederlandse samenvatting

Als je op een heldere nacht op een donkere plek naar de sterrenhemel kijkt, zie je honderden sterren. Als je vaker kijkt, valt het op dat sommige 'sterren' zich verplaatsen langs de hemel. In de oudheid noemde men deze objecten 'dwaalsterren', en nu weten we dat deze objecten - net als de Aarde - planeten zijn die zich in een baan rond de Zon bevinden. De Zon is een ster, en aangezien je met het blote oog al vele honderden sterren kunt zien is het logisch om je af te vragen of onze Zon de enige ster met planeten is. Pas 16 jaar geleden werd de eerste planeet rond een zonachtige ster buiten ons zonnestelsel ontdekt, en sindsdien zijn er in totaal meer dan vijfhonderd exoplaneten gevonden. De meeste planeetsystemen die tot nu toe zijn gevonden lijken echter helemaal niet op ons zonnestelsel - waar de binnenste vier planeten rotsachtig zijn (Mercurius, Venus, Aarde en Mars), met daarbuiten vier gasreuzen (Jupiter, Saturnus, Uranus en Neptunus). Sommige van de exoplaneetsystemen hebben een gasreus, zoals Jupiter, die heel dicht bij zijn ster staat, tot wel 10 keer dichterbij dan Mercurius bij de Zon. Doordat deze planeten zo dicht bij hun ster staan zijn ze ontzettend heet: bij sommige planeten kan de temperatuur aan de dagzijde oplopen tot boven de 2000 graden Celsius, heet genoeg om ijzer te laten smelten!

## Het vinden van exoplaneten

Een planeet rond een andere ster vinden is niet eenvoudig. Het grootste probleem is dat een ster vele malen helderder is dan de planeet, en het licht van de planeet compleet overstraalt. Als de Aarde al het zonlicht dat op het oppervlak valt zou reflecteren, dan nog is de Aarde bijna een miljard keer zwakker dan de Zon. Dit kan worden vergeleken met een vuurvliegje dat rond een groot zoeklicht vliegt. Om toch het licht van de planeet direct waar te kunnen nemen zijn grote telescopen nodig met speciale instrumenten. In de afgelopen paar jaar zijn zo astronomen er in geslaagd om in totaal 24 planeten te 'fotograferen'. HR8799, één van deze 'gefotografeerde' planeetsystemen, heeft zelfs vier planeten!

Behalve direct een plaatje maken van de planeet, kan er ook gezocht worden naar de indirecte effecten die een planeet heeft op zijn ster. Een planeet draait namelijk niet om zijn ster heen, maar de planeet en de ster draaien samen om een gemeenschappelijk zwaartepunt, omdat de planeet ook massa heeft en de ster daarvan de zwaartekracht 'voelt'. Omdat een planeet veel minder zwaar is dan de ster waar hij omheen draait (de massa van Jupiter, de zwaarste planeet in het zonnestelsel, is slechts een duizendste van de massa van de Zon) ligt dit zwaartepunt dicht bij de ster, en is de baan die de ster beschrijft veel kleiner dan de baan van de planeet. Toch zijn er verschillende methodes die kunnen worden gebruikt om deze sterbaan te meten:

### a) De radiële snelheidsmethode:

Terwijl de ster om het gemeenschappelijke zwaartepunt beweegt, verandert de richting waarin deze beweegt. De radiële snelheidstechniek meet de snelheid van de ster langs de gezichtslijn m.b.v. het Dopplereffect, hetzelfde effect dat er voor zorgt dat de toon van de sirene van een

ambulance verandert als deze langs komt rijden. Als de ambulance dichterbij komt, horen we een hogere toon, en als de ambulance gepasseerd is wordt de toon lager. Voor de radiële snelheid zien we dat lijnen in het sterspectrum naar blauwere golflengtes worden geschoven als de ster naar ons toekomt, en naar langere (roodere) golflengtes als de ster van ons af beweegt. De snelheid van de ster is echter heel klein, de verandering van snelheid van de Zon door Jupiter is slechts 12,5 meter per seconde (45 kilometer per uur), terwijl de Zon met een snelheid van slechts 9 centimeter per seconde (300 meter per uur) om het gemeenschappelijke zwaartepunt met de Aarde draait! Doordat slechts de snelheid van de ster langs de gezichtslijn wordt gemeten, kan alleen de minimale massa van de planeet worden bepaald, omdat de hoek waaronder we de planeetbaan zien onbekend is.

De eerste planeet buiten ons zonnestelsel die om een zonachtige ster draait, 51 Pegasi b, werd in 1995 ontdekt met behulp van radiële snelheidsmetingen. In de 16 jaar daarna is deze methode gebruikt om meer dan vierhonderd nieuwe planeten te vinden.

### **b) Astrometrie**

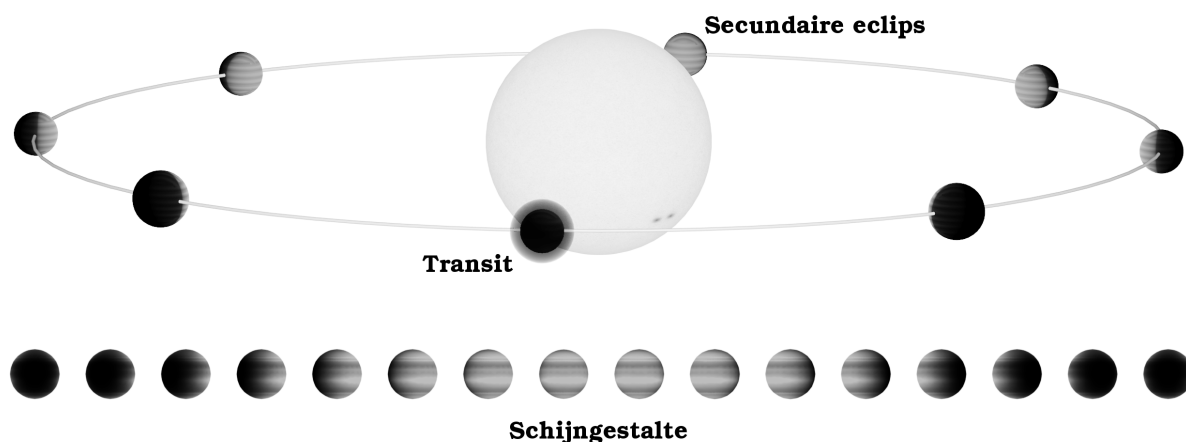
In plaats van de beweging langs de gezichtslijn te meten (zoals gedaan wordt met de radiële snelheidsmethode), kan ook de verplaatsing van de ster in het vlak van de hemel worden bepaald. Om dit te kunnen doen moet de positie van de ster heel nauwkeurig worden gemeten, met een techniek die astrometrie wordt genoemd. Door de metingen te combineren met de radiële snelheid van de ster kan de echte massa van de planeet worden bepaald.

### **c) Timingvariaties**

De derde methode die gebruikt maakt van het feit dat de ster en planeet om een gemeenschappelijk zwaartepunt draaien is de 'timing'-methode. De eerste planeten die via deze methode zijn ontdekt draaiden om een pulsar. Een pulsar is de overgebleven kern van een dode ster die heel snel ronddraait en periodiek sterke radiosignalen uitzendt. De tijd tussen twee pulsen is heel stabiel. Als de pulsar om het gemeenschappelijk zwaartepunt draait, dan staat de pulsar gedurende de ene helft van de baan iets dichterbij de aarde dan gedurende de andere helft. Doordat de lichtsnelheid eindig is komen de pulsen dan eerder of later aan. Door heel precies de aankomsttijden van de pulsen te bepalen, kan daarmee een planeet worden gevonden. Dit kan ook gedaan worden voor dubbelsterren die elkaar gedurende een korte tijd bedekken. Als er een planeet om de twee dubbelsterren draait, dan zullen de tijden waarop de bedekking plaatsvindt iets eerder of later zijn dan verwacht, wat kan worden gebruikt om de baan en massa van de planeet te achterhalen.

## **Planeetovergangen**

De bovenstaande methodes leiden allemaal het bestaan van een planeet af uit de beweging van de ster. Hierdoor is het heel lastig om, behalve de massa, andere eigenschappen van de planeet te bepalen. Als de baan van de planeet echter zo is georiënteerd dat de planeet gedurende een deel van zijn baan tussen de aarde en de ster door beweegt, dan kunnen we meer over de planeet leren. Gedurende zo'n planeetovergang, het moment dat de planeet voor de ster langs beweegt, verduistert de planeet een klein gedeelte van het steroppervlak, wat er voor zorgt dat op Aarde een iets lagere helderheid van de ster wordt gemeten. De afname in de helderheid is direct gerelateerd aan het gedeelte van het steroppervlak dat wordt afgedekt door



**Figuur 7.1** — Illustratie van de verschillende manieren waarmee we de eigenschappen van de atmosferen van exoplaneten kunnen meten. De volledige lichtcurve is te zien in figuur 7.3

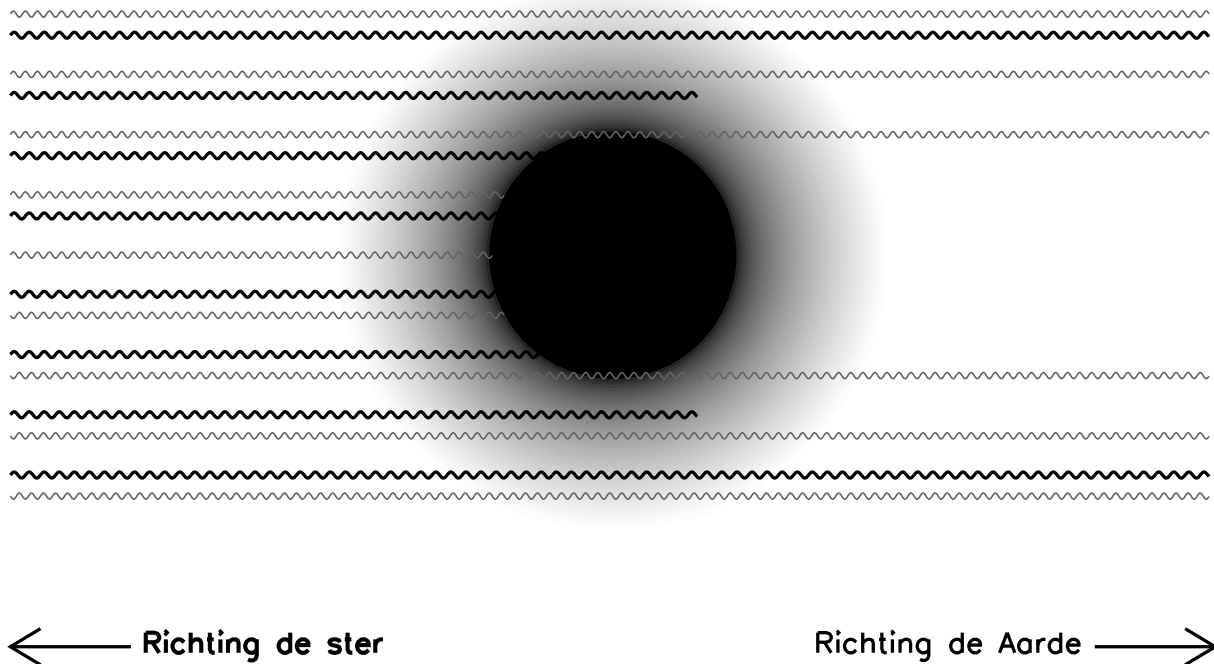
de planeet. Hierdoor kunnen we de grootte van de planeet bepalen. Doordat de planeet voor de ster langs beweegt, weten we de oriëntatie van de baan van de planeet en kunnen we, in tegenstelling tot planeten die alleen via de radiële snelheidsmethode worden ontdekt, de ware massa van de planeet achterhalen. Door de metingen van de straal en de massa van de planeet te combineren kan ook de gemiddelde dichtheid worden bepaald. Deze dichtheid geeft inzicht in de samenstelling van de planeet. Zo zal een planeet die geheel uit gas bestaat, zoals Jupiter, een veel lagere dichtheid hebben dan een rotsachtige planeet zoals de Aarde.

## Het meten van de atmosferen van exoplaneten

Een planeet die een planeetovergang vertoont biedt ook verschillende mogelijkheden om de atmosfeer te bestuderen, zoals geïllustreerd in figuur 7.1:

### a) Transmissiespectroscopie

Als de planeet voor de ster langs beweegt, filtert een deel van het sterlicht door de atmosfeer heen. Atomen en moleculen die in de atmosfeer zitten kunnen dat licht dan absorberen waardoor de planeet een groter deel van het steroppervlak afdekt. Doordat atomen licht slechts op specifieke golflengtes kunnen absorberen, kunnen we ook wat leren over de samenstelling van de planeet. In een absorptielijn, zoals het golflengtegebiedje wordt genoemd waarin een molecuul licht absorbeert, zijn er minder deeltjes nodig om al het licht te absorberen, waardoor het licht hoger in de atmosfeer toch nog volledig geabsorbeerd kan worden, terwijl voor licht buiten een absorptielijn de atmosfeer daar transparant is. Hierdoor lijkt de planeet groter als er gemeten wordt op golflengtes waar absorptielijnen zitten dan op golflengtes buiten de absorptielijnen (zie figuur 7.2). Overigens is absorptie van licht door atomen en moleculen niet de enige manier waarop we de aanwezigheid van atmosfeer kunnen vaststellen. De verstrooiing van het sterlicht in de atmosfeer (wat op de Aarde ervoor zorgt dat de lucht blauw is) kan ervoor zorgen dat de



**Figuur 7.2** — Illustratie van transmissiespectroscopie. De gegolfde lijnen laten lichtstralen zien op twee verschillende golflengtes. De grijze lijn is voor licht dat inefficiënt wordt geabsorbeerd door de planeet atmosfeer, en hierdoor ook op grotere dieptes nog ongehinderd door de planeet atmosfeer komt. De donkere lijn is voor een golflengte waar het licht efficiënt wordt geabsorbeerd, hierdoor wordt de planeet atmosfeer pas transparant op grotere hoogte, en is de gemeten planeetstraal op die golflengte groter.

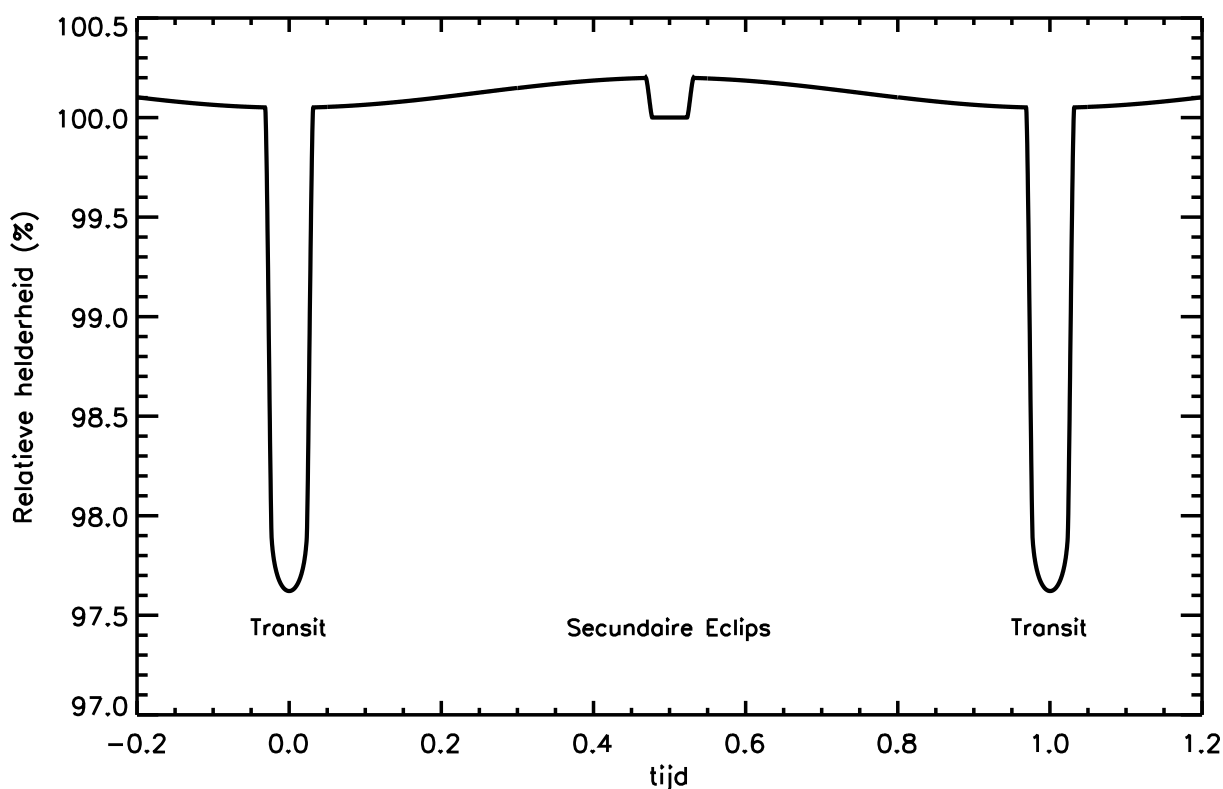
planeet op kortere golflengtes ook groter lijkt dan op langere golflengtes.

### b) Secundaire eclips

Op het moment dat de planeet gezien vanaf de Aarde achter de ster langs beweegt, de secundaire eclips, wordt het licht afkomstig van de planeet geblokkeerd. We zien op dat moment alleen het licht van de ster. Vlak voor en na de secundaire eclips zien we zowel het licht dat afkomstig is van de dagzijde van de planeet, als ook het sterlicht. Hierdoor kunnen we het licht meten dat afkomstig is van de planeet. Het licht dat afkomstig is van de planeet kan zowel gereflecteerd sterlicht zijn, als ook warmtestraling die door de planeet wordt uitgezonden. Voor hete Jupiters is de temperatuur zo hoog, dat ook in het zichtbare licht de warmtestraling domineert over gereflecteerd licht.

### c) Schijngestalten

Behalve door te kijken naar het verdwijnen van het licht van de planeet gedurende de secundaire eclips, kan er ook gezocht worden naar de verandering van het licht van de planeet terwijl deze rond de ster draait. Als de planeet verder in zijn baan beweegt, zien we een steeds groter deel van de dagzijde van de planeet, totdat, vlak voor de secundaire eclips, de gehele dagzijde naar de Aarde is toegericht. Na de secundaire eclips verdwijnt de dagzijde steeds meer uit zicht, en zien we meer en meer van de nachtzijde. Deze schijngestalte van een exoplaneet is vergelijkbaar



**Figuur 7.3** — Illustratie van een volledige fase-curve van een exoplaneet.

met wat we in ons zonnestelsel zien voor Mercurius, Venus of de Maan. In figuur 7.3 staat een illustratie van zo'n fase-curve.

## Dit proefschrift

In dit proefschrift presenter ik de resultaten van onderzoek naar de atmosferen van verscheidene exoplaneten door middel van secundaire eclips metingen en waarnemingen aan planeetovergangen. In het laatste hoofdstuk gebruik ik alle in de literatuur beschikbare metingen om ook de gemiddelde eigenschappen van de atmosferen van deze extreme exoplaneten te bepalen.

In **hoofdstuk 2** wordt de eerste detectie van de secundaire eclips van een exoplaneet gepresenteerd, gemaakt met een telescoop vanaf de grond (i.p.v. in de ruimte). Doordat we vanaf de grond door de aardatmosfeer heen kijken is dit veel moeilijker. De planeet TrES-3b draait in iets meer dan 30 uur om zijn ster heen en de afstand tussen TrES-3b en zijn ster is veertig keer minder dan tussen de aarde en de Zon (wat overeenkomt met slechts zes keer de straal van de ster). Hierdoor ontvangt TrES-3b zoveel energie van zijn ster dat de temperatuur aan de dagzijde blijkt op te lopen tot bijna 1700 graden Celsius.

In **hoofdstuk 3** bestuderen we het licht van de exoplaneet HAT-P-1b, die ongeveer twee maal verder weg staat van zijn ster dan TrES-3b. Daardoor is deze planeet relatief koeler. Hoewel de verwachte temperatuur van de atmosfeer ongeveer 1200 graden Celsius is, meten we een helderheid die overeenkomt met een temperatuur van ongeveer 1850 graden Celsius. Deze temperatuur is ook veel hoger dan de temperatuur die gemeten wordt op langere golflengte,

en is lastig te verklaren met realistische modellen voor de planeet atmosfeer, maar dat komt waarschijnlijk doordat we dieper in de atmosfeer kijken.

In **hoofdstuk 4** laten we resultaten zien van secundaire-eclipswaarnemingen van de exo-planeet WASP-33b, een hete Jupiter die in minder dan 30 uur om zijn ster heen draait. De ster waar WASP-33b omheen draait zendt meer licht uit dan de Zon, waardoor WASP-33b ongeveer tien-duizend keer meer energie van zijn ster ontvangt dan de Aarde. De temperatuur in de atmosfeer van de planeet kan daarom oplopen tot boven de 3000 graden Celsius, net zo heet als rode dwergensterren. Onze metingen wijzen uit dat de atmosfeer van de planeet inderdaad extreem heet is, wat betekent dat al het invallende sterlicht moet worden geabsorbeerd in de atmosfeer, en dat deze energie bijna direct weer wordt uitgezonden. Dit moet tot een groot verschil in de temperatuur leiden tussen de dag- en de nachtzijde van de planeet.

De super-Aarde GJ1214b, het onderwerp van **hoofdstuk 5**, draait in anderhalve dag rond zijn ster. Echter, in tegenstelling tot die van de eerder genoemde planeten, is de moederster van GJ1214b veel koeler dan de Zon, waardoor de temperatuur in de atmosfeer waarschijnlijk ‘slechts’ 200 graden Celsius is. Hoewel dit veel heter is dan de temperatuur op Aarde, is dit een van de koelste exoplaneten die een planeetovergang laat zien. GJ1214b wordt een super-Aarde genoemd, omdat hij zes en een half keer zwaarder dan de Aarde is. De vergelijking met de Aarde gaat echter niet helemaal op, want ondanks het feit dat GJ1214b veel zwaarder is, is zijn dichtheid ongeveer drie maal lager dan de Aarde. Er zijn drie modellen voor de samenstelling van de planeet die de lage dichtheid kunnen verklaren. In de eerste plaats kan GJ1214b grotendeels uit water bestaan met een atmosfeer bestaande uit stoom. Deze atmosfeer is heel compact en zal geen sterke signalen voor transmissiespectroscopie op leveren. In het tweede model wordt de dichtheid van GJ1214b verklaard doordat deze een rotsachtige kern heeft, zoals de Aarde, met daarom heen een dikke atmosfeer van gas. Ten slotte is het ook mogelijk dat GJ1214b een mini-Neptunus is. In de laatste twee gevallen is de atmosfeer van GJ1214b uitgestrekt genoeg om deze te kunnen meten met transmissiespectroscopie.

Om de samenstelling van GJ1214b te onderzoeken, hebben we een groot aantal transmissiespectroscopische waarnemingen verkregen op verschillende golflengtes. De waarnemingen op blauwe golflengtes zijn gekozen om te zoeken naar de verstrooiing van sterlicht in de planeet-atmosfeer, terwijl waarnemingen in het nabije infrarood gevoelig zijn voor de absorptie door moleculen. Uit onze waarnemingen blijkt dat we een iets grotere straal zien in blauw licht, wat een aanwijzing is dat er inderdaad sterlicht in de atmosfeer wordt verstrooid. In het infrarood zien we ook een iets grotere planeet, wat zou kunnen worden veroorzaakt door absorptie van sterlicht door moleculen. Opmerkelijk genoeg wijzen de gemeten stralen in het infrarood uit dat er wel slechts een kleine hoeveelheid methaan in de atmosfeer kan zitten. Er zullen nog meer metingen gedaan moeten worden om dit verder te onderzoeken.

In **hoofdstuk 6** worden de resultaten van mijn onderzoek naar de gemiddelde eigenschappen van de atmosferen van hete Jupiters gepresenteerd. In de afgelopen 6 jaar zijn er vele waarnemingen gedaan van de thermische straling van de hete Jupiters. In veel studies werden de eigenschappen van de atmosfeer van de individuele planeten bestudeerd. In dit hoofdstuk bestudeer ik hoe de eigenschappen van deze planeten mogelijk worden beïnvloed door hun omgeving, bijvoorbeeld de hoeveelheid sterlicht die ze ontvangen. Hiervoor heb ik alle waarnemingen uit de literatuur (waaronder ook hoofdstukken 2 tot en met 4) verzameld.

We zien dat gemiddeld de planeten warmer lijken in het optisch en nabij infrarood dan in het mid-infrarood. Dit geeft aan dat de atmosferen van hete Jupiters moleculen, zoals koolstofmonoxide, methaan en water, moeten bevatten, omdat anders de gemeten temperatuur op alle golflengtes hetzelfde zou moeten zijn.

Als we de planeten opdelen in planeten rond actieve sterren – sterren die veel variatie in hun helderheid laten zien – en planeten rond rustige sterren – zoals de Zon – en vervolgens op elke golflengte de metingen combineren, zien we dat voor deze twee groepen planeten de gemiddelde spectra erg verschillen. Waar bij de planeten rond de rustige sterren het spectrum een koelere temperatuur laat zien op golflengtes tussen de 3 en de 5 micrometer, laat het spectrum van planeten rond actieve sterren juist een ongeveer constante temperatuur zien. Dit verschil in het spectrum kan worden verklaard door een verschil in de manier waarop de temperatuur in de atmosfeer varieert met de hoogte. In de atmosfeer voor de planeten rond de actieve sterren neemt de temperatuur af naarmate je hoger in de atmosfeer komt. Bij de planeten rond rustige sterren gebeurt er iets anders: eerst neemt de temperatuur in de atmosfeer af als je hoger in de atmosfeer komt, maar als je nog verder omhoog gaat wordt de atmosfeer plotseling weer heter. Het gebied met deze stijging van temperatuur heet een inversielaag. Ook de atmosfeer van de Aarde heeft een inversielaag, de stratosfeer. Tot ongeveer 10 tot 12 kilometer hoogte neemt de temperatuur af, maar daarboven wordt het opeens weer snel warmer. Om een inversielaag te krijgen moet er veel energie in deze laag worden geabsorbeerd. In de Aardatmosfeer komt dit door absorptie van zonlicht door ozon, maar voor een hete Jupiter is het molecuul dat verantwoordelijk is voor deze absorptie nog niet geïdentificeerd.

Het feit dat de planeten rond de actieve sterren geen inversielaag hebben, terwijl de planeten rond de rustige sterren dat wel hebben, lijkt wel aan te geven dat de variabiliteit van de ster een rol kan spelen, mogelijk doordat een verhoogde variabiliteit gepaard gaat met een grotere hoeveelheid straling in het ultraviolet, wat mogelijk het absorberende molecuul vernietigt.





# Curriculum vitae

Op 30 oktober 1983 ben ik geboren in 's-Gravenhage, waarna ik ben opgegroeid in Wassenaar. Al van jongs af aan heb ik een interesse in sterrenkunde gehad. Na de basisschool ging ik naar het Vrijzinnig Christelijk Lyceum in Den Haag en tijdens mijn middelbareschooltijd heb ik daar samen met een paar andere scholieren een computerclub opgericht. In 2001 heb ik deelgenomen aan een zomerschool voor middelbare scholieren over exoplaneten, georganiseerd door de Universiteit van Leiden. Mijn gymnasiumdiploma behaalde ik in 2002.

Gezien mijn interesse was het geen verrassing dat ik in 2002 sterrenkunde in Leiden ging studeren, waar ik in 2005 mijn Bachelor of Science heb behaald. Daarna ben ik direct doorgegaan met mijn masteropleiding. In het laatste jaar van mijn master heb ik de kans gekregen om als assistent mee te gaan met het sterrenkundig practicum 2 naar La Palma, voor een week waarnemen met de 2.5 meter Isaac Newton Telescoop. Mijn masteropleiding rondde ik in november 2007 met lof af met het onderzoek *Colour-radius relation for low-redshift galaxies in the SDSS*, dat ik heb gedaan onder begeleiding van prof. dr. Marijn Franx. In het laatste jaar van mijn masteropleiding ben ik begonnen met foto's te maken tijdens evenementen die door de Sterrewacht waren georganiseerd, waaronder de Nederlandse Astronomen Conferentie in Veldhoven, en een symposium voor Rudolf Le Poole. Ook tijdens mijn promotieonderzoek heb ik bij verscheidene gebeurtenissen op de Sterrewacht foto's gemaakt, waaronder het jaarlijkse bezoek van Sinterklaas en de kerstlunch.

Na het afstuderen ben ik in Leiden begonnen met mijn promotieonderzoek naar exoplaneten. Oorspronkelijk was het de bedoeling dat ik in data van de OmegaTrans Survey naar exoplaneten zou gaan zoeken, maar door problemen met de constructie van de VLT Survey Telescope is het daar niet van gekomen. Hierdoor ben ik me gaan verdiepen in het onderzoek naar de atmosferen van exoplaneten, waarvan de resultaten hier in dit proefschrift zijn gebundeld.

Tijdens mijn promotie heb ik ongeveer vijftig nachten doorgebracht in de controlekamers van verscheidene telescopen om exoplaneten, of in het geval van slecht weer de binnenkant van de koepel, te bestuderen. Voor deze waarnemingen ben ik vele malen op La Palma geweest, maar deze reizen brachten me ook naar Tenerife, Chili en Hawai'i. Tien van de waarneemachten op La Palma waren in het kader van het Sterrenkundig practicum 2, waar ik gedurende twee jaar assistent was. In het laatste jaar heb ik geassisteerd bij zowel het tweedejaars vak Modern Sterrenkundig Onderzoek, als ook het Bachelor Onderzoek.

In de afgelopen vier jaar heb ik deelgenomen aan symposia en workshops in Boston, Parijs, Cuijk, Exeter en Turijn en aan een zomerschool in Pasadena. De resultaten van mijn onderzoek heb ik op verscheidene van deze symposia gepresenteerd. Ook heb ik een colloquium gegeven aan het Instituto de Astrofísica de Canarias op Tenerife.

Na mijn promotie zet ik mijn onderzoek naar de atmosferen van exoplaneten voort aan de universiteit van Toronto.



# Nawoord

Op deze laatste pagina van mijn proefschrift is het tijd om de mensen te bedanken die hebben bijgedragen aan de resultaten die in dit proefschrift te vinden zijn, want onderzoek doe je niet alleen.

In de eerste plaats wil ik de Leidse exoplaneetgroep bedanken. Simon, it was always good to discuss observations of exoplanet atmospheres and the misbehaving binary stars with you. Bas, bedankt voor het doen van enkele van de waarnemingen en veel succes met het vinden van de eerste planeet in de WFCAM Transit Survey. Matteo, it was always interesting to see the newest results from the CRIRES project, and I hope that after your many trips to Chile and La Palma you now have enough time to work on these exciting new data. Jayne, the discussions about the search for exoplanets and the investigation of their atmospheres were always very stimulating. Gilles, bedankt dat je de waarnemingen met de WHT in Juli 2011 wilde doen. Zonder dat had dit proefschrift veel vertraging opgelopen!

Zonder de goede ondersteuning van het systeembeheer was dit proefschrift nooit op tijd klaar geweest. David, Erik, Tycho en Aart, bedankt dat jullie mijn computer ondanks enkele harddisk crashes, altijd aan de praat hebben weten te houden. Liesbeth, Jeanne en Anita van het secretariaat verdienen zeker een vermelding, want zonder hun ondersteuning, of het om een setje nietjes ging of hulp bij het regelen van zalen, was het leven op de Sterrewacht veel moeizamer geweest. En natuurlijk kunnen Jan en Evelijn niet in dit rijtje ontbreken, want zonder hun inspanning was het regelen van reizen e.d. veel lastiger geweest.

Voor mijn conferentiebezoeken heb ik financiering gekregen van het Leids Kerkhoven-Bosscha Fonds, en mijn waarneemreizen werden (deels) gefinancierd door het Leids Sterrewacht Fonds.

During my PhD, I have spent many nights observing at different telescopes, and the success of these observations would not have been possible without the support of the staff at the observatories. I would therefore like to thank the staff of the Isaac Newton Group, in particular Raine Karjalaine, Miguel Santander, Samantha Rix, Fiona Riddick, Andrew Cardwell and Ber-to González for the support during my WHT observations. Furthermore I would like to thank the staff at the United Kingdom Infrared Telescope and at ESO's Paranal observatory for their assistance with the observations.

Franco, Maarten, Renske, Wendy and Wouter, it was a pleasure to share an office with you. Reinout en Raymond, het was altijd gezellig om tijdens de koffie en lunch te praten over het onderzoek, datareductie pipelines en de wereld in het algemeen.

En tot slot wil ik natuurlijk mijn ouders bedanken, voor het stimuleren van mijn interesse in sterrenkunde en hun steun tijdens mijn promotieonderzoek.

